Improving the determination of moment tensors, moment magnitudes and focal depths of earthquakes below Mw 4.0 using regional broadband seismic data:

Author: Nawa Dahal

Boston College Electronic Thesis or Dissertation, 2019

IMPROVING THE DETERMINATION OF MOMENT TENSORS, MOMENT MAGNITUDES AND FOCAL DEPTHS OF EARTHQUAKES BELOW M_W 4.0 USING REGIONAL BROADBAND SEISMIC DATA

NAWA R. DAHAL

A dissertation
submitted to the Faculty of
the Department of Physics
in partial fulfillment
of the requirements for the degree of
Doctor of Philosophy

Boston College
Morrissey College of Arts and Sciences
Graduate School

September 2019

IMPROVING THE DETERMINATION OF MOMENT TENSORS, MOMENT MAGNITUDES AND FOCAL DEPTHS OF EARTHQUAKES BELOW M4.0 USING REGIONAL BROADBAND SEISMIC DATA

Author: Nawa R. Dahal

Advisors: Prof. Michael J. Naughton and Prof. John E. Ebel

Committee Members: Prof. David Broido

Prof. Michael Graf

ABSTRACT

Determining accurate source parameters of small magnitude earthquakes is important to understand the source physics and tectonic processes that activate a seismic source as well as to make more accurate estimates of the probabilities of the recurrences of large earthquakes based on the statistics of smaller earthquakes. The accurate determination of the focal depths and focal mechanisms of small earthquakes is required to constrain the potential seismic source zones of future large earthquakes, whereas the accurate determination of seismic moment is required to calculate the sizes (best represented by moment magnitudes) of earthquakes. The precise determination of focal depths, moment magnitudes and focal mechanisms of small earthquakes can help greatly advance our knowledge of the potentially active faults in an area and thus help to produce accurate seismic hazard and risk maps for that area.

Focal depths, moment magnitudes and focal mechanisms of earthquakes with magnitudes M_w 4.0 and less recorded by a sparse seismic network are usually poorly constrained due to the lack of an

appropriate method applicable to find these parameters with a sparse set of observations. This dissertation presents a new method that can accurately determine focal depths, moment magnitudes and focal mechanisms of earthquakes with magnitudes between M_w 4.0 and M_w 2.5 using the broadband seismic waveforms recorded by the local and regional seismic stations. For the determination of the focal depths and the moment magnitudes, the observed seismograms as well as synthetic seismograms are filtered through a bandpass filter of 1-3 Hz, whereas for the determination of the focal mechanisms, they are filtered through a bandpass filter of 1.5-2.5 Hz. Both of these frequency passbands have a good signal-to-noise ratio (SNR) for the small earthquakes of the magnitudes that are analyzed in this dissertation. The waveforms are processed to their envelopes in order to make the waveforms relatively simple for the modeling. A grid search is performed over all possible dip, rake and strike angles and as well as over possible depths and scalar moments to find the optimal value of the focal depth and the optimal value of the scalar moment. To find the optimal focal mechanism, a non-linear moment-tensor inversion is performed in addition to the coarse grid search over the possible dip, rake and strike angles at a fixed value of focal depth and a fixed value of scalar moment.

The method of this dissertation is tested on 18 aftershocks of M_w between 3.70 and 2.60 of the 2011 Mineral, Virginia M_w 5.7 earthquake. The method is also tested on 5 aftershocks of M_w between 3.62 and 2.63 of the 2013 Ladysmith, Quebec M_w 4.5 earthquake. Reliable focal depths and moment magnitudes are obtained for all of these events using waveforms from as few as 1 seismic station within the epicentral distance of 68-424 km with SNR greater or equal to 5. Similarly, reliable focal mechanisms are obtained for all of the events with M_w 3.70-3.04 using waveforms from at least 3 seismic stations within the epicentral distance of 60-350 km each with

SNR greater or equal to 10. Tests show that the moment magnitudes and focal depths are not very sensitive to the crustal model used, although systematic variations in the focal depths are observed with the total crustal thickness. Tests also show that the focal mechanisms obtained with the different crustal structures vary with the Kagan angle of 30° on average for the events and the crustal structures tested. This means that the event moment magnitudes and event focal mechanism determinations are only somewhat sensitive to the uncertainties in the crustal models tested. The method is applied to some aftershocks of the M_w 7.8, 2015 Gorkha, Nepal earthquake which shows that the method developed in this dissertation, by analyzing data from eastern North America, appears to give good results when applied in a very different tectonic environment in a different part of the world.

This study confirms that the method of modeling envelopes of seismic waveforms developed in this dissertation can be used to extract accurate focal depths and moment magnitudes of earthquakes with M_w 3.70-2.60 using broadband seismic data recorded by local and regional seismic stations at epicentral distances of 68-424 km and accurate focal mechanisms of earthquakes with M_w 3.70-3.04 using broadband seismic data recorded by local and regional seismic stations at epicentral distances of 60-350 km.

TABLE OF CONTENTS

LIST OF TABLES

Table **Page**

Chapter 3

Chapter 4

Chapter 5

Chapter 6

LIST OF FIGURES

Figure **Page**

Chapter 2

Chapter 3

Chapter 4

Chapter 5

Chapter 6

ACKNOWLEDGEMENTS

Firstly, I would like to express my profound gratitude to my dissertation advisor, Prof. John E. Ebel for his excellent guidance, support and encouragement throughout my years of research. It has been an honor to be his first Ph.D. student. I believe that I have developed a comprehensive understanding of the subject matter under his excellent guidance. I would also like to thank my advisor in the Physics Department, Prof. Michael J. Naughton, for the guidance and support that he provided as well as for allowing me to pursue this interdisciplinary research between the Department of Physics and the Department of Earth and Environmental Sciences. I am very thankful to my committee members Prof. David Broido and Prof. Michael Graph for taking the time and interest to be on my committee and for providing me with worthy comments to improve this dissertation. I am also thankful to my academic advisor Prof. Ying Ran for his guidance. I greatly appreciate Prof. Michael Graf, current Chair of the Department of Physics, Prof. Michael Naughton, past Chair of the Department of Physics and Jane Carter, Physics Department Administrator, for providing me with financial support to carry out this research.

I also would like to acknowledge Prof. Ethan Baxter, Chair of the Department of Earth and Environmental Sciences and Prof. Gail C. Kineke, Graduate Program Chair in the Department of Earth and Environmental Sciences, for providing me with financial support which made this research possible. I am also indebted to Prof. Alan L. Kafka, Director of the Weston Observatory of Boston College, and to Marilyn Bibeau of Weston Observatory for providing me with use of the facilities at the Observatory. I greatly appreciate Prof. Douglas Dreger at the Department of Earth and Planetary Sciences, UC Berkeley for the comments and suggestions that he provided to

me at scientific meetings to improve this work. I would also like to thank all the professors, staff and my colleagues in the Department of Physics and the Department of Earth and Environmental Sciences at Boston College.

Finally, I would like to thank my parents, my entire family and my friends who supported me in all pursuits of my life without whom I would not have done this degree. I am indebted to my wife Chetana for her love and support during the final years of my Ph.D.

Thank you.

Nawa R. Dahal

Department of Physics/

Department of Earth and Environmental Sciences

Boston College

September 2019

DEDICATION

This dissertation is dedicated to my parents and my entire family for their continuous support and encouragement throughout my academic career. In writing this thesis, I want to remember my sister who lost her life in the 25 April 2015 Gorkha, Nepal, earthquake.

QUOTATION

"Imagination is more important than knowledge. Knowledge is limited. Imagination encircles the world."

-Albert Einstein

Chapter 1

INTRODUCTION

1.1 MOTIVATION

The number of earthquakes occurring per year around the globe increases almost ten times with a one unit decrease in earthquake magnitude. The major portion of the earthquake catalog for the earth is occupied by the earthquakes with magnitudes less than M_w4.0 (referred to as small magnitude earthquakes throughout this dissertation). Constraining the source parameters of small magnitude earthquakes is crucial for those areas where large earthquakes are not frequent, and thus one must rely on small earthquakes to help quantify the seismic hazard of an area due to the infrequent large earthquakes. Determining accurate source parameters of the small magnitude earthquakes is important to understand the seismic source physics and tectonic processes that activate a seismic source. The accurate determinations of the focal mechanisms and focal depths of small earthquakes are required to constrain the potential seismic source zones of future large earthquakes, whereas the accurate determination of moment magnitude is required to make more accurate estimates of the probabilities of recurrence of large earthquakes based on the recurrence rates of small earthquakes. The mean recurrence rate of large earthquakes is obtained by determining a Gutenberg-Richter line at small magnitudes and extrapolating it to higher magnitudes. A common problem is that the magnitudes for these small earthquakes are typically not moment magnitudes but rather some other kind of magnitudes. Thus, the first step to solve this problem would be to obtain moment magnitudes for the small earthquakes, which

usually is done by estimating a conversion factor from other magnitudes to moment magnitudes. This additional step of magnitude conversion involves inherent uncertainty which adds a level of uncertainty to the estimates of the mean repeat times of large earthquakes as a function of moment magnitude. A direct measurement of moment magnitude (based on the scalar moment) for small events eliminates the uncertainties involved in the conversion from one magnitude scale to another and makes the estimation of mean repeat times of the larger events as a function of moment magnitude more accurate.

The precise determination of seismic moments, focal mechanisms and focal depths for small earthquakes can help greatly to advance our knowledge of the potentially active faults in an area and thus helps to produce accurate seismic hazard and risk maps for that area. Improved information on seismic hazard will encourage government agencies as well as the general public to take the necessary actions to mitigate the losses from future strong earthquakes. These considerations have played a major role in motivating the research presented in this dissertation.

1.2 OVERVIEW OF THE PRESENT STUDY

The accurate determination of the focal depths, moment magnitudes and focal mechanisms of earthquakes is required to understand the faulting process during earthquakes as well as for constraining the potential seismic source zones for future earthquakes. If the seismic network is spatially dense near an earthquake epicenter, P-wave first-motion data and S/P

amplitude ratios can be used to calculate the focal depth, moment magnitude and focal mechanism for that earthquake. If the seismic network coverage is sparse around an earthquake epicenter, then the most accurate focal depths, moment magnitudes and focal mechanisms are obtained through the moment-tensor inversion of local and regional waveform data. One of the moment-tensor inversion methods that is commonly used with regional seismic network data from a sparse network of stations is Dreger's moment-tensor inversion method, which uses waveforms filtered through a relatively low frequency passband that is typically of 0.05-0.1 Hz (*Dreger and Helmberger, 1990; Ford et al., 2009*). There are other versions of moment-tensor inversion methods that are routinely used for sparse regional data, such as those employed by the Saint Louis University Earthquake Center (SLUC) which filters the waveforms through a band pass filter of 0.03-0.08 Hz and the National Earthquake Information Center (NEIC) of the United States Geological Survey (USGS) (I was not able to find the filter parameters for this one). Both of these regional waveform inversion methods process the seismic waveforms with a low-pass filter which only passes the fundamental-mode surface waves, excluding the body waves from being included in the inversion. The surface waves utilized in all of these inversion methods have good signal-to-noise ratio (SNR) usually only for events with magnitudes about M_w 4.0 and higher, and it is for this reason that these moment-tensor inversion methods are able to obtain accurate focal mechanisms for earthquakes of magnitude above about M_w 4.0 (*Guilhem et al., 2014*). The source parameters obtained from these methods become progressively more inaccurate as the sizes of the events analyzed decrease below M_w 4.0, although in some cases these inversion methods can extract accurate source parameters of earthquakes smaller than M_w 4.0. For example, the catalog of regional moment-tensor

inversion results for North America put together by the SLUC has 103 events with $M_w \geq 4.0$, 86 events with $4.0 > M_w \geq 3.5$ and only 9 events with $M_w < 3.5$ of the total number of 198 events that were analyzed for the year 2018 (http://www.eas.slu.edu/eqc/eqc_mt/MECH.NA/2014.html, last visited May 2019). This shows how the number of events that can be analyzed using moment-tensor inversion method decreases for $M_w < 4.0$ using the method employed by the SLUC.

In addition to the limitations provided by SNR, imprecise velocity models available for the determinations of the source parameters of local and regional earthquakes, the trade-off between the source depth and the earthquake origin time inherent in earthquake locations computed using P and S arrival times, and the sparse distribution of the regional and local seismic stations of many regional seismic networks present additional problems towards computing accurate focal depths, moment magnitudes and focal mechanisms of earthquakes below M_w 4.0 (*Tan and Helmberger, 2007; Wéber, 2006*). An imprecise velocity model and uncertainties in earthquake focal depth due to the trade-off between the origin time and focal depth of an earthquake when the hypocenter is computed from a sparse regional seismic network introduce uncertainties in the calculation of the Green's functions for the determination of seismic source parameters. Sparse seismic network data almost always lack the dense distance and azimuthal coverage required to compute well-constrained focal mechanisms of the events using the P-wave first motion data recorded by the network stations.

Various techniques have been developed in an effort to find accurate and precise focal mechanisms and hypocentral depths of earthquakes of M_w<4.0 using local and regional data. A summary of past published works to calculate the focal depths and focal mechanisms of earthquakes below M_w 4.0 using local and regional seismic waveforms with their associated limitations is discussed in the following paragraphs.

One method to find focal depth involves using the depth phase sPg and the ratio Rg/Sg, as was done by *Langston (1987)* to constrain the depths of 59 earthquakes recorded at epicentral distances of 60-95 km and having local magnitudes 2.5-4.2 containing the foreshocks and aftershocks of the M_s6.8 1986 Meckering, Australia earthquake. Another method utilizes local and regional depth phases to calculate the differential time between a depth phase and a reference P phase, such as the pP-P or sP-P time difference, to estimate earthquake depth (*Ma, 2010; Bock, 2010*). *Ma (2010)* obtained the focal depths of 29 earthquakes of magnitude M_N2.8-5.5 using data from stations with epicentral distances within 30-253 km (but also with one station at 628 km). *Ma and Eaton (2011)* combined the double-difference relocation method with modeling of regional depth phases (MRDP) to improve hypocenter depth accuracy and constrained the focal depths of 10 earthquakes of magnitudes M_N 2.0-4.3 and 7 earthquakes of magnitudes M_L 0.34-2.34, using data from stations within about 300 km epicentral distance. Stacking multiple-station autocorrelograms (SMAC) is another approach that has been taken to enhance the SNR of the depth phases so that the depth phases can be identified accurately and the focal depths can be well constrained (*Zang et al., 2014*). *Zang et al. (2014)* describe the method for

SMAC and apply it to 1 earthquake of M_w 3.8 using SH-wave data from 37 stations with SNR>3.6, within the epicentral distance of 5°. The data were filtered through a frequency band of 0.8-8 Hz before being analyzed using the method by *Zang et al. (2014)*.

The methods for the determination of the focal depth described in the previous paragraph have their own limitations. The ratio Rg/Sg method like that employed by *Langston (1987)* can only be used to constrain the focal depths of very shallow events because Rg waves have observable amplitudes only for events with focal depths less than about 4 km (*Kafka, 1990*). One issue with using regional depth phases to calculate focal depths such as in the MRDP method is that these phases often are not easily discernible or identifiable for the epicentral distance range of 100-500 km, which is typically the epicentral distance range for the local and regional seismic stations in a sparse seismic network that detects small local earthquakes (*Ma, 2010 and Bock, 2010*). The application of the SMAC method becomes limited for earthquakes recorded by a sparse network as the data from a large number of seismic stations (37 stations) were used for the event analyzed by *Zang et al., (2014)* are required in order to enhance SNR through stacking.

Some other approaches using waveform modeling to constrain the focal mechanisms of earthquakes with magnitudes M_w<4.0 have also been published. *Guilhem et al. (2014)* computed the full moment-tensor solutions for 13 earthquakes of M_w 4.03-3.15 and 1 earthquake of magnitude M_w 2.6 at the Geysers geothermal field in California using waveform modeling. They were able to calculate accurate focal mechanisms for these

earthquakes by fitting synthetic waveforms to the observed waveforms taken from at least 4 stations with epicentral distances of 1 to 6 km. In their analysis, the observed and synthetic waveforms were filtered with a frequency band of either 0.5-2.5 Hz or 0.7-1.7 Hz. Using a different waveform modeling method, relative moment-tensor solutions were obtained for the 2003 Big Bear sequence by *Tan and Helmberger (2007*) for earthquakes with magnitudes M_w<3.5, which they calibrated using the known focal mechanisms of events of M_w 4.0 and greater that were computed using the regional moment-tensor inversion method. They filtered the short-period P-waveform data recorded at least at 10 seismic stations with epicentral distances up to 200 km through a frequency band of 0.5-2.0 Hz to invert for the moment-tensors of events with M_w 3.5-2.0. With yet another method (*D'Amico et al., 2011; D'Amico, 2014*), P and S waves from waveforms recorded at least at 4 stations within 200 km of epicenters were filtered separately before inverting them for the moment-tensor. The P waves were filtered through a passband of 0.05-0.3 Hz and the S and surface waves were filtered through a 0.02-0.1 Hz frequency passband. Moment-tensor solutions of earthquakes in the Calaboro-Peloritan Arc region in southern Italy (*D'Amico et al., 2011*) and of an earthquake swarm off-shore of Malta in the central Mediterranean (*D'Amico, 2014*) were obtained using this method. This method is called the Cut-And-Paste (CAP) inversion and is described in *Zhu and Helmberger (1996)* and *Tan et al. (2006)*. Focal mechanisms of earthquakes of magnitude M_w 4.6 to M_w 3.6, except for one event with magnitude M_w 2.8 were obtained using this method by *D'Amico et al. (2011)*.

All of the methods developed described above to constrain the focal mechanisms of M_w 4.0-2.5 events using waveform modeling have limited applications. The method used for the Geysers events (*Guilhem et al., 2014*) is applicable only to smaller events recorded by stations very close to the epicenters (the epicentral distances used were 1-6 km). The method of *Tan and Helmberger (2007)* is only applicable to small magnitude earthquakes that have at least one nearby earthquake of $M_w \geq 4.0$ whose source parameters could be obtained through a currently available moment-tensor inversion method. In many regions, there is at most only a very small number of $M_w < 4.0$ earthquakes with nearby $M \geq 4.0$ earthquakes such that the Tan and Helmberger method can be used. The CAP method is applicable for the events which are recorded by least 4 seismic stations within 200 km of the epicenter (*D'Amico et al., 2011; D'Amico, 2014*). This requirement is fulfilled only by earthquakes with magnitude M_w 3.6 and above except for one event of magnitude M_w 2.8 among all the earthquakes on which this method was tested (*D'Amico et al., 2011; D'Amico, 2014*). All of the methods described above use different passband filters to filter the data and are applied to data with different magnitude ranges, epicentral distance ranges and azimuthal coverage. None of these methods can be used to estimate the focal depths, seismic moments or focal mechanisms of all earthquakes of M_w 2.5-4.0 for a region with predominantly sparse regional seismic network coverage like that in the Central and Eastern United States (CEUS). Thus, a more general method that can be applicable for all such earthquakes is still needed.

1.3 RESEARCH OBJECTIVES

For the reasons described in the previous section, the methods that have been developed so far to obtain the source parameters of earthquakes below M_w 4.0 are limited in terms of their application. All of the methods described in the previous section of this dissertation can be used with data sets with limited frequency bands, limited magnitude ranges and/or limited epicentral distance ranges. The research objective of this dissertation is to develop a method that works for all M_w 4.0-2.5 earthquakes recorded by only a few regional seismic stations in the epicentral distance range of 50-500 km in which the data for all of these earthquakes could be filtered through a single bandpass filter. Specifically, this dissertation aims to demonstrate the use of synthetic waveforms computed using a 1-D crustal structure and the modeling of waveform envelopes for constraining the source focal depths, moment magnitudes and focal mechanisms of all earthquakes between M_w 40 and M_w 2.5 for regions of sparse regional seismic network coverage.

1.4 ORGANIZATION OF THE DISSERTATION

By introducing regional waveform analysis in general and then proposing a new analysis method to extend it to use it to smaller magnitude earthquakes, this dissertation comprehensively deals with the determination of source properties of earthquakes with magnitudes M_w 4.0-2.5. The chapters following this introductory section describe how the research objective described in Section 1.2 is met.

Chapter 2 discusses the background theory required for this dissertation. This chapter defines the basics of earthquake source physics and of seismic wave propagation through the crust that are pertinent to the method developed in this dissertation. The source parameters that are to be constrained, namely the dip, rake and strike angles, the focal depth and the seismic moment expressed as the moment magnitude, are defined in this chapter. The calculation of the Green's functions and the synthetic seismograms that are computed using those Green's functions are also discussed.

Chapter 3 gives an overview of the data processing and modeling methodology developed in this study to constrain the source properties of earthquakes with magnitudes M_w 2.6-3.7. The concept of the envelope of a seismic waveform and how it can be applied to constrain the source properties of small earthquakes is introduced in this chapter. The variation of SNR with different frequency passbands is explored. The aftershock sequences to which the methodology is applied are introduced in this chapter. One aftershock sequence is that of the M_w5.7 Mineral, Virginia earthquake that occurred on 23 August 2011 with origin time 17:51:3.9 UTC. A second aftershock sequence is that of the M_w 4.3 Ladysmith, Quebec earthquake that occurred on 17 May 2013 with origin time 13:43:23 UTC. The third aftershock sequence is that of the M_w 7.8 Gorkha, Nepal earthquake that occurred on 25 April 2015 with origin time 06:11:25 UTC.

Chapter 4 illustrates the application of the method as applied to the determination of the focal depths and moment magnitudes of the aftershocks of the Mineral and Ladysmith earthquakes. The details involved in applying the methodology described in Chapter 3 to these aftershocks are described in this chapter. The threshold SNR and the minimum number of the stations required to accurately determine the focal depths and the scalar seismic moments using the method are estimated. The sensitivity of the focal depths and the moment magnitudes with changes in crustal structure is tested. A comparison of the results obtained using the new method of this dissertation to the results obtained by previous studies of the events of the two aftershock sequences is provided.

Chapter 5 describes the determination of focal mechanisms of small magnitude earthquakes by applying the methodology presented in Chapter 3 to some aftershocks of the Mineral earthquake and the Ladysmith earthquake. The details involved in the application of the method as well as the test results on the threshold SNR and the minimum number of the stations required to determine accurate focal mechanisms are presented. The effect of azimuthal coverage on the final focal mechanism is explored. A comparison is made between the focal mechanisms determined in this study and those obtained from the previously published studies on these earthquakes.

Chapter 6 explains the results of applying the method described in Chapter 3 to the aftershocks of M_w 7.8 2015 Gorkha earthquake to obtain the focal depths, focal mechanisms and the moment magnitudes of those aftershocks. The results are interpreted

relative to the geological setting, and the results are compared to the previously published results on these earthquakes.

Finally, Chapter 7 summarizes the results obtained in this dissertation and concludes with suggestions for the further research.

Chapter 2

Background Theory

A summary of the theory of the seismic source and the propagation of the seismic waves through the crust with application to the waveform modeling discussed in this dissertation is presented in this chapter. The summary is provided to give the readers sufficient background to understand what is presented in the following chapters.

2.1 FAULTS

A fault is a surface along which the slip of rock has occurred. Although a fault can have any orientation and the slip on a fault surface can be in any direction, there are three basic types of faulting from which all possible earthquake fault motions can be derived. These basic faults are shown in Figure 2.1. Thrust faulting, also known as reverse faulting, is common for convergent plate boundaries where two tectonic plates are moving towards each other producing horizontal compressive stresses at these plate boundaries. Normal faulting is seen at divergent plate boundaries where the tectonic plates are moving away from each other producing horizontal tensional stresses. Strike-slip faulting is found at transform plate boundaries where the tectonic plates are moving laterally past each other due to the shear stress across these boundaries, which produces strong horizontal stress in one direction and weak horizontal stress in the perpendicular direction.

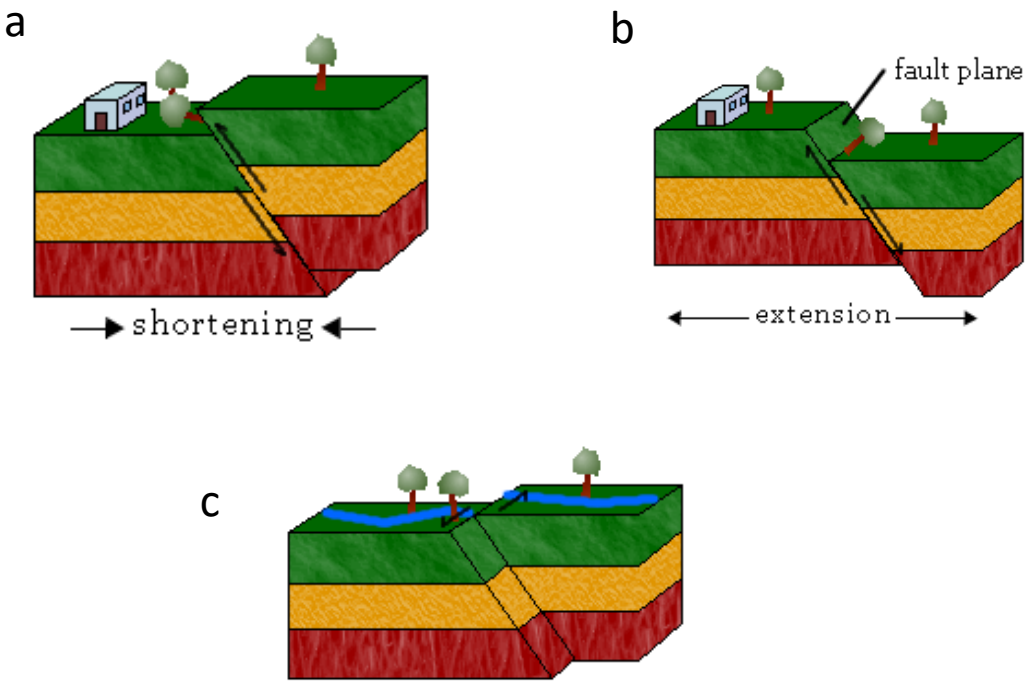

Figure 2.1. Three basic types of faulting a) Thrust faulting b) Normal faulting c) Strike slip faulting. [Figure: *http://kiska.giseis.alaska.edu*]

2.2 EARTHQUAKE LOCATION

Location of an earthquake is represented by its hypocenter or focus, which is the point in the earth where the shear rupture of the fault begins. The hypocenter of an earthquake is defined by three parameters: latitude, longitude and focal depth. The latitude and longitude of an earthquake hypocenter define a point called the epicenter, which is the surface projection of the hypocenter. The vertical distance between the hypocenter and the epicenter is called the focal depth of the earthquake (also called the earthquake depth). Figure 2.2 gives a schematic diagram showing the hypocenter, epicenter and focal depth of an earthquake.

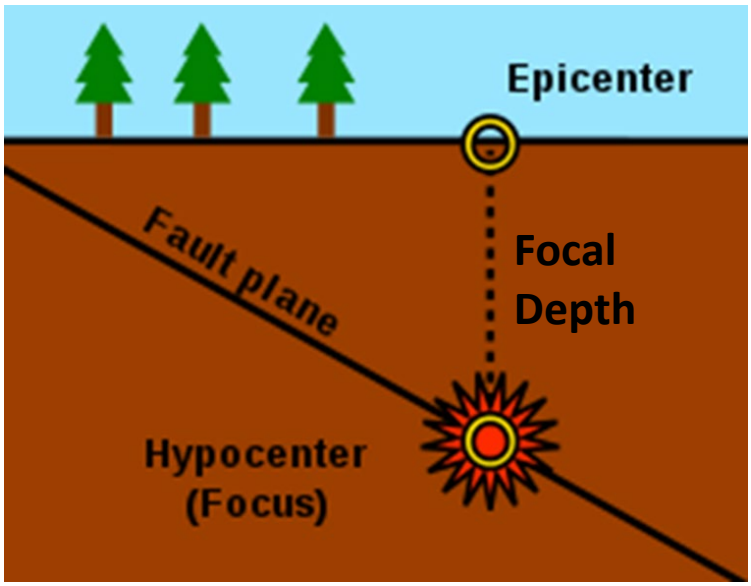

Figure 2.2. Location of an earthquake.

2.3 EARTHQUAKE MAGNITUDE

Earthquake magnitude is a number that characterizes the relative size of an earthquake. Many earthquake magnitude scales are available and are used in practice today (*https://www.bgs.ac.uk/discoveringGeology/hazards/earthquakes/magnitudeScaleCalculations.html*). Magnitudes are generally determined by identifying a specific type of seismic wave (called a seismic phase) in an earthquake waveform and measuring some of its characteristic properties such as amplitude, frequency, duration or timing. The type of earthquake magnitude scale used to measure the size of an earthquake depends on the information available and the type of seismic event for which the magnitude scale was developed. The different magnitude scales that describe the magnitudes of the earthquakes used in this dissertation are defined as follows:

2.3.1 LOCAL MAGNITUDE (ML or M_L):

The local magnitude scale, commonly referred to as the "Richter magnitude", was the first earthquake magnitude scale. It was developed by Charles Richter and is described in *Richter (1935)*. M_L is based on the logarithm of the ratio of the largest earthquake amplitude to the amplitude of the smallest detectable wave along with a correction factor that is a function of epicentral distance (surface distance from the epicenter to the recording station) to provide an extrapolation of this ratio to the earthquake epicenter. $M_L = \log_{10} [A(\delta) / A_0(\delta)]$

where

$A(\delta)$ – the measure of the highest amplitude of the earthquake wave measured at epicentral distance ‘δ’ from the earthquake source.

$A_0(\delta)$ – the amplitude of the smallest detectable wave (or standard wave) measured at distance ‘δ’ from an earthquake source.

The Richter magnitude is designed to give approximately the same M_L value for all seismic stations where the magnitude is computed. *Richter (1935)* recommended that the magnitudes from all the stations be averaged to find the final local magnitude value. Richter designed the M_L magnitude scale to be used with readings from a Wood-Anderson seismometer (a specific kind of seismometer in use at that time). As Richter developed this magnitude scale working with earthquakes form Southern California, the attenuation of seismic waves in Southern California is implicit in Richter’s original scale. People have modified the original Richter scale for other parts of the world (e.g., Ebel, 1982).

2.3.2 SURFACE WAVE MAGNITUDE (M_S)

The surface-wave magnitude was developed by *Gutenberg (1942)*. This magnitude scale utilizes surface waves with periods about 20 seconds (which have large trace amplitudes for most distant earthquakes) to calculate the magnitude of an earthquake. This magnitude scale was developed to extend Richter’s original magnitude scale concept to distant

earthquakes (known by seismologists as teleseisms) on a global scale, since Richter's M_L scale was not able to give the accurate magnitude estimates for teleseismic earthquake signals. The M_s scale works for shallow teleseismic earthquakes (less than about 50 km depth) which usually generate strong 20-second surface waves.

2.3.3 BODY WAVE MAGNITUDE (m_b)

The body wave magnitude scale was developed by *Gutenberg (1945)* and *Gutenberg and Richter (1956)* in order to overcome the distance and magnitude limitations present in the M_L scale and to provide magnitude values for deep teleseismic earthquake signals that have little or no surface-wave energy at 20-sec period. The m_b magnitude scale utilizes the first 10 seconds or so of the seismograms to estimate the magnitude of an earthquake. The magnitude obtained using this scale depends on the amplitude and period of the body-wave signal that is measured as well as the epicentral distance and the focal depth of the earthquake.

2.3.4 NUTTLI MAGNITUDE (m_{bLg} or M_N)

The Nuttli magnitude scale was developed from the amplitude of guided Lg waves for application in the central and eastern U.S. Lg waves are a group of seismic phases observed at regional distances and are caused by superposition of multiple S-wave reverberations and S to P and/or P to S conversions within the crust (*Knopoff et al., 1973)*. As stated in

Section 2.3.1, the attenuation of seismic waves in Southern California is implicit in Richter's original scale. The attenuation in the central and eastern U.S. is less than that in Western U.S. (*Necioglu and Nuttli, 1971*). To address this issue, the m_{bLg} scale was developed by *Nuttli (1973)* for earthquakes in the central and eastern part of North America. The scale is expressed in the following equations:

$$m_{bLg} = 3.3 + 1.66*\log_{10}(\Delta) + \log_{10}(A/T) \qquad (1)$$

for $0.5^o \leq \Delta \leq 4^o$

$$m_{bLg} = 3.3 + 1.66*\log_{10}(\Delta) + \log_{10}(A/T) \qquad (2)$$

for $4^o \leq \Delta \leq 30^o$

where

'Δ' is the epicentral distance in degrees

'A/T' is the zero-to-peak amplitude of the Lg waves expressed in microns per seconds.

The constants in Equations (1) and (2) were obtained using Lg waves with period T = 1 sec.

2.3.5 MOMENT MAGNITUDE (M_w):

The conventional magnitude scales such as local magnitude (M_L), surface magnitude (M_s) and body magnitude (m_b) underestimate the magnitudes of the largest earthquakes, also called the magnitude saturartion (for example, *Howell, 1981*). In order to address the issue

of magnitude saturation, *Hanks and Kanamori (1979)* developed the moment magnitude scale M_w. The M_w magnitude scale is directly related to the energy released during an earthquake and no saturation is observed in earthquake magnitudes using this scale. M_w is calculated from the scalar seismic moment (M_0) of an earthquake and is defined as in the equation below:

$$M_w = (2/3)*[\log_{10} (M_0)] - 10.7$$

where,

$M_0 = \mu \times A \times D$ in the unit of dyne-cm

with

μ is the shear stress of the rock in dyne/cm^2.

A is the area of the fault that ruptured during an earthquake, also called the fault area, measured in cm^2.

D is the average slip observed during an earthquake, also called as the displacement of the fault measured in cm.

2.3.6 DURATION MAGNITUDE (M_D) AND MODIFIED DURATION MAGNITUDE (M_D*)

Duration magnitude was first proposed by *Bisztricsany (1958)*. This magnitude scale is based on the total duration of the seismic wave train, where the end of the waveform is

called the seismic coda. *Bisztricsany (1958)* defined the coda duration as the time interval between the onset of the first seismic wave and the time when the wave amplitude diminishes to the 10% of its maximum recorded value. A duration magnitude (M_D) scale for the Central and Southern Appalachians, derived from the duration of an earthquake signal measured in seconds on a 1 Hz instrument is defined by the following equation (*Wu et al., 2015*):

$$M_D = 2.83[\log_{10}(t_d)] - 3.42$$

where,

't_d' is the time duration from the P-wave onset until the time when the amplitude of the signal becomes equal to the pre-event noise amplitude.

As observed by (*Wu et al., 2015*) for the aftershocks of M_w 5.7 2011 Mineral Virginia earthquake, this M_D magnitude scale overestimates the magnitudes of small earthquakes recorded at stations at less than 10 km epicentral distance and, for this reason a modified duration magnitude was determined, which is defined as follows:

$$M_D^* = \log_{10}(R \times A) - 4.2$$

where,

R is the hypocentral distance in kilometers, and

A is the averaged three-component peak trace amplitude in digital counts on a short period instrument.

2.4 WAVE EQUATION

The homogeneous equation of motion for an isotropic elastic medium can be written as (*Stein and Wysession, 2003*):

$$\sigma_{ij,j}(r,t) = \rho \frac{\partial^2 u_i(r,t)}{\partial t^2} \qquad (3)$$

where,

σ_{ij} is the stress tensor

ρ= density of the medium, and

In terms of elastic constants, Hooke's Law for an isotropic medium can be written as:

$$\sigma_{ij} = \lambda\theta\delta_{ij} + 2\mu e_{ij} \qquad (4)$$

where

λ= Lame's first constant, μ=shear modulus of the medium, $\delta ij = 1\ for\ i = j\ and\ zero\ otherwise,\ and\ \sigma_{ij}$ is the strain tensor.

For a displacement u, θ is the dilatation defined as:

$$\theta = \nabla . u \qquad (5)$$

Using Equations (3), (4) and (5) and the definition of the Laplacian operator, the three dimensional homogeneous equation of motion for a linear isotropic elastic medium can be written as:

$$(\lambda + 2\mu)\nabla\big(\nabla . \mathrm{u}(\mathrm{r},\mathrm{t})\big) - \mu\nabla \times (\nabla \times \big(\mathrm{u}(r,\mathrm{t})\big) = \rho \frac{\partial^2 u(r,t)}{\partial t^2} \qquad (6)$$

and the inhomogeneous equation of motion can be written as:

$$(\lambda + 2\mu)\nabla\big(\nabla.\mathrm{u}(\mathrm{r},\mathrm{t})\big) - \mu\nabla \times (\nabla \times \big(\mathrm{u}(r,\mathrm{t})\big) - \ \rho\frac{\partial^2 u(r,t)}{\partial t^2} \ = \ f(r,t) \qquad (7)$$

where u(r,t) is the displacement produced at point (r = r, t = t) due to a source at point (r = 0, t = 0). f (r,t) is the source term.

The displacement field in Equation (7) can be expressed as the sum of the gradient of a scalar potential (ϕ(x,t)) and the curl of a vector potential (γ(x,t)).

$$u(r,t) = \nabla\emptyset(r,t) + \ \nabla \times \gamma(r,t) \qquad (8)$$

Solving equations (3), (4) and (8) gives the scalar wave equation

$$\nabla^2\emptyset(r,t) - \left(\frac{\rho}{\lambda+2\mu}\right)\frac{\partial^2\emptyset(r,t)}{\partial t^2} = \ f(r,t) \qquad (9)$$

Equation (9) is the wave equation for a P wave with the P wave velocity

$$\alpha = \sqrt{\frac{\lambda+2\mu}{\rho}}$$

The solution of equation (9) is given by:

$$\emptyset(r,t) = A\exp(i[\omega t - \boldsymbol{k}.\boldsymbol{r}]) \ ,$$

where, the constant A is a scalar amplitude and **k** is the wave number vector.

P-waves, also called pressure waves, are longitudinal body waves. These waves alternately expand and compress the material through which they travel. Due to the continuous

expansion and compression, materials undergo volume change when P-waves travel through them. As shown in Figure 2.3, the direction of particle motion for a P-wave is in the direction of the propagation of the wave. P-waves can travel through a solid medium as well as through a fluid. These are the fastest travelling waves among all the seismic waves and therefore are recorded as the first arrivals on seismograms.

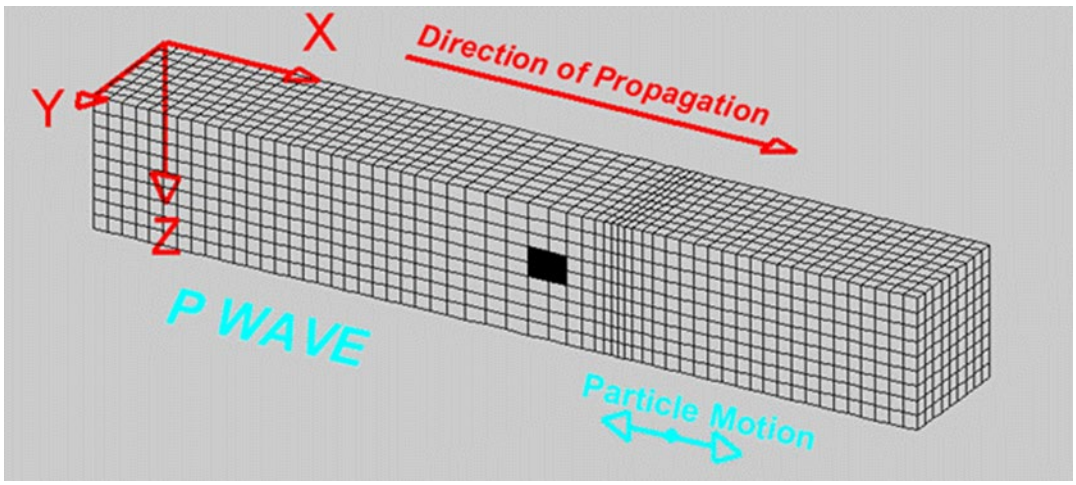

Figure 2.3. Displacement produced by P-wave shown at a snapshot in time. [Figure: *http://web.ics.purdue.edu*]

Solving equations (7) and (8), also gives the vector wave equation

$$\nabla^2\gamma(r,t) - \left(\frac{\rho}{\mu}\right)\frac{\partial^2\gamma(r,t)}{\partial t^2} = f(r,t) \qquad (10)$$

Equation (10) is the wave equation for an S wave with the S wave velocity

$$\beta = \sqrt{\frac{\mu}{\rho}}$$

S-waves, also called shear waves, are the transverse body waves. The direction of the particle motion for S-waves is perpendicular to the direction of the propagation of the wave (see Figure 2.4). The direction in which S-waves move the ground depends on the polarization of the S-wave vector and the direction of travel of the wave. Horizontally polarized S-waves (also called as SH waves) move the ground side to side whereas vertically polarized S-waves (also called as SV waves) can move the ground side to side as well as up and down. Both SH and SV waves are defined in relation to the orientation of the local surface. S waves travel through solids but cannot travel through fluids. S-waves travel slower than the P-waves and arrive later than P waves on seismograms.

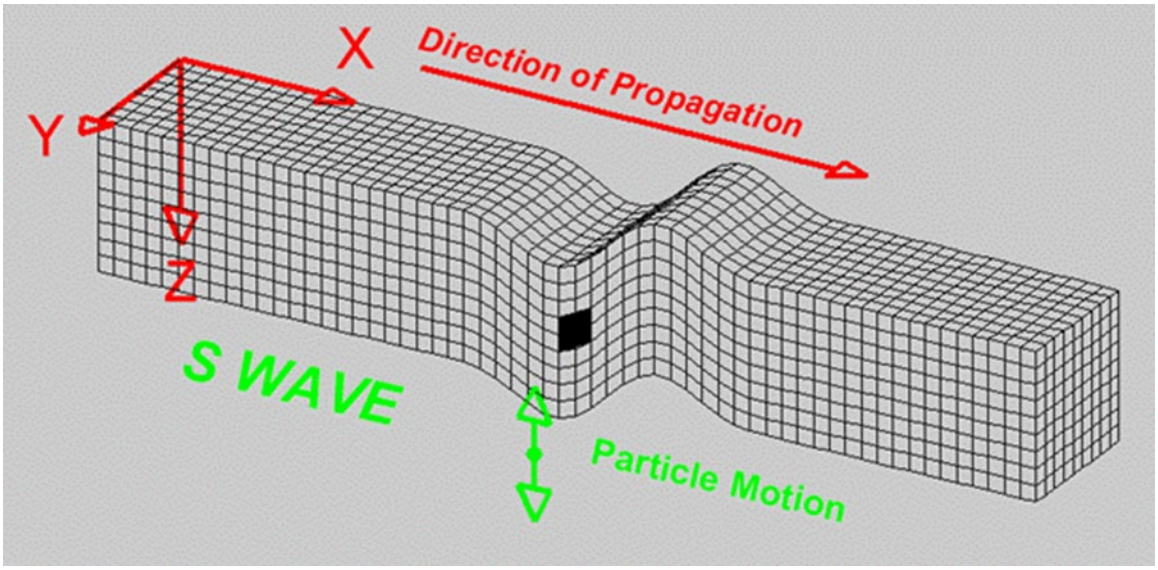

Figure 2.4. Displacement produced by S-wave shown by a snapshot in time. [Figure: *http://web.ics.purdue.edu*]

2.5 SURFACE WAVES

Surface waves are generated near the surface of the earth and can be thought of as a result of the interaction of body waves with the surface of the earth. These waves travel slower than the body waves so are observed after the P and S waves in a seismogram. Surface waves come in two forms 1) Rayleigh waves and 2) Love waves.

Rayleigh waves are composed of P and SV waves. These waves roll the ground as the particles in the medium are set into retrograde elliptical motion by the waves as shown in Figure 2.5. A Rayleigh wave can exist at the top of a homogeneous half space and it has an apparent wave velocity that is always less than the shear wave velocity (β) in half space. For a homogeneous Poisson solid ($\alpha = \sqrt{3}\,\beta$), the apparent velocity is (0.92β). These waves appear both in the vertical and radial components of the seismograms. For a medium with multiple velocity layers, Rayleigh waves are dispersive in nature.

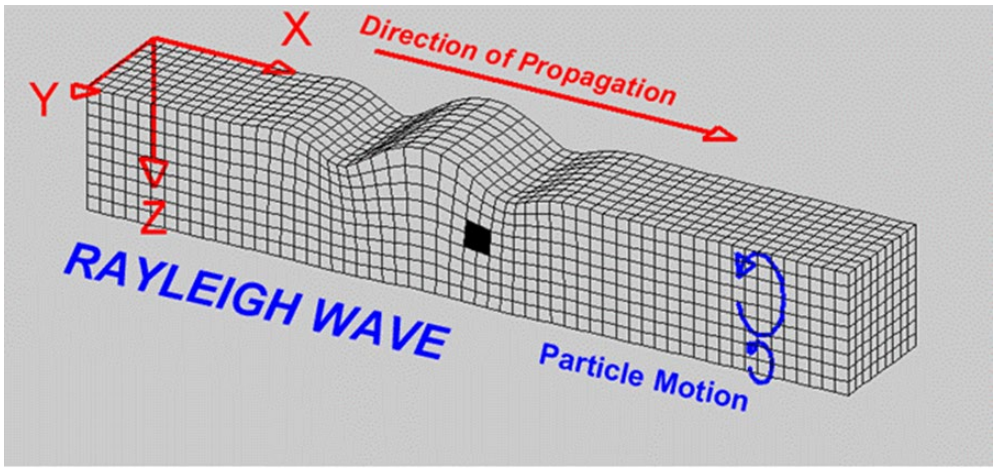

Figure 2.5. Displacement produced by Rayleigh-wave shown at a snapshot in time.

[Figure: *http://web.ics.purdue.edu*]

Love waves are the result of the interaction of SH waves with the surface of the earth. The particle motion for a Love wave is similar to that of an SH wave. It is parallel to the earth's surface and perpendicular to the direction of the propagation of the wave as shown in Figure2.6. Love wave exists only if there are one or more layers in between the half space and the surface. The apparent velocity for a Love wave is less than that of the shear wave velocity in the half space. Love waves are inherently dispersive in nature.

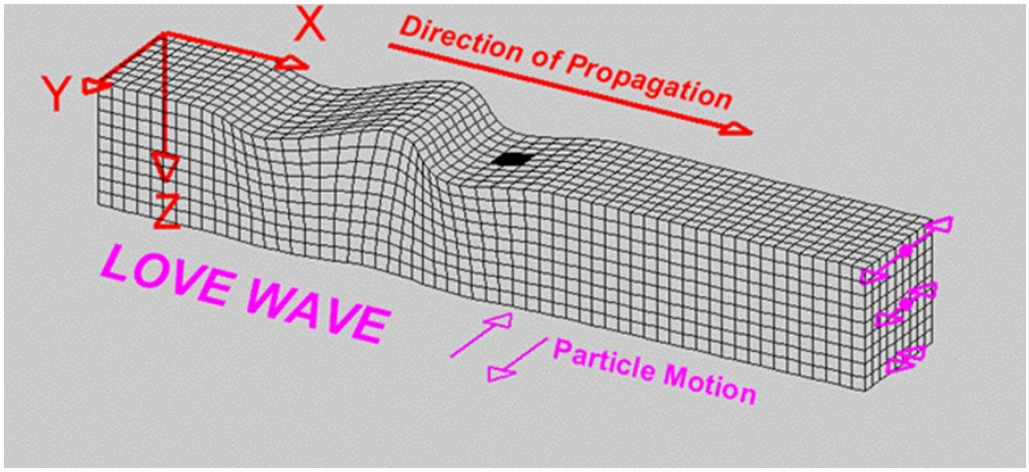

Figure 2.6. Displacement produced by Love-wave shown at a snapshot in time. [Figure: *http://web.ics.purdue.edu*]

2.6 Lg WAVE

The Lg wave is one of the prominent seismic phases observed in the high frequency seismograms in a continental setting. The Lg wave can either be understood as the sum of the higher mode surface waves or the reverberations of multiply reflected and refracted S waves trapped within the crust, including S to P and P to S conversions (*Knopoff et al., 1973; Bouchon, 1982*). Lg waves can be dispersive (Bath, 1954; *Bouchon, 1982*). Since Lg waves are trapped within the crust, the amplitudes of Lg waves are very sensitive to crustal heterogeneities (*Bouchon, 1982*). These waves have particle motions in all three directions and appear in all three components of seismograms. Lg waves attenuate with distance as other seismic waves, with more attenuation observed in the oceanic crust than in the continental crust (*Knopoff et al., 1973*).

2.7 HEAD WAVES

(The description provided in this section is based on the explanation of Stein *and Wysession (2003)*).

A head wave is a wave-propagation effect due to the structure of the seismic velocities with depth in the earth. Head waves are horizontally refracted body waves (P and S), and they require a source and a receiver in a lower velocity medium (V_0) which lies above a higher velocity medium (V_0) as shown in Fig 2.7. Three basic ray paths from the source to the receiver for a low velocity layer over a high velocity layer are shown in Figure 2.7. For a surface source shown in Figure 2.7, the direct wave travels through the low-velocity layer

to the surface receiver directly from the source. The reflected wave travels downward at an angle through the layer and is reflected at the interface between the two layers to reach the receiver. The head wave is incident on the interface at the critical angle 'i_c', and undergoes refraction to travel horizontally along the top of the lower layer. As the head wave travels horizontally along the interface between the two layers, it continuously radiates energy back into the top layer where that energy can travel upward to the receiver.

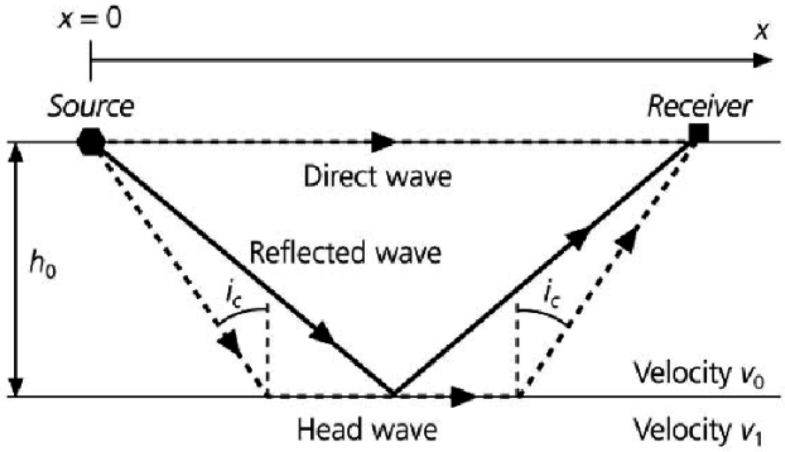

Figure 2.7. Three basic ray paths for a layer over a halfspace. [Figure: *Stein and Wysession, 2003*]

A travel-time versus the source-to-receiver distance plot for the three ray paths illustrated in Figure 2.7 is shown in Figure 2.8. The plot of Figure 2.8 is obtained, for example, through the acquisition of data in a seismic refraction survey for a surface source and a linear array of surface receivers. The first arrivals at the surface receivers with source-receiver distances less than the crossover distance (x_d) are the direct waves, whereas the head waves replace the direct waves as the first arrivals at distances beyond the crossover distance. No refracted waves appear until a distance called the critical distance (x_c). As head waves are the refracted waves, they start to appear only after the critical distance. Both the crossover distance and the critical distance are functions of the velocities of the layers as well as of the thickness of the lower velocity layer.

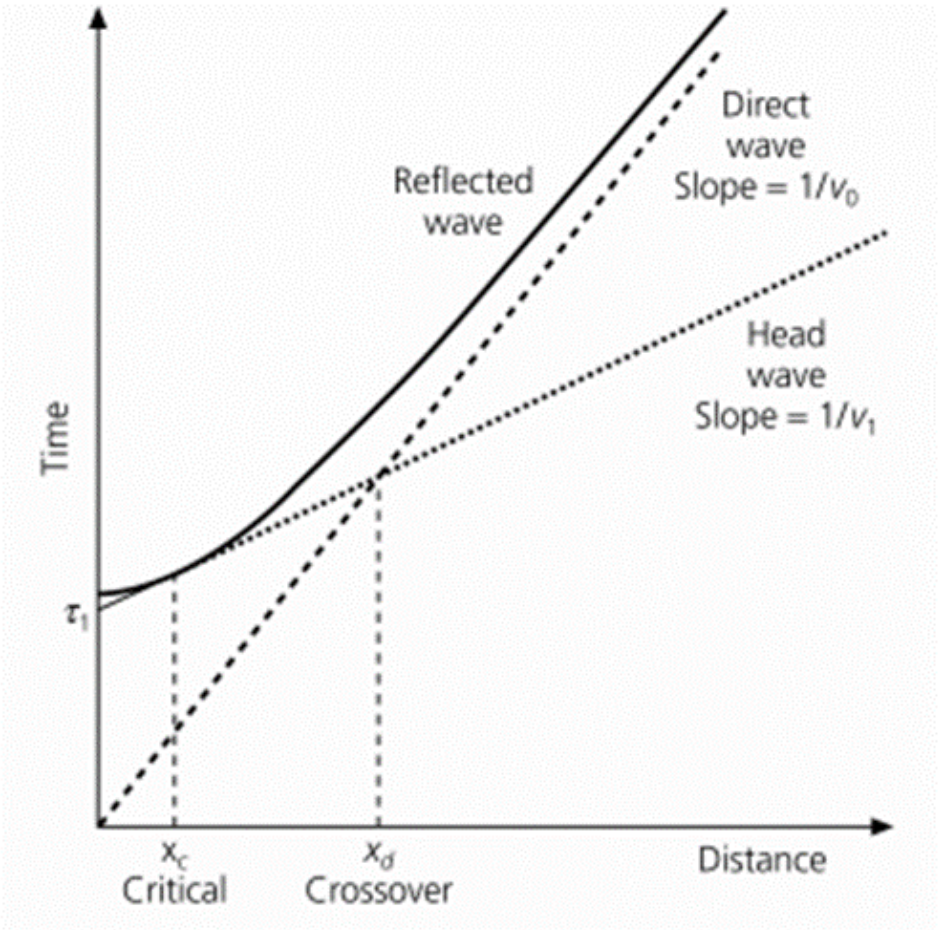

Figure 2.8. Travel time versus receiver-to-source distance curves for the three basic ray paths in Figure 2.7. [Figure: *Stein and Wysession, 2003*]

2.8 FAULT GEOMETRY

The geometry of an earthquake fault is quantified in terms of the orientation of the fault plane and the direction of the slip on that fault plane. An example of a planar earthquake fault plane is shown in Figure 2.9 with n as the normal vector to the fault plane and d as the slip vector that lies on the fault plane. The slip vector is the direction of movement of the overlying material relative to the material that underlies the fault. The orientation of the fault plane is described in terms of the dip angle (δ) and the strike angle (Φ_f) whereas the direction of the slip is given by the slip angle (λ), where these angles are illustrated in Figure 2.9.

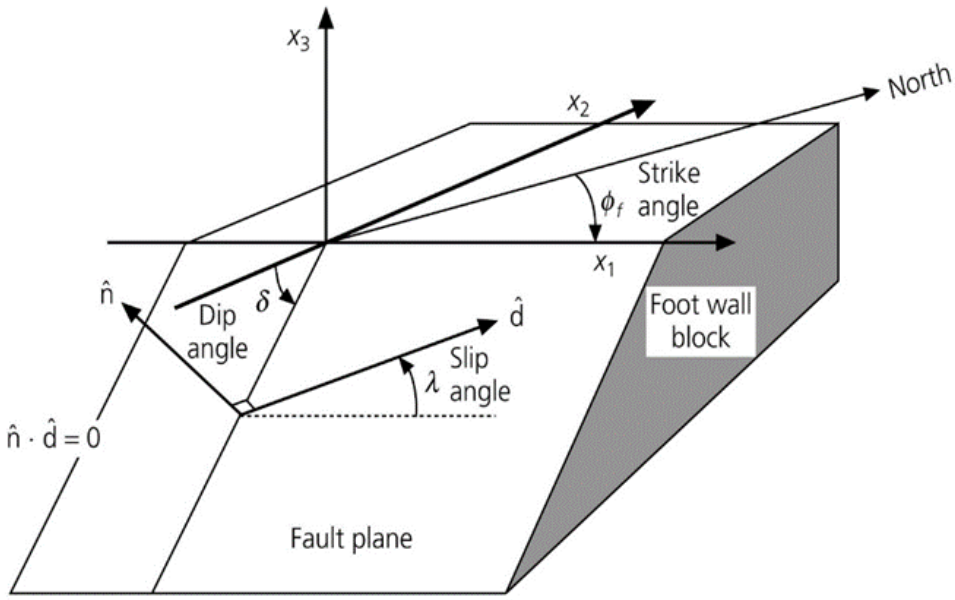

Figure 2.9. Fault geometry for an earthquake. [Figure: *Stein and Wysession, 2003*]

The dip angle is the acute angle between the horizontal surface of the earth and the fault plane and can vary from 0° to 90°. The strike angle is the angle made by the direction of the strike (taken with dip direction perpendicular and to the right of the strike direction) clockwise from geographical north and can vary from 0° to 360°. The slip angle is the angle made by the slip direction with the fault strike as shown in Figure 2.9 and can vary from 0° to 360°.

2.9 FORCES REPRESENTING AN EARTHQUAKE

An earthquake can be described as a slip on a fault caused by a double-couple force system, also called the body forces for an earthquake source (*Burridge and Knopoff, 1964*) as shown in Figure 2.10. Each force couple of a double-couple force system consists of two equal and opposite forces separated by a small distance. The two pairs of force couples are oriented such that the net torque exerted by the double couple force system on the fault is zero. For each earthquake, there are two possible planes on which the faulting may have occurred. One of them is the plane on which the slip occurred and is called the fault plane, whereas the second one is a plane perpendicular to the fault plane and is called the auxiliary plane. Seismic waves from a double-couple point source (a source with negligible spatial extent) do not have information about which of the two planes is the real fault plane. Additional information such as geologic and geophysical information about the trend of the known fault is required to differentiate between the fault plane and the auxiliary plane.

There are nine possible force couples for a seismic source which are the components of a seismic moment-tensor (M). These force couples are shown in Figure 2.11.

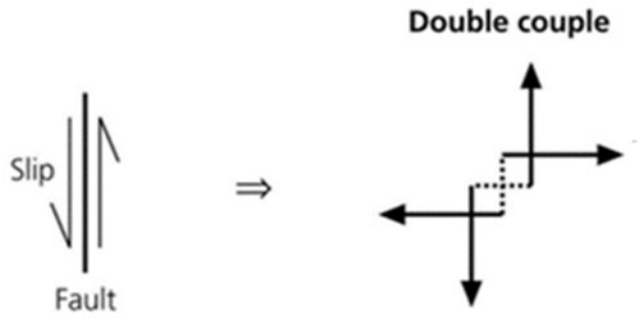

Figure 2.10. Equivalent body force representation for a double couple source. [Figure: *Stein and Wysession, 2003*]

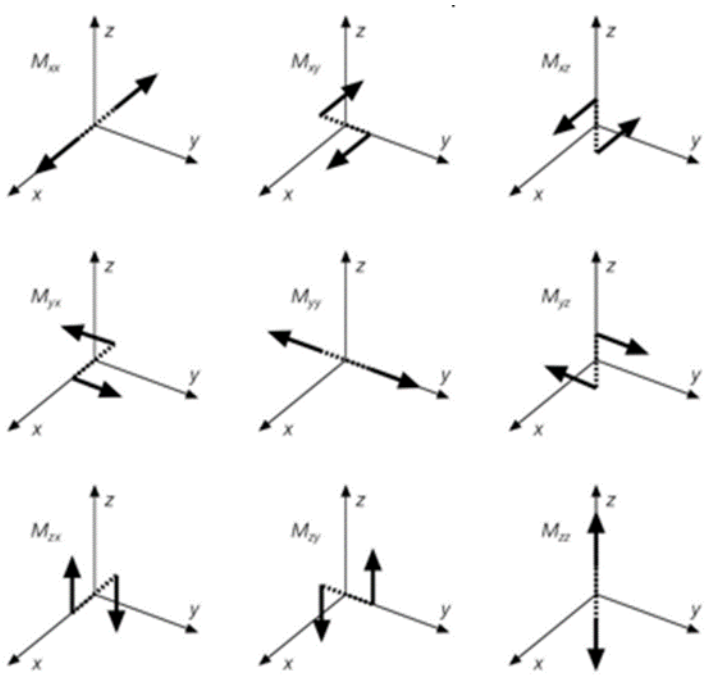

Figure 2.11. Components of seismic moment-tensor. [Figure: *Stein and Wysession, 2003*]

The nine moment-tensor components can be calculated from the scalar moment and the fault angles using the following relations (*Jost and Herrmann, 1989*):

$Mxx = M0\ (\sin(\delta)\cos(\lambda)\sin(2\Phi_f) + \sin(2\delta)\sin(\lambda)\sin(s)\sin(\Phi_f))$

$Myy = -M0\ (\sin(\delta)\cos(\lambda)\sin(2\Phi_f) - \sin(2\delta)\sin(\lambda)\cos(s)\cos(\Phi_f))$

$Mzz = -M0\ (\sin 2\delta \sin \lambda)$

$Mxy = -M0\ (\sin(\delta)\cos(\lambda)\cos(2\Phi_f) + 0.5\sin(2\delta)\sin(\lambda)\sin(2\Phi_f))$

$Mxz = M0\ (\cos(\delta)\cos(\lambda)\cos(\Phi_f) + \cos(2\delta)\sin(\lambda)\sin(\Phi_f))$

$Myz = M0\ (\cos(\delta)\cos(\lambda)\sin(\Phi_f) - \cos(2\delta)\sin(\lambda)\cos(\Phi_f))$

where, M0 is the scalar seismic moment and δ, λ and Φ_f are the fault angles as described in Section 2.5.

As the moment-tensor is a symmetric tensor,

$Myx = Mxy \quad Mzx = Mxz \quad Mzy = Myz$

For a double couple source, as there is no net volume change, the moment-tensor is traceless. To make sure this condition is not violated, Mzz is usually calculated from the following equation:

$Mzz = -(Mxx + Myy)$

Thus, for a double couple source, there are only five independent moment-tensor components.

2.10 P-WAVE FIRST MOTION

The first seismic wave to arrive at a station from a seismic source is always a P-wave. The direction of the first P wave motion (weather it is compressional or dilatational), also called the first motion or the P-wave polarity, varies between the stations located at the different distances and azimuths around a seismic source, with azimuth being the direction from a seismic source to a seismic station measured clockwise from north (*Cronin, 2010*). In Figure 2.12, where a vertical strike slip fault is shown, the first motion polarity divides into four quadrants, two of which are dilatational and the other two are compressional. The planes between the different quadrants are the fault plane and the auxiliary plane. The quadrants which are located such that the material is initially compressed as the P wave travels through them are called the compressional quadrants. The quadrants which are located such that the material initially extended as the P wave travels through them are called the dilatational quadrants. For vertical-component seismic stations, the P-wave first motion is up for the compressional quadrants whereas it is down for the dilatational quadrants.

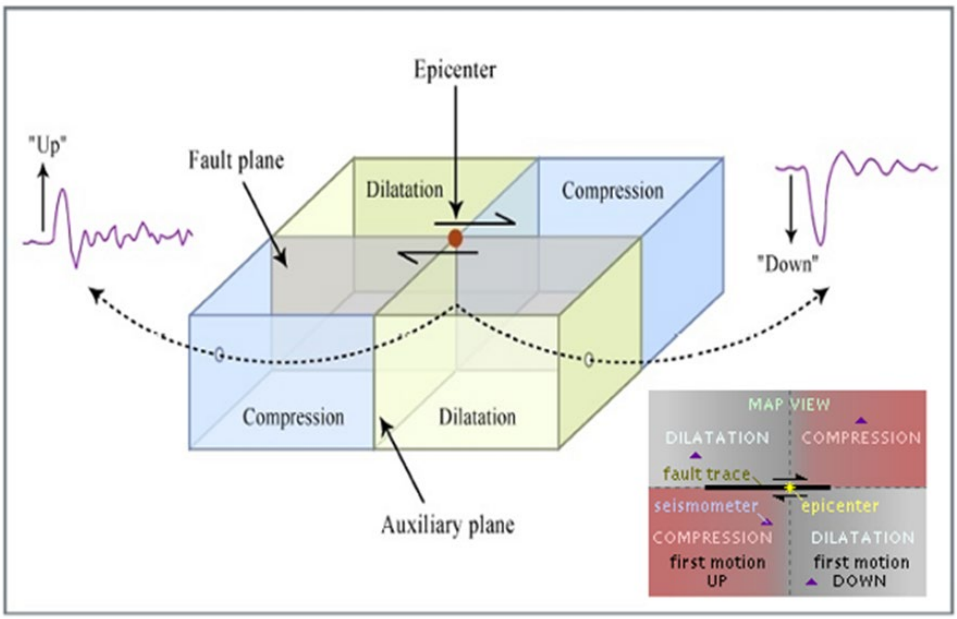

Figure 2.12. P-wave first motions for a vertical strike-slip fault. [Figure: modified from *Stein and Wysession, 2003*]

2.11 RADIATION PATTERN

The radiation pattern of an earthquake describes the spatial pattern of the amplitudes of the initial P and S wave movements as received by receivers distributed in all possible directions around a double couple source, as shown in Figure 2.13. The description provided in this section is based on the explanation of *Stein and Wysession (2003)*. Figure 2.13(a) defines a spherical coordinate system relative to Cartesian axes x_1, x_2 and x_3. Figure 2.13(b) represents a double couple force system oriented along the x_1- and x_3-axes such that the x_1-x_2 plane represents the fault plane (Figure 2.13(c)) and the x_2-x_3 plane represents an auxiliary plane (Figure 2.13(d)), with the x_1 axis containing the slip vector on the fault plane, the x_3-axis containing a normal vector perpendicular to the fault plane and the x_2-axis being perpendicular to both the x_1 and x_3 axes, with the x_2-axis also being called the null axis. The P and S displacements produced by the earthquake are zero on the null axis. The radiation pattern for a P wave is given by Equation (11) whereas the radiation patterns for the two perpendicular components of an S wave are given by Equation (12) and Equation (13).

$$u_r = \frac{1}{4\pi\rho\alpha^3 r}\left[\mathrm{M}(t - \frac{r}{\alpha})sin2\theta cos\phi\right] \qquad (11)$$

$$u_\theta = \frac{1}{4\pi\rho\beta^3 r}\left[\mathrm{M}(t - \frac{r}{\beta})cos2\theta cos\phi\right] \qquad (12)$$

$$u_\phi = \frac{1}{4\pi\rho\beta^3 r}\left[\mathrm{M}(t - \frac{r}{\beta})(-cos\theta sin\phi\right) \qquad (13)$$

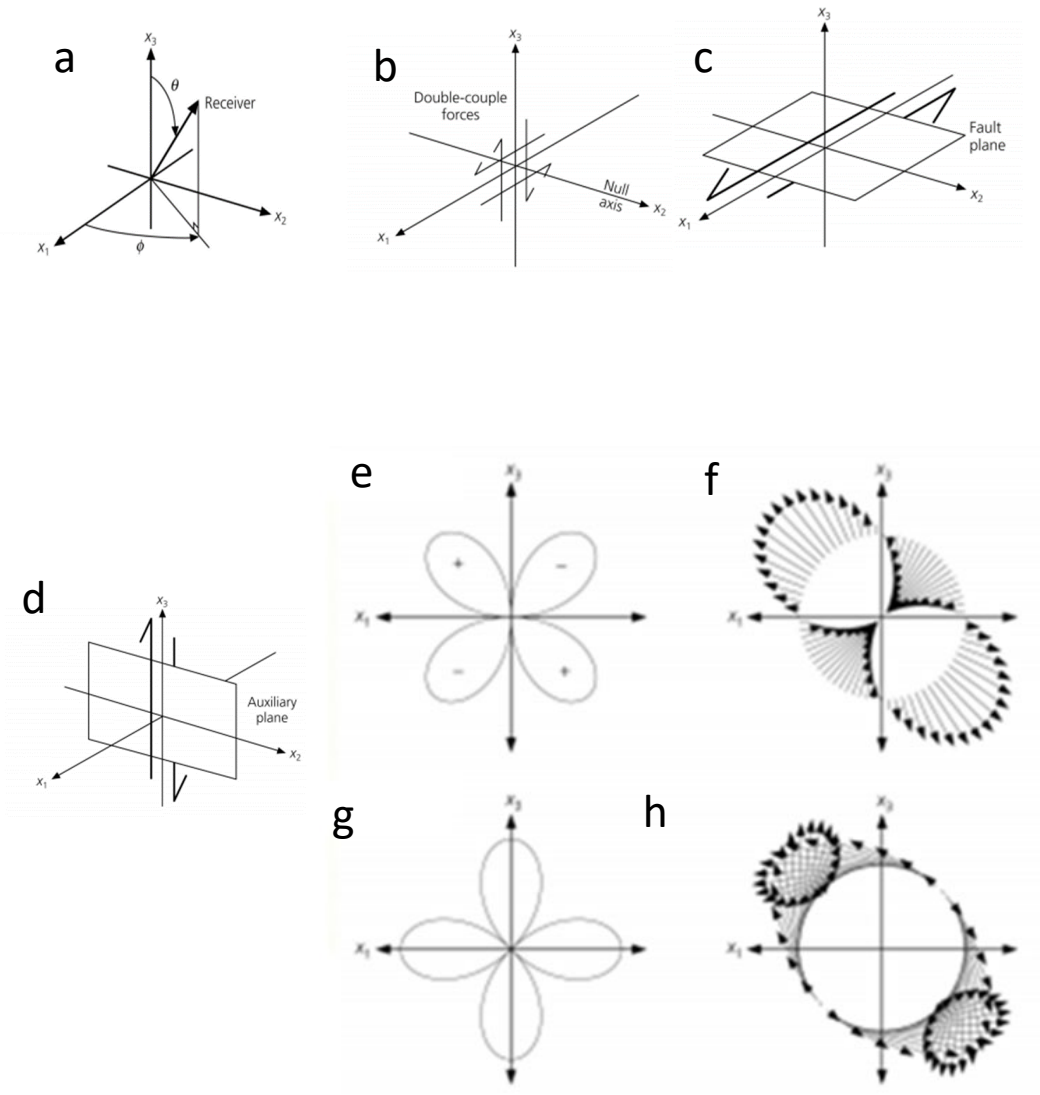

Figure 2.13. a) A spherical coordinate system relative to Cartesian Cartesian axes x_1, x_2 and x_3. b) A double couple force system. c) Fault plane d) Auxilliary plane. e) and f) P-wave radiation pattern. g) and h) S-wave radiation pattern. [Figure: *Stein and Wysession, 2003*]

The first term $\frac{1}{4\pi\rho\alpha^3 r}$ in Equation (11) gives the amplitude of the P-wave in an infinite medium in which the amplitude decays as 1/r where 'r' is a distance from the source. The second term $\mathrm{M}(t - \frac{r}{\alpha})$ is called the source time function and gives the pulse radiated from the source which travels with P-wave velocity 'α' and arrives at distance 'r' at time (t - r/ α). The third term 'sin2θcosΦ' controls the radiation pattern for the P wave. The P-wave radiation pattern is four lobed with two compressional quadrants (indicated by + signs in Figure 2.13(e)) and two dilatational quadrants (indicated by - signs in Figure 2.13(e)). The P-wave displacement is maximum mid-way between the two nodal planes whereas it is minimum (zero) on the nodal planes (Figure 2.13(e)). The particle motion for a P wave is away from the source for the compressional quadrants and towards the source for the dilatational quadrants (Figure 2.13(f)).

The S-wave displacement has two components given in Equation (12) and Equation (13). The total S-wave displacement can be calculated as $u_\theta \hat{\mathrm{e}}_\theta + u_\phi \hat{\mathrm{e}}_\phi$. The first and the second terms in these equations have similar meanings to that in Equation (11) but now applied to an S wave with velocity 'β'. The S-wave radiation pattern is also four lobed but with displacement being maximum on the nodal planes and minimum mid-way between the nodal planes (Figure 2.13(g)). The particle motion for an S wave diverges away from the center of the dilatational quadrants and converges towards the center of the compressional quadrants (Figure 2.13(h)).

2.12 FOCAL MECHANISM

The term focal mechanism is used as the name of the graphical representation of the fault geometry of an earthquake. The focal mechanism of an earthquake is generally displayed on a hemispheric plots of the P-wave first-motion patterns, often with the compressional quadrants colored black (or colored other than white) and the dilatational quadrants colored white (*Cronin, 2010*). A stereographic projection transforming a hemisphere (typically either the upper hemisphere or the lower hemisphere) to a plane is used to generate these plots. The two nodal planes (which are seen as straight or curved lines when projected onto the plane) separate the compressional and the dilatational regions. An example of a focal mechanism plot is given in Figure 2.14.

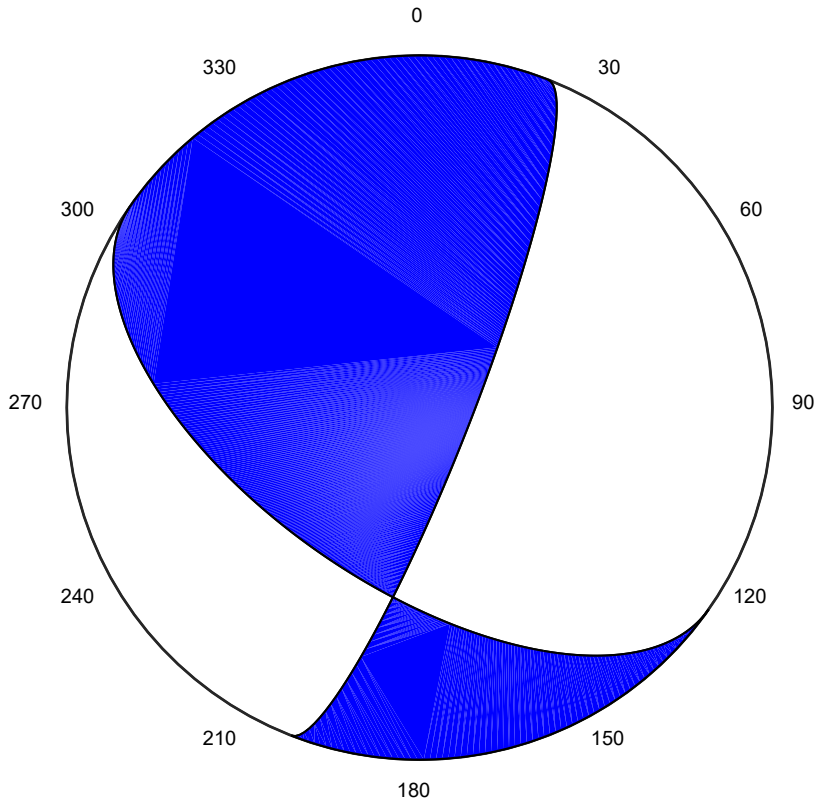

Figure 2.14. Focal mechanism plot showing oblique thrust faulting with dip = 45°, rake = 19°, and strike = 125°. The two quadrants colored blue are the compressional quadrants and the remaining two colored white are the dilatational quadrants.

2.13 GREEN'S FUNCTIONS

Green's functions are the solutions of the inhomogeneous wave equation described by Equation (1) in the Section 2.4 for seismic waves that propagate through an earth model. A Green's function represents a signal that arrives at a seismometer if the source is a delta function in space and if the time function of the source is a delta function. The Green's function includes elastic and inelastic effects of the structure on the seismic waves as they propagate from the source to the receiver and can be written as (*Arfken, 1985*):

$$G(t) = E(t)*Q(t)$$

where E(t) is the elastic response of the medium between the source and the receiver and Q(t) is the inelastic effect of the propagating seismic waves. The '*' represents temporal convolution of the functions E(t) and Q(t).

There are 10 different Green's functions that are needed to completely define the seismic energy released from a seismic source (*Jost and Herrmann, 1989*). Eight of these 10 Green's function arise from a double-couple source whereas the remaining two describe a volume change source that can take place during some kinds of seismic events such as explosions or implosions. All possible orientations of shear sources (such as earthquake faulting events) can be described by a combination of the three types of sources (faults), namely; a strike-slip fault, a vertical dip-slip fault and a 45°–dip-slip fault. The Green's functions for each of these sources are as listed below:

Strike Slip:

- Tangential strike slip (TSS)
- Radial strike slip (RSS)
- Vertical strike slip (ZSS)

Dip Slip:

- Radial dip slip (RDS)
- Vertical dip slip (ZDS)

45^0 - Dip Slip

- Tangential 45^0-dip slip (TDD)
- Radial 45^0-dip slip (RDD)
- Vertical 45^0-dip slip (ZDD)

2.14 SYNTHETIC SEISMOGRAMS

Synthetic seismograms are theoretical representations of the variations in the displacement with time produced at a given point on the surface of the earth by an assumed seismic source after the seismic energy has propagated through an assumed earth model. .In seismology, a synthetic seismogram for a single seismic receiver has three components: the tangential synthetic seismogram (S_T), the radial synthetic seismogram (S_R) and the vertical synthetic seismogram (S_V). The tangential synthetic seismogram describes the ground motion tangentially (clockwise or anticlockwise) around the source, the radial synthetic seismogram describes the ground motion radially (outward away from or inward toward) the source, and the vertical synthetic seismogram describes the ground motion (up

or down) in the vertical direction. Synthetic seismograms for a point source in space and time are obtained by combining the Green's functions with the appropriate moment-tensor components. The following relations are used to calculate synthetic seismograms from the Green's functions generated for a double couple source (*Jost and Herrmann, 1989*):

$$S_T = (((Mxx-Myy)/2)\sin(2Az)-Mxy\cos(2Az))TSS - (Mxz\sin(Az)-Myz\cos(Az))TDS$$

$$S_R = Mxx(RDD/2 - RSS\cos(2Az)/2) + Myy(RDD/2 + RSS(\cos(2Az)/2) - Mxy(RSS\sin(2Az) + MxzRDS\cos(Az) + MyzRDS\sin(Az)$$

$$S_Z = Mxx(ZDD/2 - ZSS\cos(2Az)/2) + Myy(ZDD/2+ZSS\cos(2Az)/2) -MxyZSS\sin(2Az)+ MxzZDS\cos(Az)+ MyzZDS\sin(Az)$$

2.15 OBSERVED SEISMOGRAM

The displacement versus time graph produced by a real earthquake as measured by a seismograph is called as an observed seismogram. An example of an observed seismogram with several different seismic phases labeled is provided in Figure 2.17. The first seismic phase that reaches a seismic station is always the P wave, which is followed by the S wave, surface waves and the coda waves.

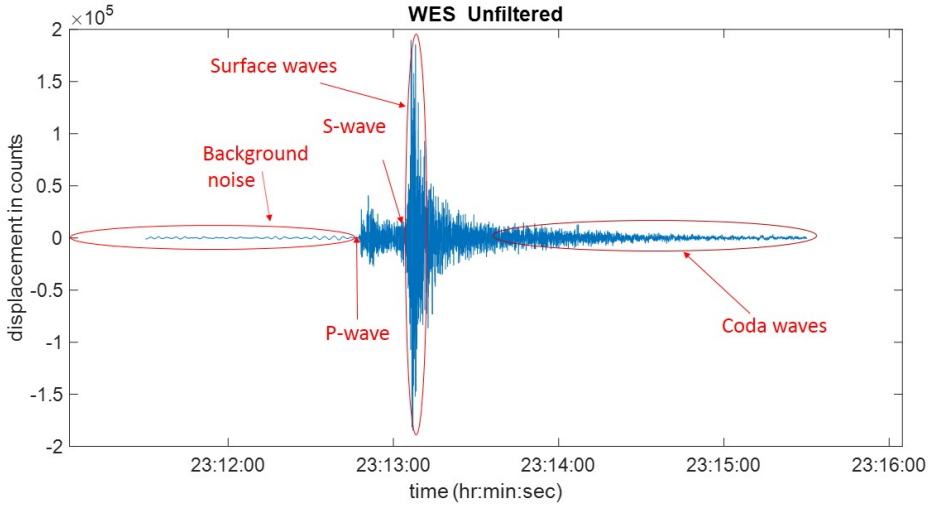

Figure 2.15. Unfiltered vertical component seismogram of the M_w 4.3 Maine earthquake with origin time: 2012/10/16 23:12:22 UTC as measured at Weston Observatory.

2.15 MOMENT TENSOR INVERSION

The concept of a moment-tensor was first suggested by *Gilbert (1973)*. The process of inverting seismograms to find the moment-tensor that produces synthetic seismograms that best match observed seismograms is called moment-tensor inversion (*Langston, 1981; Dreger and Helmberger, 1990*). The moment-tensor obtained through an inversion of observed seismograms is used to obtain the best estimates of the source parameters of an earthquake. The set of equations that relate the moment-tensor to the observations is

$$\mathbf{U=GM} \qquad (14)$$

where, U is a vector composed of observed seismograms, G is a matrix of Green's function and M is the moment-tensor.

As **G** is not a square matrix it cannot be inverted by standard matrix inversion methods to find the matrix $\mathbf{M} = \mathbf{G}^{-1}\mathbf{U}$. To find M for this case Equation (14) is left multiplied by the transpose of **G** (i.e.$\mathbf{G}^{\mathbf{T}}$) to get $\mathbf{G}^{\mathbf{T}}\mathbf{G}$ which is a square and thus an invertible matrix. This new matrix can be inverted it to obtain the moment-tensor **M** as shown by Equation (15).

$$\mathbf{G^TU=G^TGM}$$

$$\mathbf{M= (G^TG)^{-1}G^TU} \qquad (15)$$

This inversion is possible because the seismogram has a linear relationship with the Green's functions. When the envelopes of the seismograms are used in place of the seismograms themselves, the inversion scheme must be modified because as the envelopes of the seismograms do not have a linear relationship with the envelopes of the Green's

function. For the case of synthetic and observed envelopes, Equation (14) can be re-written as

$$\mathbf{U}(\boldsymbol{x},\boldsymbol{t}) = \boldsymbol{G}(\boldsymbol{x},\boldsymbol{t})\,\boldsymbol{M} = \mathbf{S}(\mathbf{x},\mathbf{t}) \qquad (16)$$

where **S** is a vector of synthetic seismograms.

In terms of envelopes, we can write as:

$$\mathbf{U}'(\boldsymbol{x},\boldsymbol{t}) = \boldsymbol{S}'(\boldsymbol{x},\boldsymbol{t})$$

where ***U'*** is envelope of **U** and ***S'*** is envelope of ***S.***

Suppose that **Uo** is collection of the envelopes of synthetic seismograms generated with moment-tensor **Mo** that represents a starting model for the inversion. Expanding the displacement **U** in a Taylor series about **Uo** to the first order gives

$$\boldsymbol{U} \simeq \boldsymbol{Uo} + \frac{\partial \boldsymbol{Uo}}{\partial m}\delta m \qquad (17)$$

which can also be written as

$$\boldsymbol{\delta U} = \boldsymbol{U} - \boldsymbol{Uo} = \frac{\partial \boldsymbol{Uo}}{\partial m}\delta m \qquad (18)$$

By perturbing moment-tensor components, we can numerically calculate the derivative matrix as

$$\boldsymbol{\delta G} = \frac{\boldsymbol{Uo}|mo - \boldsymbol{Uo}|mo+\delta m}{\delta m} \simeq \frac{\partial \boldsymbol{Uo}}{\partial m} \qquad (19)$$

From Equations (18) and (19), it follows that:

$$\boldsymbol{\delta U} = \boldsymbol{\delta G \delta M} \qquad (20)$$

Multiplying Equation (20) by $\delta \boldsymbol{G}^T$ from left,

$$\boldsymbol{\delta G^T \delta U} = [\boldsymbol{\delta G^T \delta} \mathbf{G}]\boldsymbol{\delta M}$$

δ**M** can be obtained through the least square inversion of δG as:

$$[\boldsymbol{\delta G^T \delta G}]^{-1} \boldsymbol{\delta} G^T \boldsymbol{\delta U} = \boldsymbol{\delta M}$$

The moment-tensor after one inversion step is

$$\mathbf{M1} = \mathbf{Mo} + \boldsymbol{\delta}\mathbf{M}$$

The next iteration is started with **M1** which yields **M2** = **M1** + $\boldsymbol{\delta}$**M1** and so on for the subsequent iterations until a final one, which is usually decided on when the difference in the fit of the data between the subsequent iterations becomes smaller than a threshold value decided by the user. The moment-tensor **Mn** obtained after the nth iteration is then decomposed to get the fault orientation (dip, strike and slip angles) as well as the scalar seismic moment. The scalar seismic moment thus obtained can be converted to the earthquake magnitude.

Chapter 3

Methodology and Data

- A significant portion of this chapter is published in: *Dahal and Ebel (2019)*. Method for Determination of Depths and moment Magnitudes of Small-Magnitude Local and Regional Earthquakes Recorded by a Sparse Seismic Network, *Bull. Seism. Soc. Am.*, **109**, 124–137, doi: 10.1785/0120180151.

3.1 INTRODUCTION

Various methods that are used to determine the source parameters of local and regional earthquakes are described in Section 1.2 of Chapter 1.Most of the methods developed to determine the source parameters of earthquakes smaller than M_w 3.5, have used earthquake data filtered through frequency passbands which includes the surface waves as well as body waves (*Tan and Helmberger 2007; Guilhem et al., 2014; D'Amico et al., 2011; D'Amico, 2014*). These methods tend to work for the given data set, particularly with a given source-receiver configuration, and are very difficult to be transferred to a new data set with a different source-receiver configuration. This dissertation has developed a new method to calculate the source parameters of small earthquakes which are recorded by a sparse network of local and regional seismic stations. The method is applicable to the earthquakes as small as M_w 2.5 and is usable to a wide range of source-receiver configurations. This chapter describes the method developed in this dissertation to constrain the source parameters of small earthquakes and introduces the aftershock sequences of the two earthquakes on which the method is tested and the aftershock sequence of an earthquake on which the method is applied after being fully developed.

3.2 SNR AND ENVELOPE OF A SEISMIC WAVEFORM

The ratio of the highest amplitude (sum of positive and negative amplitude) present in a signal to the highest amplitude present in its background noise is defined as SNR (signal-to-noise ratio) for the seismic signals analyzed in this dissertation. SNR decreases with the magnitude of an earthquake when filtered through any frequency band, but especially when filtered through the frequency band of 0.05-0.10 Hz (Table 3.1). In the frequency band of 0.05-0.1 Hz, the earthquake signal dominates the background noise for an M_w 4.3 event (SNR=20), whereas the earthquake signal is less dominant over the noise for an M_w 3.3 event (SNR=2) and is barely visible for the M_w 3.1 event (SNR=1). This indicates how much the SNR for this particular frequency band decreases with decreasing event magnitude below M_w 4.0. Table 3.1 contains one example that represents the general pattern of how SNR varies with event magnitude. This is the major reason why source moment-tensor inversions using regional seismic network data are commonly computed only for events with magnitude M > 4.0 when the passband of 0.05-0.10 Hz is used (*Dreger and Helmberger, 1990; Ford et al., 2009; Guilhem et al., 2014*).

Table 3.1 Signal-to-Noise Ratio (SNR) for different magnitude events filtered through a passband of 0.05-0.1 Hz.

M_w	SNR for Unfiltered	SNR for 0.05-0.1 Hz
4.3	120	20±2
3.3	27	2
3.1	18	1

Uncertainty in SNR for 0.05-0.1 Hz for M_w 4.3 reported in Table 3.1 is the standard deviation in the observed SNRs (rounded off to their nearest integers) with the signal

filtered through three different frequency bands of 0.04-0.09 Hz, 0.05-0.1 Hz and 0.06-3.011 Hz. Similar uncertainties are assumed for the remaining SNRs reported in Table 3.1.

Determinations of the source parameters for events with magnitudes less than M_w 4.0 using regional seismic network data require a determination of the frequency band with a good SNR for those magnitudes. From Figure 3.1 it is clear that the SNR varies with the frequency band through which the signal is filtered, and a larger SNR is obtained for higher frequency passbands (Figure 3.1(a) through (j)). Green's functions from a simple 1-D flat earth model are unable to generate synthetic seismograms that fit very well with the observed seismograms filtered through higher frequency passbands above 0.10 Hz because the synthetic seismograms lack the complexity of the observed waveforms in the higher frequency band. In the newly developed method described in this dissertation, the waveform envelope is used as a smoothing filter because the envelope of a seismogram has a smoother shape than the seismogram itself and thus should be easier to fit with a synthetic envelope than by trying to fit the waveform itself. By using the envelope of a seismogram filtered with a passband above 0.10 Hz, one can simplify the number of peaks in the seismogram that needs to be fit by the synthetic seismogram (Figure 3.1(f)) while still maintaining the SNR obtained by frequency filtering the data.

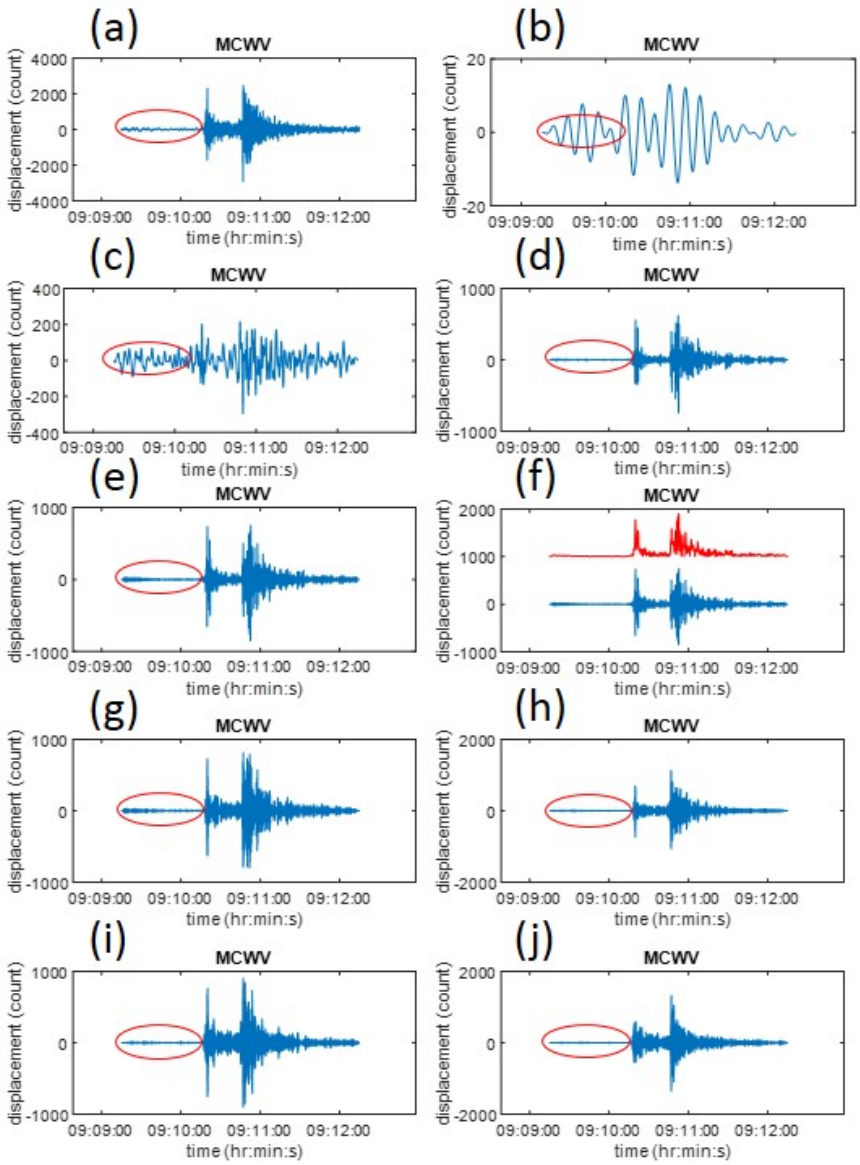

Figure 3.1. Vertical component seismogram of the M_w 3.3 Mineral Virginia aftershock with origin time 2011/09/01 09:09:37.60 UTC as measured by broadband station MCWV filtered through different frequency bands. The oval shows the section of the background noise for which the average noise amplitude was measured. (a) The unfiltered seismogram. The approximate SNR is 27. (b) Figure (a) filtered with a Butterworth band-

pass filter of passband 0.05-0.1 Hz. The approximate SNR is 2. (c) Figure (a) filtered with a Butterworth band-pass filter of passband 0.05-1 Hz. The approximate SNR is 3. (d) Figure (a) filtered with a Butterworth band-pass filter of passband 0.5-2 Hz. The approximate SNR is 86. (e) Figure (a) filtered with a Butterworth band-pass filter of passband 1-3 Hz. The approximate SNR is 70. (f) Lower is Figure (e). Upper is envelope of Figure (e). (g) Figure (a) filtered with a Butterworth band-pass filter of passband 2-4 Hz. The approximate SNR is 22. (h) Figure (a) filtered with a Butterworth band-pass filter of passband 3-5 Hz. The approximate SNR is 51. (i) Figure (a) filtered with a Butterworth band-pass filter of passband 4-6 Hz. The approximate SNR is 50. (j) Figure (a) filtered with a Butterworth band-pass filter of passband 5-8 Hz. The approximate SNR is 90.

3.3 METHODOLOGY

The waveform-envelope fitting method described in this chapter to determine the focal depths and moment magnitudes of earthquakes in the magnitude range of M_w 4.0 to M_w 2.5 recorded at local and regional distances is carried out in three steps. The first step is to determine all of the necessary parameters to be used in the analysis as well as to generate Green's functions to be used in the calculation of the synthetic seismograms. The second step is to read the observed seismograms and to process them to the observed envelopes as well as to read the Green's functions, compute synthetic seismograms using the Green's functions and process the synthetic seismograms to synthetic envelopes. The third and last step is to determine the optimal solution by finding the source parameters that give the best fit of the synthetic envelopes to the observed envelopes. A grid search is performed over all possible dip, rake and strike angles and as well as across the range of possible depths and scalar moments to find the optimal value of the focal depth and the optimal value of the scalar moment. To find the optimal focal mechanism, a non-linear moment-tensor inversion is performed in addition to the grid search over the possible dip, rake and strike angles for a known value of focal depth and a known value of scalar moment. The new method developed in this chapter is presented in Figure 3.2 and in detail as follows:

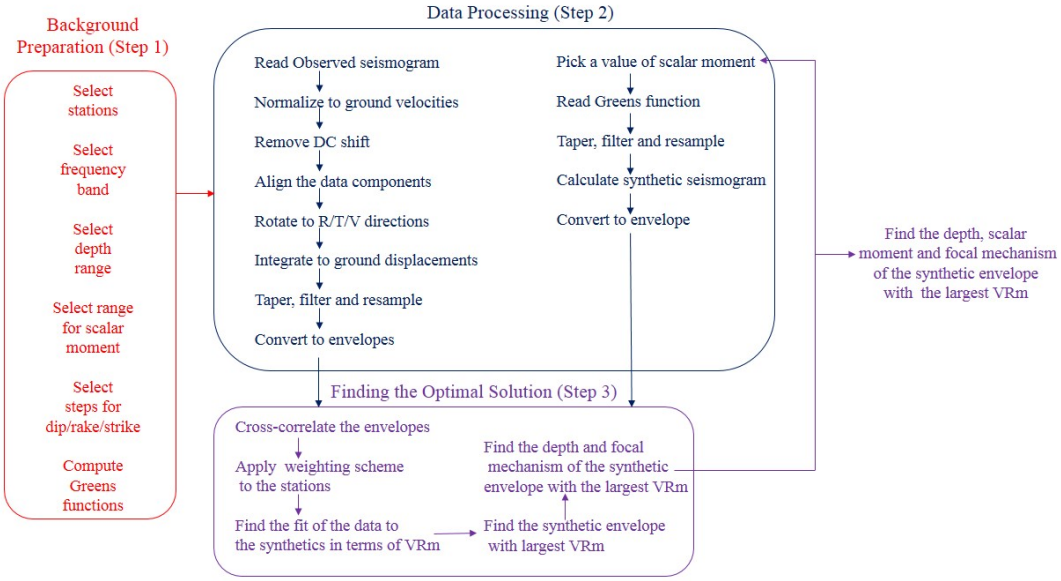

Figure 3.2 Flow chart showing the steps taken to determine the hypocentral depth and moment magnitude using the method described in this chapter. R/T/V refers to radial/tangential/vertical seismogram components and VRm refers to the modified variance reduction.

1) Background Preparation: The first step is to select a set of seismic stations, a frequency pass band, a range of seismic moments, a range of source focal depths and the steps in dip/rake/strike angles to be used in the grid search. In addition, a set of Green's functions is generated for the desired range of source depths and epicentral distances. Stations with SNR higher than a threshold SNR for a given frequency passband are chosen for the analysis. A threshold SNR can be set at different epicentral distances for different magnitude events and different passband frequencies in order to select those seismograms that should give the most robust solution from the analysis. Weights are applied to the stations used in the analysis such that the farther stations are weighted more (see Equation (21) in the last part of this section). Because the envelopes of the full waveforms are being used in the analysis, the higher amplitudes in the waveforms are controlled mostly by the surface waves, and the surface wave amplitudes become more dominant in the waveforms with distance. A range of seismic moments is chosen based on the magnitude of the event whereas the range of focal depths is selected based on prior knowledge about the known or suspected depth range of earthquakes in the study area.

2) Data Processing: In the second step, the regional waveforms are read/downloaded from where they are stored (e.g., IRIS DMC), the amplitudes of the seismograms are normalized to ground velocity by dividing the waveforms by the station gain, any DC amplitude shift present in the data is removed by subtracting the mean of

the waveform amplitudes from the waveform, and all three data components are aligned at the same starting time which is chosen to be the latest of the start times of the individual components. The waveforms are rotated to the radial, tangential and the vertical directions with the positive directions as vertical up, radially outward from the source for the SV wave and tangentially clockwise around the source for the SH wave. This receiver coordinate system is the Helmberger coordinate system (*Langston, 1981*) but with the positive vertical direction reversed. After the waveforms have been rotated, the velocity components are integrated to ground displacements, tapered at the beginning and at the end to prevent a step response from filtering, forward and reverse bandpass filtered to avoid any phase shifts from filtering, resampled to the sampling frequency to which the Green's functions are calculated and finally converted to their envelopes using the Hilbert transform. The Green's functions are generated in the Helmberger coordinate system, the vertical components are reversed to bring them to the receiver coordinate system, and then they are filtered exactly in the same manner as the observed waveforms and are converted to synthetic seismograms by convolving them with the moment-tensor components before the synthetics are converted to their envelopes.

3) Finding the Optimal Solution: The observed envelopes for a seismic station and all possible synthetic envelopes (as determined in the grid search over the steps in dip, rake and strike angles) for a given depth and scalar seismic moment for that station are cross-correlated to find the optimal relative time shift, i.e., the time shift that

produces the highest value of the cross-correlation coefficients from among the three component seismograms for the station. The traces are then aligned at this optimal shift and the fit of the synthetic envelopes to the observed envelopes is calculated in terms of a modified variance reduction (VRm) as defined in Equation (21). Weights are applied to the stations used in the analysis such that the farther stations are weighted more. Because the envelopes of the full waveforms are being used in the analysis, the higher amplitudes in the waveforms are controlled mostly by the surface waves, and the surface-wave amplitudes become more dominant in the waveforms with distance. The synthetic envelope with the largest VRm value for that depth and that seismic moment from among all of the stations is found. The process is repeated for a desired range of depths and a desired range of seismic moments until the optimal value of the depth and the optimal value of the seismic moment for the event are found. The modified variance reduction is defined as

$$VRm = [1 - \frac{(\sum_i w_i \sum_j (d_{ij} - sij)^2)}{\sum_i w_i \sum_j [(d_{ij})^2 + (s_{ij})^2]}] \times 100\% \qquad (21)$$

where the subscripts *i* refers to the station number and the subscript. *j* refers to one of the three data components. *d* is the observed seismogram. *s* is the synthetic seismogram. *w* is the weight given to each station so that the farther stations are weighted more.

3.4 APPLICATION OF THE METHOD TO SOME EARTHQUAKES

3.4.1 AFTERSHOCKS OF THE 2011 MINERAL, VIRGINIA, EARTHQUAKE

The M_w 5.7 Mineral Virginia earthquake that occurred on 23 August 2011 with origin time 17:51:3.9 UTC (yellow star in Figure 3.3) produced a well-recorded aftershock sequence (red and green shapes in Figure 3.3) due to the immediate deployment of temporary seismic stations after this intraplate mainshock. This aftershock data set provided an opportunity to apply the technique developed in this dissertation to determine the source parameters of small earthquakes using the data from regional seismic network stations and to compare the moment magnitudes, focal depths and focal mechanisms obtained with the analysis method of this dissertation to the moment magnitudes, focal depths and focal mechanisms obtained by other investigators using data from the portable seismic stations that were deployed over the mainshock epicenter. The new method of this dissertation is tested on 18 aftershocks of M_w between 3.62 and 2.63.

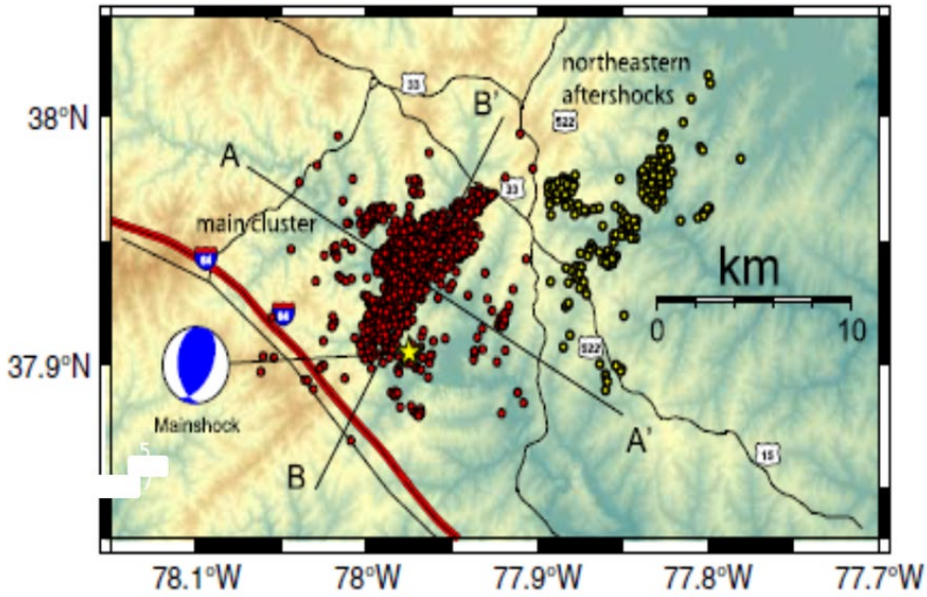

Figure 3.3. The 2011 Mineral earthquake and its aftershocks. [*Figure: Wu et al., 2015*]

3.4.2 AFTERSHOCKS OF THE 2013 LADYSMITH, QUEBEC, EARTHQUAKE

The M_w 4.3 Ladysmith Quebec earthquake that occurred on 17 May 2013 with origin time 13:43:23 UTC (star with 2013 in Figure 3.4) in the western Quebec seismic zone (WQSZ) had an aftershock sequence that was well recorded due to the presence of a dense distribution of Canadian National Seismograph Network (CNSN) and U.S. Transportable Array (TA) stations in the region. The aftershock sequence of the Ladysmith, Quebec earthquake gave a chance to test the method described in this thesis on events with relatively deeper focal depths of 10-15 km. The method is tested on 5 aftershocks of M_w between 3.62 and 2.63 of the 2013 Ladysmith, Quebec M_w 4.5 mainshock. Investigated is done on the effect of variations in the crustal structure on the determination of the moment magnitudes, focal depths and focal mechanisms using those aftershocks.

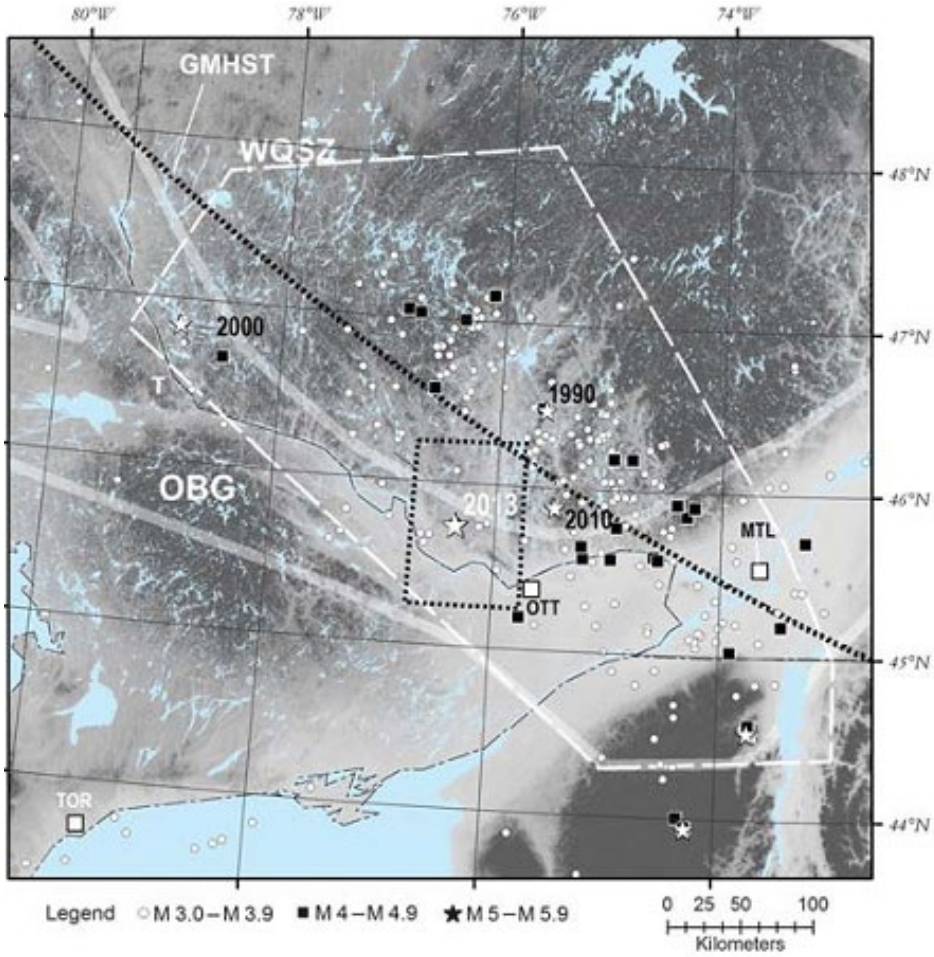

Figure 3.4 The 2013 Ladysmith earthquake within the outline of Western Quebec Seismic Zone (WQSZ). [*Figure: Bent et al., 2015*]

3.4.3 AFTERSHOCKS OF THE 2015 GORKHA, NEPAL, EARTHQUAKE

The M_w 7.8 Gorkha earthquake that occurred on 25 April 2015 with origin time 06:11:25 UTC (blue star with dark bold outline in Figure 3.5) produced a well-recorded aftershock sequence due to the immediate deployment of temporary seismic stations after the mainshock. This aftershock sequence gave a chance to apply the method developed in this dissertation to the earthquakes of a continental subduction zone that is tectonically different from the setting of the other two aftershock sequences studied in this dissertation, which were both located within a stable continental area.

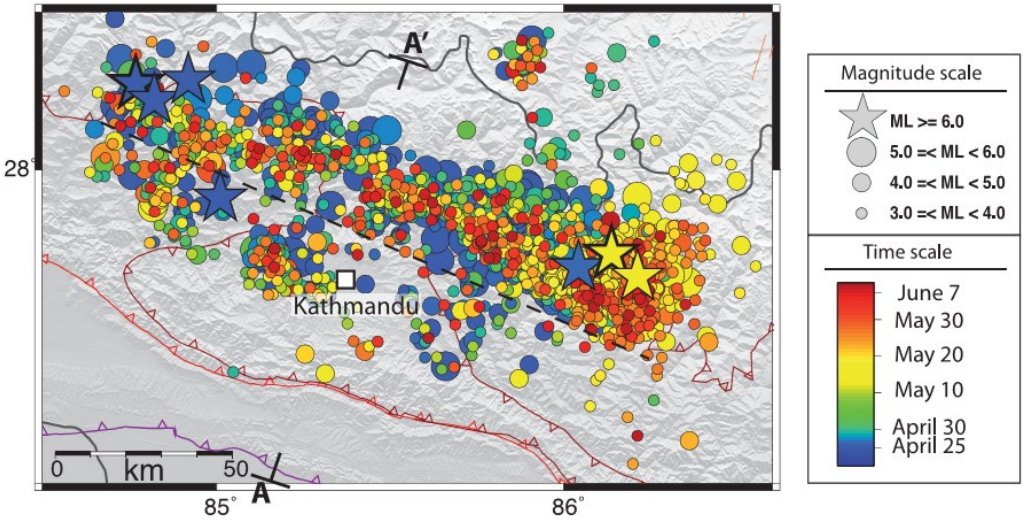

Figure 3.5. The 2015 Gorkha earthquake and the aftershocks color coded with their time of occurrence [Figure: *Adhikari et al., 2015*].

Chapter 4

DETERMINATION OF FOCAL DEPTHS AND MOMENT MAGNITUDES OF EARTHQUAKES BELOW M_w 4.0

- A significant portion of this chapter is published in: *Dahal and Ebel (2019)*. Method for Determination of Depths and Moment Magnitudes of Small-Magnitude Local and Regional Earthquakes Recorded by a Sparse Seismic Network, *Bull. Seism. Soc. Am.*, **109**, 124–137, doi: 10.1785/0120180151.

4.1 INTRODUCTION

As described in Chapter 1, the precise determination of the focal depth and moment magnitude of an earthquake is important for a good understanding of the earthquake source physics, the tectonic processes that caused the earthquake and the assessment of seismic hazard. The precise determination of the focal depth of an individual earthquake as part of routine regional seismic network monitoring depends on the several factors, such as the density of the local seismic stations, the accuracy of the crustal structure used to locate the earthquake and the ability of a seismic analyst to pick the P and S arrival times (*Pavlis, 1986; Gomberg et al., 1990*). The focal depth often is not very well constrained due to the trade-off between the source depth and the earthquake origin time when locations using only P and S arrival times are computed and there is no seismic station close to the epicenters (*Billings et al., 1994*).

In this chapter, a new method is presented to determine the focal depths and moment magnitudes of earthquakes using regional broadband seismic data. By calculating sets of envelopes of synthetic seismograms for all possible focal mechanisms over a range of

possible focal depths and a range of possible scalar moments and comparing the synthetic envelopes with the envelopes of observed seismograms, the best matching synthetic envelopes to the observed envelopes is sought, from which an estimate of the event focal depth and scalar moment is made. The method proposed in this dissertation finds reliable focal depths and moment magnitudes when compared to the focal depths and moment magnitudes found previously for the same events. The method is described in detail, and its effectiveness is demonstrated by applying the method to some aftershocks of the M_w 5.7 Mineral Virginia earthquake and to some aftershocks of the M_w 4.5 Ladysmith, Quebec earthquake for which hypocentral depths were well constrained.

4.2 DATA

For each event and each station included in the analyses of this chapter, the event magnitude, event origin time, station epicentral distance, station azimuth, station network code and station name were obtained from the IRIS wilber3 system (*http://ds.iris.edu/wilber3/find_stations/10002986* , last accessed April 2018). Data sets for events with previously reported focal depths that are well constrained were used in order to test the accuracy of the method. The first data set analyzed included the aftershocks of M_w 5.7 2011 Mineral earthquake described in the previous chapter. The majority of the aftershocks of the Mineral earthquake form a tabular cluster with hypocentral depths 3-8 km, and they delineate the newly discovered Quail Fault zone (*Horton et al., 2015a*). *Wu et al. (2015)* located 3,960 aftershocks from 25 August 2011 through 31 December 2011 and obtained focal mechanisms and depth solutions for 393 of the aftershocks. 17

aftershocks from the *Wu et al. (2015)* catalogue with magnitude (M_D*) between 3.62 and 2.49 along with one aftershock from R. Herrmann's website (*http://www.eas.slu.edu/eqc/eqc_mt/MECH.NA/*, last accessed March 2018) with moment magnitude (M_w) 3.14 were selected and the technique described in this dissertation was tested on those aftershocks. The second data set analyzed included the aftershocks of M_w 4.3 2013 Ladysmith earthquake described in the previous chapter. 5 aftershocks of local magnitude (ML) between 3.7 and 2.3 of this earthquake were selected and the method was tested on those aftershocks. The 2011 Mineral mainshock along with its 18 aftershocks, the 2013 Ladysmith earthquake along with its 5 aftershocks, and the stations used to obtain the data for each of these events are shown in Figure 4.1. The 23 events that are analyzed in this dissertation are listed in Table 4.1.

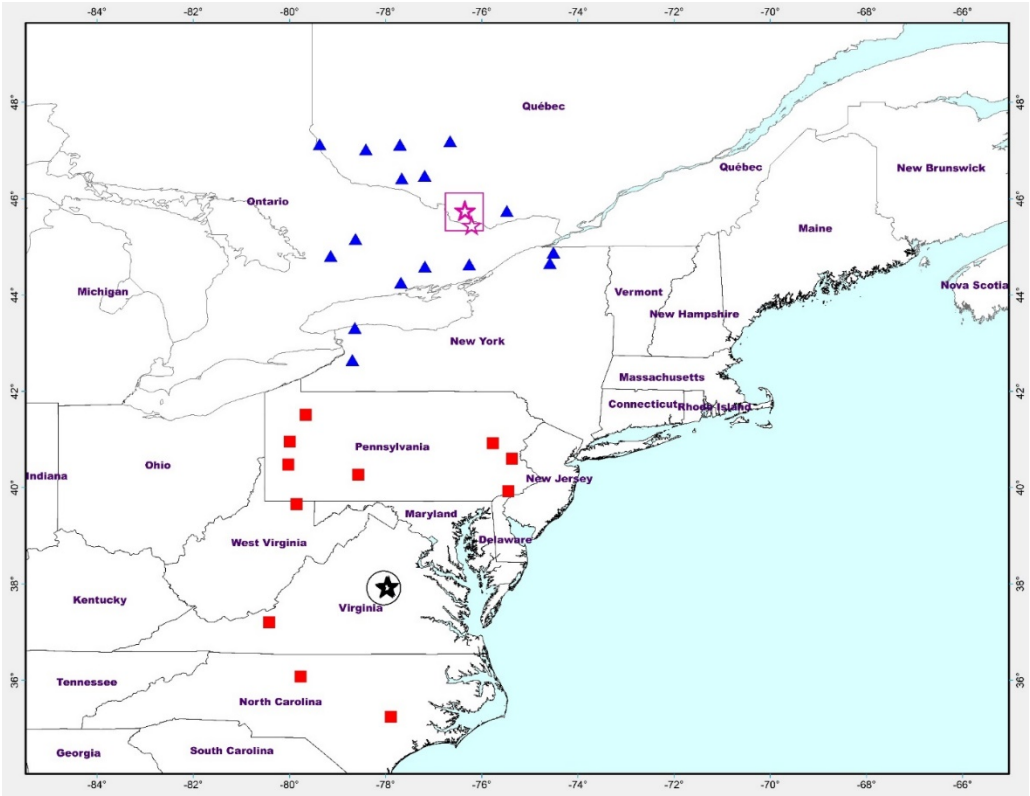

Figure 4.1. Map showing the M_w 5.7, 2011 Mineral, Virginia, earthquake epicenter (unfilled circle), epicenters of its 18 aftershocks analyzed in this study (stars on unfilled circle) along with the regional seismic stations used to analyze these earthquakes (filled squares) and M_w 4.5, 2013 Ladysmith, Quebec, earthquake epicenter (unfilled square), epicenters of its 5 aftershocks analyzed in this study (stars on unfilled square) and the regional seismic stations used to analyze these earthquakes (triangles).

Table 4.1: List of Mineral, Virginia aftershocks and Ladysmith, Quebec aftershocks analyzed

Aftershock Region	Event Number	Date (yyyy/mm /dd)	Time UTC (hh:mm:ss)	Duration Magnitude (M_D*)	Latitude (°N)	Longitude (°E)
Mineral, Virginia	1	2011/09/01	09:09:37	3.62	37.9453	-77.9450
	2	2011/08/25	05:07:51	3.49	37.9521	-77.9823
	3	2011/10/12	16:40:00	3.36	37.9423	-77.9850
	4	2011/08/30	03:48:28	3.27	37.9084	-77.9788
	5	2012/01/30	23:39:47	3.14†	37.9500	-77.9800
	6	2011/09/05	16:54:24	3.12	37.9481	-77.9669
	7	2011/08/29	03:16:51	3.07	37.9395	-77.9843
	8	2011/09/17	15:33:13	2.96	37.9267	-77.9860
	9	2011/08/25	23:40:56	2.92	37.9687	-77.9329
	10	2011/08/29	03:15:21	2.89	37.9397	-77.9839
	11	2011/08/25	15:27:46	2.83	37.9676	-77.9299
	12	2011/08/29	01:06:36	2.77	37.9395	-77.9840
	13	2011/10/19	00:02:44	2.76	37.9417	-77.9855
	14	2011/11/03	12:50:31	2.6	37.9497	-77.9624
	15	2011/08/27	09:02:29	2.6	37.9433	-77.9846
	16	2011/11/19	20:12:24	2.54	37.9456	-77.9866
	17	2011/10/05	06:18:49	2.51	37.9381	-77.9914
	18	2011/08/25	06:37:31	2.49	37.9475	-77.9857
Ladysmith, Quebec	19	2013/05/17	13:53:54	3.7^	45.7527	-76.3518
	20	2013/05/30	05:34:59	3.5^	45.7566	-76.3606
	21	2013/05/24	19:48:09	2.9^	45.7410	-76.346
	22	2013/05/17	20:15:17	2.6^	45.767	-76.3460
	23	2013/06/30	08:40:46	2.3^	45.4494	-76.2117

† refers to M_w, ^ refers to ML. The details for Mineral aftershocks presented in Table 4.1 are from *Wu et al. (2015)* and the details for Ladysmith aftershocks presented in Table 4.1 are read from IRIS wilber3 system (*http://ds.iris.edu/wilber3*).

4.3 METHODOLOGY

The methodology used in this chapter is described in detail in Section 3.2 of Chapter 3. Details of the methodology as applied to the 23 events that were analyzed for the determination of focal depths and moment magnitudes are presented in this section. Green's functions were generated at a grid of epicentral distances and source focal depths with epicentral distances ranging from 60-500 km at a step of 5 km and with depth at each epicentral distance ranging from 1 to 10 km for the Mineral aftershocks and ranging from 1 to 20 km for the Ladysmith aftershocks, both at a step of 1 km. Green's functions for the Mineral aftershocks were generated by utilizing the crustal model (1-D flat earth model) presented in Table 4.2. Green's functions for the Ladysmith aftershocks were generated by utilizing the crustal models (1-D flat earth models) presented in Table 4.3 (a), (b), (c). The crustal models in Table 4.2 and Table 4.3 (a) are published on Prof. R. Herrmann's website (*http://www.eas.slu.edu/eqc/eqc_mt/MECH.NA/*, last accessed March 2018). The crustal model in Table 4.3 (b) is taken from Table 8 of *Brune et al. (1963)* whereas the crustal model in Table 4.3 (c) is obtained by replacing the lower velocity layers below 25 km of the crustal model published in the last column of Table 1 in *Motazedian et al. (2013)* by relatively higher velocity lower crustal and upper mantle layers.

Table 4.2: Crustal model used to generate the Green's functions for the Mineral aftershocks

Thickness (km)	Vp (km/s)	Vs (km/s)	Rho (g/cc)	1/Qp	1/Qs
1	5	2.89	2.50	581	258

9	6.10	3.52	2.73	625	275
10	6.40	3.70	2.82	671	298
20	6.70	3.87	2.90	9000	5000
-	8.15	4.70	3.36	515	232

Errors in the parameters in Table 4.2 are not reported as they were not available in the source from which the crustal model was taken.

Table 4.3: Crustal models used to generate the Green's functions for the Ladysmith aftershocks.

(a)

Thickness (km)	Vp (km/s)	Vs (km/s)	Rho (g/cc)	1/Qp	1/Qs
1.9	3.41	2.01	2.22	331	147
6.1	5.55	3.30	2.61	287	128
13	6.27	3.74	2.78	472	210
19	6.41	3.77	2.82	901	411
-	7.90	4.62	3.28	6098	2703

(b)

Thickness (km)	Vp (km/s)	Vs (km/s)	Rho (g/cc)	1/Qp	1/Qs
6	5.64	3.47	2.70	331	147
10.5	6.15	3.64	2.80	472	147
18.7	6.60	3.85	2.85	901	411
-	8.10	4.72	3.30	6098	2703

The thickness of the third layer from the top (in bold) was increased by 5 km and 10 km to obtain alternative crustal structures with total crustal thicknesses of 40.2 km and 45.2 km, respectively, for use in the crustal structure sensitivity analyses.

(c)

Thickness (km)	Vp (km/s)	Vs (km/s)	Rho (g/cc)	1/Qp	1/Qs
2	5.89	3.40	2.26	300	150
2	5.91	3.41	2.27	300	150
2	5.92	3.42	2.29	300	150
2	5.92	3.42	2.28	300	150
2	6.17	3.56	2.37	500	200
2	6.17	3.56	2.37	500	200
2	6.20	3.58	2.48	500	200
2	6.24	3.60	2.50	500	200
1	6.27	3.62	2.51	500	200

2	6.41	3.70	2.65	500	200
2	6.41	3.70	2.65	500	200
2	6.39	3.69	2.65	900	400
1	6.32	3.65	2.62	900	400
6	6.58	3.80	2.73	900	400
6	6.76	3.90	2.80	900	400
4	7.10	4.10	2.94	900	400
-	7.97	4.60	3.30	6000	2700

5 km was added to and subtracted from the thickness of the third layer from the bottom (in bold) to obtain alternative crustal structures with total crustal thicknesses of 45 km and 35 km, respectively, for use in the crustal structure sensitivity analyses. Errors in the parameters in Table 4.3 (a), (b) and (c) are not reported as they were not available in the source from where the crustal models are taken.

An estimated value of the scalar seismic moment computed from the reported magnitude of the event was picked as the starting estimated seismic moment for the grid search. The seismic moment value estimated for the events analyzed are listed in Table 4.4. In the grid search, the value of the starting seismic moment was changed by adding/subtracting $1*10^{13}$ N-m cumulatively to/from the estimated value of $x*10^{13}$ N-m and $1*10^{14}$ N-m cumulatively to/from the estimated value of $x*10^{14}$ to search for the optimal value of the seismic moment with x ranging from 1 to 9. The number of stations used to analyze each event ranged from 3 to 10. The epicentral distances of the stations used in the analyses

ranged from 68-424 km. Observed data with SNR of 5-2480 were used in the analyses. Both the observed seismograms as well as the Green's functions were filtered forward and backward through a Butterworth bandpass filter with 2 poles with a passband frequency of 1-3 Hz.

The moment magnitude was computed using the value of the optimal scalar seismic moment obtained for each event. Some sample fits of the synthetic envelopes to the observed envelopes are shown in Figure 4.2. Sample goodness-of-fit curves with depth and with seismic moment are given in Figure 4.3.

Table 4.4: Details of the observed data and the estimated seismic moment used to generate the Green's function for the events analyzed.

Event Number from Table 4.1	Number of stations used	Epicentral distance range (km)	SNR range	Estimated Seismic Moment (Nm)
1	9	235-423	23±1-180±3	2×10^{14}
2	8	227-333	517-2480	1×10^{14}
3	7	229-424	9±1-57±2	9×10^{13}
4	6	229-381	8-51	8×10^{13}
5	4	231-306	82-177	7×10^{13}
6	7	231-423	6-35	7×10^{13}

7	7	229-378	5-29	6×10^{13}
8	4	251-279	5-22	5×10^{13}
9	6	242-388	5-22	5×10^{13}
10	4	229-317	6-16	4×10^{13}
11	3	255-306	5-19	4×10^{13}
12	4	229-265	5-6	3×10^{13}
13	3	232-264	11-24	3×10^{13}
14	3	231-264	5-6	2×10^{13}
15	4	229-421	5-8	2×10^{13}
16	3	232-265	5-13	1×10^{13}
17	4	229-318	6-7	1×10^{13}
18	5	230-320	5-17	1×10^{13}
19	4	119-200	8-88	1×10^{13}
20	8	122-290	23-323	1×10^{13}
21	7	68-190	6-42	1×10^{13}
22	5	122-202	8-52	1×10^{13}
23	10	100-209	6-96	1×10^{13}

Uncertainties in SNR reported for Events 1 and 3 in Table 4.4 are the standard deviations in the observed SNR (rounded off to their nearest integers) with the signal filtered through three different frequency bands of 0.99-2.99 Hz, 1.00-3.00 Hz and 1.01-3.01 Hz. It is assumed that similar uncertainties are present in the rest of the SNRs reported in Table 4.4.

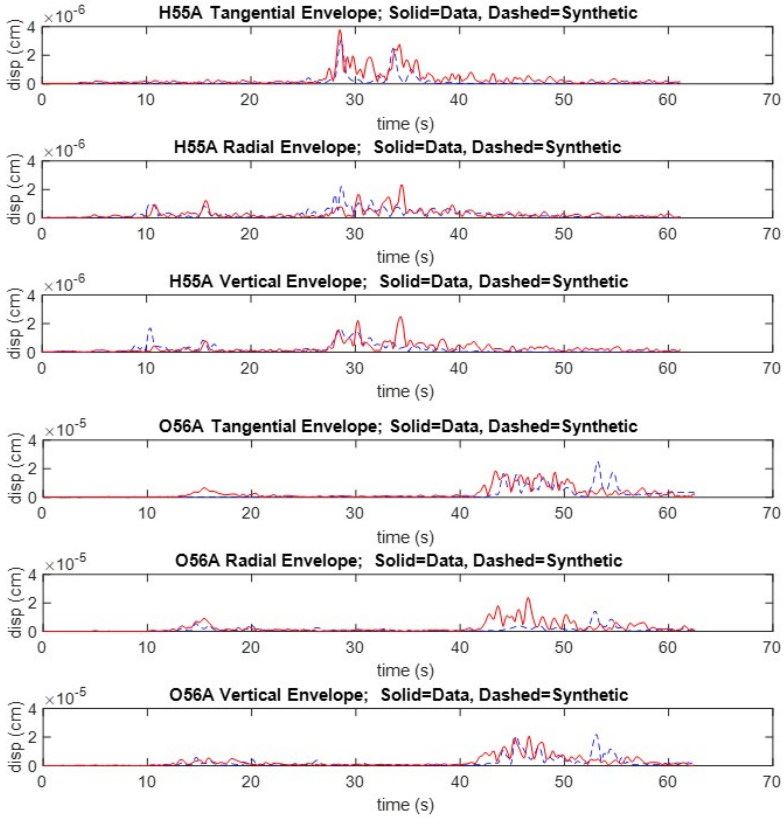

Figure 4.2. Fit of the synthetic envelopes to the data envelopes for a Ladysmith aftershock, Event 23 in Table 4.1 (upper graph) and for a Mineral aftershock, Event 3 in Table 4.1 (lower graph). Synthetic envelopes are generated for the optimal solution of dip= 50°, rake=140°, strike=220°, scalar moment=$1*10^{20}$ dyn-cm and depth=13 km for the Ladysmith aftershock and the optimal solution of dip=40°, rake=80°, strike=20°, scalar moment= $1.10*10^{21}$ dyn-cm and depth=4 km for the Mineral aftershock.

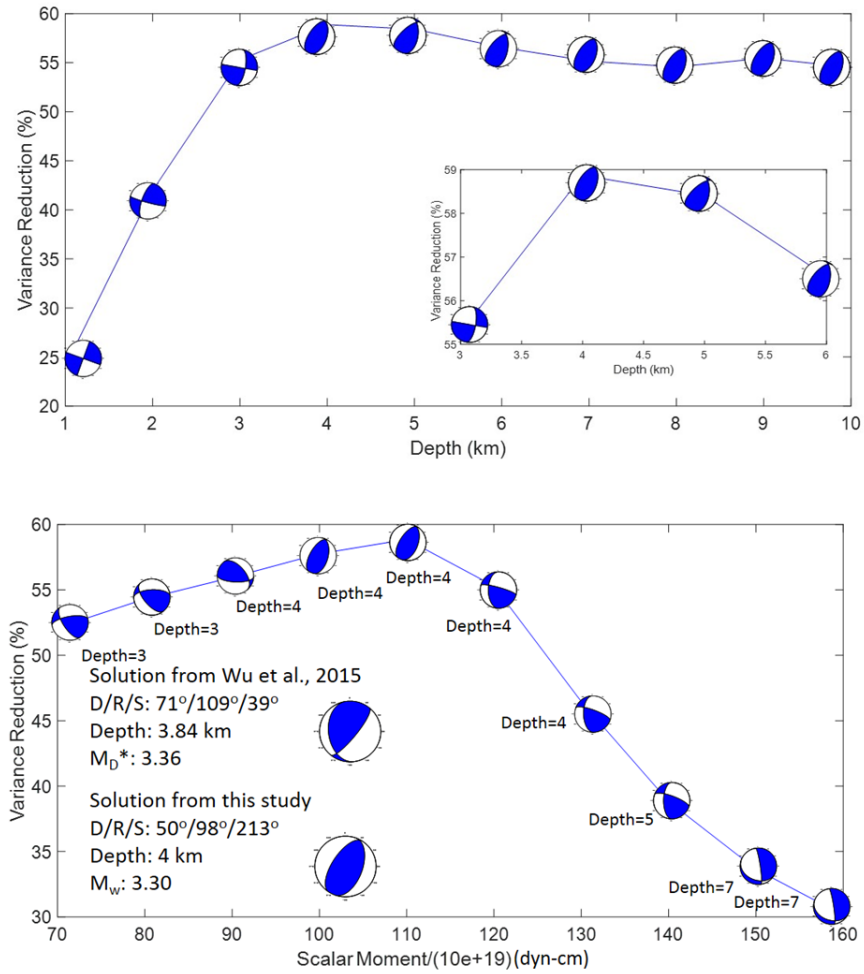

Figure 4.3. Goodness-of-fit curve with depth (upper graph) and with scalar moment (lower graph) for the Mineral aftershock Event 3 in Table 4.1. The inset in upper graph is obtained by limiting the x-axis in the upper graph from 3 km to 6 km so that the peak in the curve can be observed clearly. The optimal depth is at 4 km and the optimal scalar moment is at $1.60*10^{21}$ dyn-cm. A comparison of the solution obtained from this study and that from *Wu et al. (2015)* is given in the lower graph. The depth from this study is in close agreement with the depth from Wu et al. (2015) whereas the mechanism from this study is rotated as compared to the mechanism from *Wu et al. (2015)*.

4.4 DEPTH SIGNATURES IN SYNTHETIC WAVEFORMS

The reason that the method developed in this dissertation is capable of accurately determining event focal depth for small earthquakes is because the focal depth is very sensitive to arrival time differences between different higher-amplitude phases in the seismograms. Figure 4.4 shows a set of three synthetic seismograms for source depths of 5 km, 10 km and 15 km at an epicentral distance of 200 km filtered in the 1 Hz to 3 Hz band. Also shown in Figure 4.4 are the envelopes of these seismograms. The three arrows on Figure 4.4 point to the three distinct phases on each seismogram. The earliest arrow in time points to the first P-arrival, which at 200 km epicentral distance is the head wave from the Moho interface. The arrow with a filled circle on the top points to the peak amplitude in the later, higher-amplitude P arrivals, which are comprised of the post critical reflections from the different layers in the crust as well as the surface reflections pP and sP and their corresponding deep crustal reflections. The arrow with the filled diamond at the top points to the first high amplitude in the later, highest amplitude part of the seismogram, which is a combined train of S and Lg waves. In Figure 4.4, systematic changes are seen in the relative time differences between the three arrows in the seismograms as well as in the envelopes as a function of depth. The common feature in these seismograms is that the energy is concentrated basically in two regions of the seismograms, firstly in the time window where the pP, sP and post critical reflections arrive and secondly in the time window where the S and Lg wave train arrive in the seismogram. The time difference between the peak amplitude in the packet of energy composed of the pP, sP and post critical reflections and the first P-arrival shows a dependence on depth, with deeper events having

a greater time difference. Similarly, the time difference between the peak amplitude in the packet of energy composed of the pP, sP and post critical reflections and the first high amplitude in the S and Lg wave train is also dependent on the focal depth of the event, with shallower events having a greater time difference. The method of this dissertation is sensitive to these systematic timing differences in the envelope shapes due to the depth of the event, and it is for this reason that the method is able to constrain the depth of the each event analyzed.

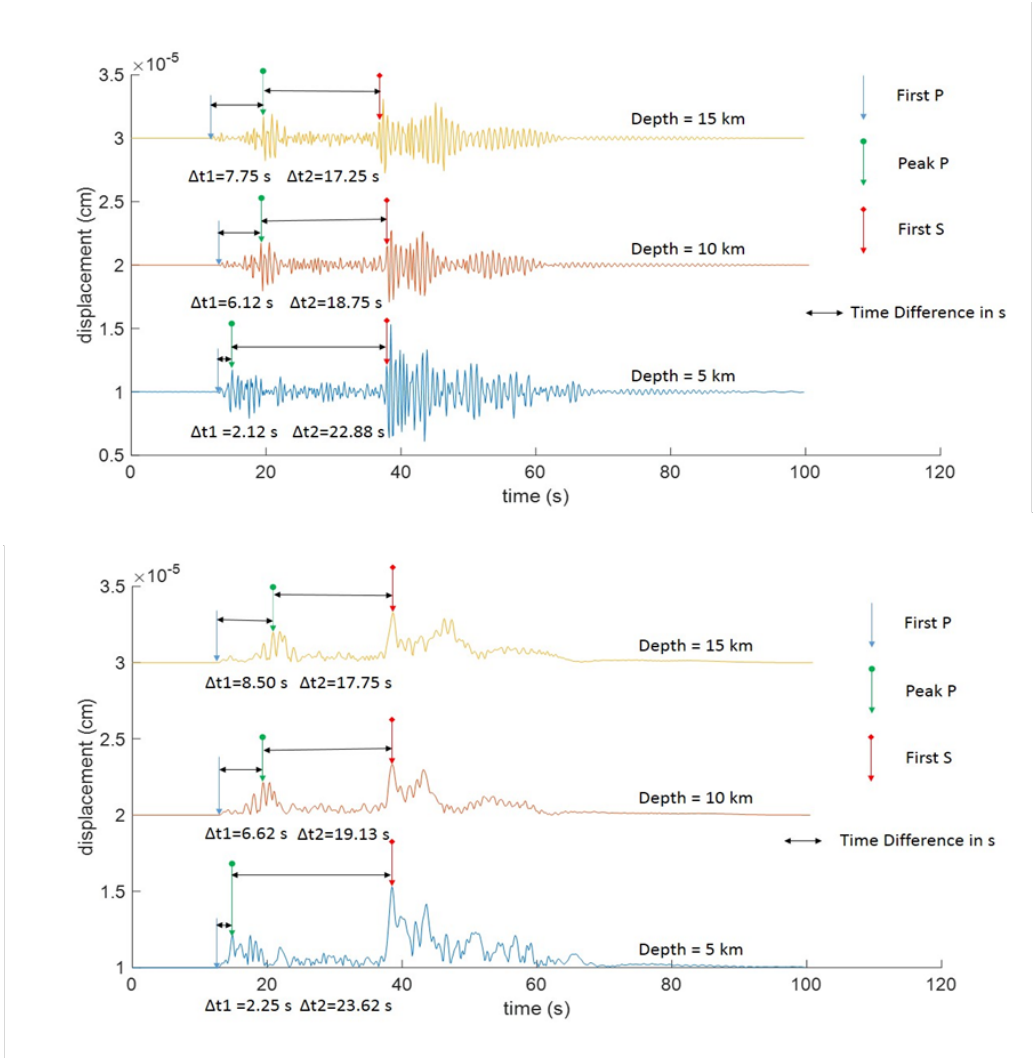

Figure 4.4 Synthetic seismograms (upper graph) and corresponding envelopes (lower graph) generated with dip=45°, rake=90°, strike=90°, azimuth=50° at an epicentral distance of 200 km for different depth sources.

4.5 RESULTS AND ANALYSIS

4.5.1 FOCAL DEPTHS AND MOMENT MAGNITUDES

Focal depths and moment magnitudes obtained for the events analyzed using the crustal structures in Table 4.2 and Table 4.3 (a) from the method developed in this thesis are presented in Table 4.5.

Table 4.5. Depths and moment magnitudes of the Mineral and Ladysmith aftershocks using the method developed in this dissertation applied to data from all available stations.

Event Number from Table 4.1	Depth from previous studies (km)	Depth from this study (km)	Percentage Change in Depth* (%)	Duration Mag. (M_D*) from previous study	Moment Magnitude (M_w) from previous study	Moment Magnitude (M_w) from this study
1	6.77	4±1.09	41	3.62	3.30	3.62±0.13
2	2.83	4	-41	3.49	3.94	3.70
3	3.84	4±1.47	-4	3.36	-	3.30±0.14
4	6.80	3±1.23	56	3.27	2.68	3.10±0.07
5	3.00	4	-33	-	3.14	3.50
6	5.38	4	26	3.12	-	2.95
7	4.34	4	8	3.07	-	3.27
8	4.07	4	2	2.96	-	3.04
9	5.68	4	30	2.92	2.56	3.10
10	4.31	5	-16	2.89	-	2.83
11	5.75	4	30	2.83	-	3.04
12	4.38	4	9	2.77	-	2.63
13	3.78	4	-6	2.76	-	2.95
14	5.54	3	46	2.6	-	2.63
15	3.46	7	-102	2.6	-	2.95
16	2.60	3	-15	2.54	-	2.63
17	3.60	3	17	2.51	-	2.60
18	2.33	4	-72	2.49	-	2.83
19	-, 14	10	-, 28.57	3.7^	-	3.62
20	11.24,13	10	11.03, 23.07	3.5^	-	3.04
21	11.68, 14.6	12±1.87	-2.74, 17.81	2.9^	-	2.83±0.09
22	-, 14	10	-, 28.57	2.6^	-	2.83
23	11.53,14	13±1.87	-12.75, 7.14	2.3^	-	2.63±0.12

^ refers to ML, - refers to data not available. For the Mineral Virginia aftershocks previous studies refers to *Wu et al. (2015)* (Modified duration magnitude (M_D*) is described in Chapter 2) and to Professor R. Herrmann's website (*http://www.eas.slu.edu/eqc/eqc_mt/MECH.NA/20120130233947/index.html*). For the Ladysmith aftershocks previous studies refers to *Bent et al. (2015)* and *Ghafoori, S. (2017)*. For Ladysmith aftershocks, there are two sets of depths reported in the third column. The first set of depths is obtained from RDPM *Bent et al. (2015)* and the second set of depths is obtained using routine hypocentral location of the events *Bent et al. (2015)*. The error in depths and moment magnitudes for Events 1, 3, 4, 21 and 23 in Table 4.5 are estimated from the single station analysis presented in Table 4.7. It is assumed that similar errors are present in the focal depths and moment magnitudes for the rest of the events. The error in depths and moment magnitudes from previous studies are not reported as they were not available in those studies. The percentage difference in depths reported in Table 4.5 are obtained by rounding off the percentage (to the nearest integer) calculated using the equation below:

$$\left[\frac{Depth\ from\ previous\ study - Depth\ from\ this\ study}{Depth\ from\ Previous\ Study}\right] \times 100\%$$

Focal depths using all available stations ranged from 3-7 km with a standard deviation of 1.75 km for the Mineral aftershocks and 10-13 km with a standard deviation of 1.13 km for the Ladysmith aftershocks (as compared to the solutions obtained using RDPM, *Bent et al. (2015)*). The depths of all he Mineral aftershocks from the previous study (*Wu et al., 2015*) were obtained from the first arrival time data as recorded by the portable stations deployed after the mainshock except for one event (Event Number 5 in Table 4.1) for which the depth was obtained from a regional moment-tensor inversion

(*http://www.eas.slu.edu/eqc/eqc_mt/MECH.NA/20120130233947/index.html*). The distribution of the depths of these aftershocks within 3-7 km as obtained in Table 4.5 is supported by *Horton et al. (2015b)*, who concluded that most of the aftershocks of Mineral earthquake are concentrated at focal depths of 4-6 km. The depths from the previous studies of Ladysmith aftershock with Event Numbers 20, 21 and 23 in Table 4.1 as obtained with the Regional Depth Phase Modeling (RDPM) technique using the data from stations within 16 km of the epicenters ranged from 11.2-11.7 km (*Bent et al., 2015*). The depths of the aftershocks from Event Number 19 to Event Number 23 as obtained from the routine hypocentral calculations ranged from 13.0-14.6 km (*Bent et al., 2015*). For the Ladysmith events analyzed using the crustal structure in Table 4.3 (a), depths from this study agree more with the depths obtained using the RDPM than with the depths obtained from the routine hypocentral locations of the events.

The moment magnitudes obtained for the Mineral aftershocks ranged from M_w 2.60-3.70, whereas for Ladysmith aftershocks they ranged from M_w 2.63-3.62. Moment magnitudes for the Mineral mainshock and Ladysmith mainshock were also determined using the waveform envelope method introduced in this dissertation. As obtained from this study, the moment magnitude for Ladysmith mainshock differs by 0.04 magnitude unit whereas the moment magnitude obtained for the Mineral mainshock differs by 0.15 magnitude unit as compared to the moment magnitudes for these events published by R. Prof. Herrmann on his website (*http://www.eas.slu.edu/eqc/eqc_mt/MECH.NA*). Five of the Mineral, Virginia aftershocks analyzed have previously reported moment magnitudes which differ

from the moment magnitudes obtained from this study, with a range from 0.24 to 0.54 magnitude units (see Table 4.6).

Table 4.6. Observed difference in the magnitude of Mineral aftershocks between the inversion method used by Herrmann and the method of this dissertation.

Event number from Table 4.1	Number of regional stations used by R. Herrmann	Number of portable stations used by R. Herrmann	Magnitude (M_w) difference between R. Herrmann and this study
1	5	4	0.32
2	15	-	0.24
4	-	10	0.42
5	2	7	0.36
9	-	6	0.54

The observed differences in the moment magnitudes in Table 4.6 for the five Mineral aftershocks from this study and the previously published solutions follow a pattern of being larger with the smaller events. In the analyses by Prof. R. Herrmann, for the smaller Mineral aftershocks fewer regional stations were used in the moment-tensor inversion to obtain his moment magnitudes. He compensated for this lack of regional data for the smaller aftershocks by incorporating data in his inversions from the portable aftershock monitoring stations that were installed in the epicentral region shortly after the mainshock took place. In contrast, the newly developed analysis method utilized data only from regional stations. The largest difference in moment magnitude between the newly developed method and that of Prof. R. Herrmann was for Event Number 9 in Table 4.1, which is the smallest of the events for which Prof. R. Herrmann was able to obtain M_w

through his moment-tensor inversion. For this event, Prof. R. Herrmann used only data from the portable aftershock monitoring network, presumably because the SNRs at the regional seismic network stations were too low in the frequency band that he used in his analysis. The discrepancy in magnitudes between the new analyses from this study and those of Prof. Herrmann for the Mineral aftershocks appears to directly correlate with how few regional seismic network stations (and how many aftershock monitoring stations) that Prof. R. Herrmann included. As a confirmation of this, it is noted that the magnitude differences between this study and those of Prof. R. Herrmann and of the USGS for the Mineral mainshock and the Ladysmith mainshock are small (0.15 magnitude unit or less). For these two mainshocks, all the moment magnitudes computed in this study, by Prof. R. Herrmann and by the USGS only used data from regional seismic network stations.

In this study tests are carried out to determine the minimum number of the stations from which one can determine an accurate depth and moment magnitude of an event using the method in this dissertation, and it was found that the method can provide reliable focal depths and moment magnitudes using data from just a single station. Depths and moment magnitudes obtained by analyzing data from individual stations using the method for three of the Mineral aftershocks (Events 1, 3 and 4 in Table 4.1) and two of the Ladysmith aftershocks (Events 21 and 23 in Table 4.1) are presented in Table 4.7. On average of 4-5 stations were used in the full analysis described above (see Table 4.7) to find the depth and the scalar moment of each of these events. The single-station depths in Table 4.7 are in good agreement with the depths obtained from the previous studies (*Wu et al., 2015,*

http://www.eas.slu.edu/eqc/eqc_mt/MECH.NA/20120130233947/index.html; *Bent et al., 2015*) as well as with the depths obtained by the method of this dissertation using all available stations presented in Table 4.5. Also, the moment magnitudes obtained by using a single station show a good agreement with the moment magnitudes obtained by using all available stations. The standard deviation of 0.07-0.14 in the M_w values calculated using the method of this dissertation with the single stations is similar to the error in the estimation of M_w by the source inversion method described in *Duputel et al. (2012)*. This shows that the method of this dissertation is able to recover the focal depth as well as the scalar moment and hence the moment magnitude of small magnitude earthquakes even if there is a record of an event with good SNR from only one station. This makes the method extremely useful in regions of thinly scattered regional and local seismic stations, which is the case in many regions around the globe including some parts of the CEUS.

Table 4.7. Depths and moment magnitudes of the Mineral and Ladysmith aftershocks using the method of this dissertation applied to data from a single station.

Event number from Table 4.1	Station used	Depth from single station analysis (km)	Mean depth of single station analysis ± standard deviation (km)	Depth using all stations from Table 4.5 (km)	Scalar Moment (10^{13} N-m)	M_w	Mean M_w of single station analysis ± standard deviation	M_w using all stations from Table 4.5
1	BLA	5	5±1.09	4	60	3.82	3.72±0.13	3.62
	CNNC	4			70	3.86		
	MCWV	5			20	3.50		
	O56A	4			40	3.70		
	PSUB	7			40	3.70		

3	BLA	4	3.2±1.47	4	10	3.30	3.40±0.14	3.30
	MCWV	5			10	3.30		
	O56A	4			30	3.62		
	PANJ	2			9	3.27		
	M54A	1			20	3.50		
4	BLA	5	5±1.23	3	6	3.15	3.12±0.07	3.10
	MCWV	4			4	3.04		
	O56A	4			7	3.20		
	PSUB	7			4	3.04		
21	E53A	12	12±1.87	12	2	2.83	2.88±0.09	2.83
	G53A	10			4	3.04		
	GAC	15			2	2.83		
	D54A	11			2	2.83		
23	E53A	12	13.5±1.5	13	1	2.63	2.81±0.12	2.63
	H55A	15			2	2.83		
	I55A	15			2	2.83		
	LONY	12			3	2.95		

Tests were carried out to determine the minimum SNR for the observed seismograms that can be used to find a precise focal depth and moment magnitude of an event using the method of this dissertation. In Figure 4.5, it is assumed that a minimum SNR of 5 of an earthquake signal is required to constrain the focal depth using the method of this dissertation. Figure 4.5 indicates that one can get reliable values of focal depth and seismic moment using stations with epicentral distances as great as 510 km for an event of magnitude M_w 3.62 and as great as 283 km for an event of magnitude M_w 2.63 using the method of this dissertation. The SNR for the M_w 2.63 event was decreased to obtain an SNR for an M_w 2.13 so that the x-intercept difference between the curves for the M_w 2.63 and M_w 2.13 units (half magnitude unit difference) is half of the x-intercept difference between the M_w 3.62 and M_w 2.63 (one magnitude unit difference). The predicted threshold epicentral distance for an event of magnitude M_w 2.13 is 150 km, which indicates that one should be able to accurately determine depths and scalar moments of events as low as M_w

2.13 if there are one or more seismic stations within 150 km of the epicenter of the seismic source.

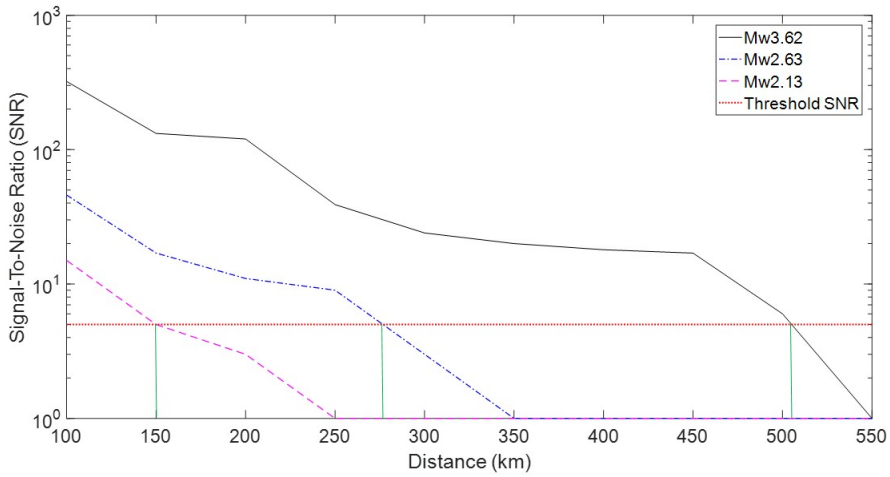

Figure 4.5. Observed decrease of SNR with epicentral distance for two of the Ladysmith aftershocks, one with M_w 3.62 (event 19 in Table 4.1) and one with M_w 2.63 (Event 23 in Table 4.1). The threshold SNR is 5. The threshold epicentral distance for an event of magnitude M_w 3.62 is 510 km whereas for an event of magnitude M_w 2.63 it is 283 km. The predicted threshold epicentral distance for an event of magnitude M_w 2.13 is estimated to be 150 km.

4.5.2 SENSITIVITY TO CRUSTAL STRUCTURES

The arrival times of different seismic phases depend on the crustal structure through which they travel. This means that the crustal structure used to generate the Green's functions must have some effect on the focal depths and moment magnitudes obtained using the method of this dissertation. To investigate how much effect the crustal structure may have on the results, two different crustal structures for the region were taken and used to generate Green's functions. To further test the sensitivity of the method to variations in crustal structure, the crustal thickness for each of the two crustal models was varied to values of 35 km, 40 km and 45 km. Using all of these different crustal models, focal depths and moment magnitudes for the Ladysmith aftershocks were computed using the method of this dissertation. One published crustal structure that was used in this sensitivity testing is presented in Table 4.3 (b). This crustal structure has a Moho depth of 35.2 km. To the bottom layer of this model were added 5 km and 10 km of additional material with the same seismic properties to obtain new crustal models with crustal thicknesses of 40.2 km and 45.2 km. The second published crustal structure tested is given in Table 4.3 (c). This crustal structure as published has a crustal thickness of 40 km, to which 5 km of crustal thickness was added and subtracted to obtain crustal structures with the crustal thicknesses of 45 km and 35 km.

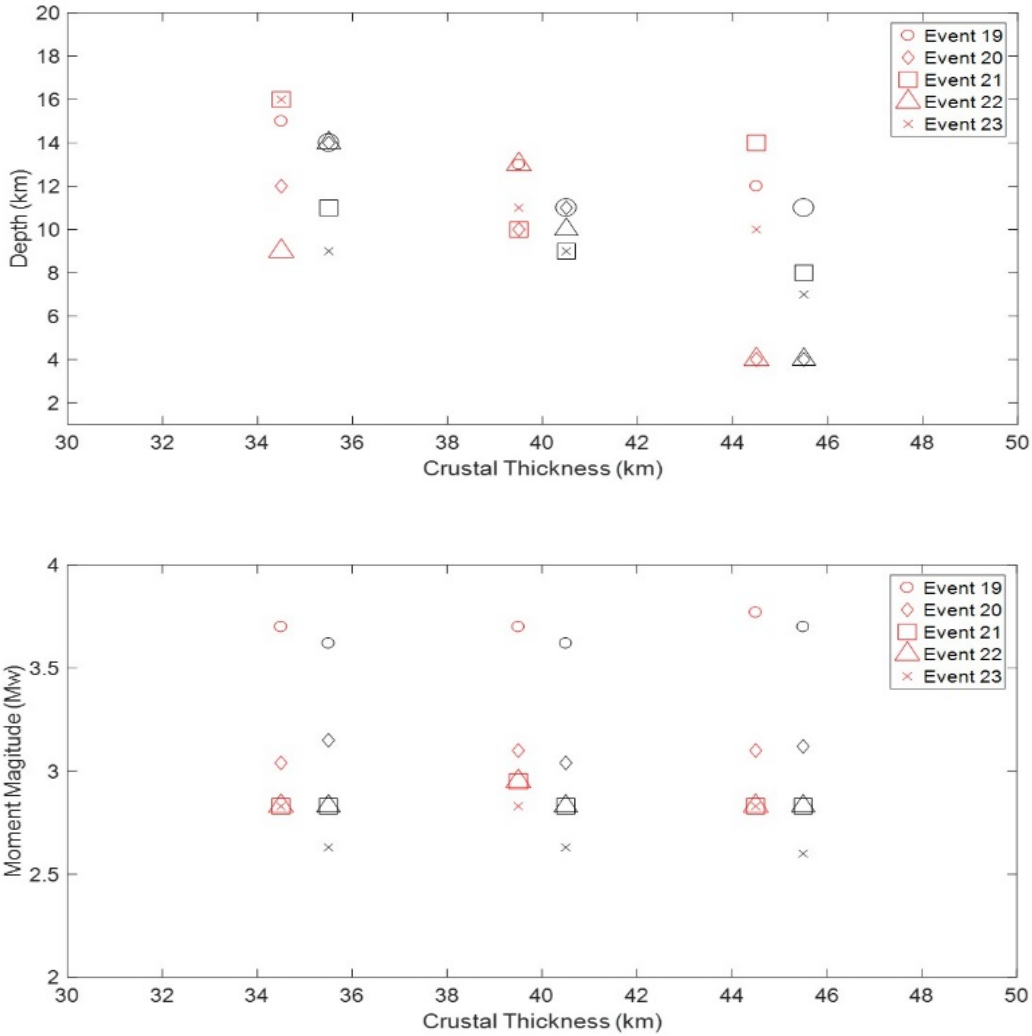

Figure 4.6. Variation of focal depths (upper graph) and variation of moment magnitudes (lower graph) of the Ladysmith aftershocks with variations in seismic structure and crustal thickness. Focal depths and moment magnitudes for crustal thicknesses of 35.2 km, 40.2 km and 45.2 km obtained using the crustal model given in Table 4.3 (b) are plotted at crustal thicknesses of 34.5 km, 39.5 km and 44.5 km, respectively. Focal depths and moment magnitudes for crustal thicknesses of 35 km, 40 km and 45 km obtained using the crustal model given in Table 4.3 (c) are plotted at crustal thicknesses of 35.5 km, 40.5 km and 45.5 km, respectively. Event numbers in the legend refer to Table 4.1.

The results obtained from the tests done on the two crustal structures each with the three different crustal thicknesses are summarized in Figure 4.6. For the crustal structure listed in Table 4.3 (b), the focal depths computed with the method of this dissertation for the Ladysmith aftershocks are between 9 km and 16 km with a mean depth of 13.6 km, between 10 km and 13 km with a mean depth of 11.4 km and between 4 km and 14 km with a mean depth of 8.8 km for the respective crustal thicknesses of 35.2 km, 40.2 km and 45.2 km. For the crustal structure listed in Table 4.3 (c), the focal depths computed with the method of this dissertation are between 9 km and14 km with a mean depth of 12.4 km, between 9 km and 11 km with a mean depth of 10 km and between 4 km and 11 km with a mean depth of 6.8 km for the respective crustal thicknesses of 35 km, 40 km and 45 km. From these results, it can be seen that the depths of the aftershocks are less dispersed and closer to the independently determined focal depths for the crustal thickness of 40 km as compared to the crustal thicknesses of 35 km and 45 km. The moment magnitudes of the Ladysmith aftershocks range from M_w 2.83 to 3.70 as determined using the crustal structure listed in Table 4.3 (b) whereas they range from M_w 2.60 to 3.70 as determined from the crustal structure listed in Table 4.3 (c). The moment magnitudes determined using three different crustal thicknesses for the crustal structure in Table 4.3 (b) show no difference except for event 20 in Table 4.1 for which M_w is less by 0.1 magnitude unit for the crustal thickness of 40 km as compared to the other two crustal thicknesses. Similarly, the moment magnitudes determined using the three different crustal thicknesses for the crustal structure in Table 4.3 (c) show no difference for Event 19 and Event 23 in Table 4.1. A slight change in moment magnitude is observed for the remaining events where the change is always less than 0.16 magnitude unit.

The sensitivity analysis shows the crustal structure dependence of the focal depths determined by the method developed in this dissertation. It is observed that the focal depths determined by the method of this dissertation are sensitive primarily to the crustal thickness with a much smaller dependence on the details of the crustal layers used to generate the Green's functions. These analyses show a tendency for the computed focal depths to be somewhat shallower for a thicker crust and somewhat deeper for a thinner crust with only small differences observed with variations in the crustal details. On the other hand, the determination of the moment magnitudes does not exhibit any observable dependence on crustal structure, and only small variations in the computed seismic moment using different models of the velocity layering above the Moho are seen.

4.6 CONCLUSIONS

In this chapter, a new method is developed and tested that can determine the focal depths and moment magnitudes of small earthquakes from magnitude M_w 3.70 down to at least M_w 2.60 by using data from the available local and regional seismic stations at epicentral distances of 68 km to 424 km. The method works by fitting synthetic waveform envelopes to the envelopes of observed seismograms. The focal depths of the Mineral Virginia aftershocks ranged from 3 to 7 km whereas the focal depths of the Ladysmith Quebec aftershocks ranged from 9 to 13 km as determined by the method of this dissertation by using crustal models each of thickness 40 km. These depths are similar to those that were found for these events using other methods for the depth determinations. The focal depths obtained using the method of this dissertation depend primarily on thickness of the crust

used to generate synthetic seismograms. The method is applied successfully to the range of crustal focal depths in two different geographical settings using four different velocity models. The moment magnitudes obtained for the Mineral aftershocks ranged from M_w 2.60 to M_w 3.70 whereas for Ladysmith aftershocks they ranged from M_w 2.63 to M_w 3.62 among all the crustal structures that were tested. The variation of moment magnitudes obtained using the different crustal thicknesses is 0.16 or less.

The focal depths and moment magnitudes computed using data from all available seismic stations were reproduced using data from just a single station, no matter which seismic station was tested. This shows the robustness of the method developed in this dissertation for determining the focal depths and seismic moments of small earthquakes using data from a sparse regional seismic network. The method of this dissertation works because the arrival time differences between the different higher amplitude phases in the seismograms, are sensitive to the focal depth of the event. These arrival time differences stand out well even in the seismograms from a single station, which enables the method to constrain depth of an event using data from a single station. Along with the focal depths, the method also obtains the scalar seismic moments for the smaller magnitude events from which moment magnitudes for these earthquakes can be calculated.

Chapter 5

DETERMINATION OF FOCAL MECHANISMS OF EARTHQUAKES BELOW M_w4.0

5.1 INTRODUCTION

Accurate determination of the focal mechanisms of earthquakes is required to understand the faulting process during earthquakes as well as for constraining the potential seismic source zones for future earthquakes. If the seismic network is spatially dense near an earthquake epicenter, P-wave first-motion data and S/P amplitude ratios can be used to calculate the focal mechanism for that earthquake. If the seismic network coverage is sparse around an earthquake epicenter, then the most accurate focal mechanisms are obtained through the moment-tensor inversion of local and regional waveform data. One of the moment-tensor inversion methods that is commonly used with regional seismic network data from a sparse network of stations is Dreger's moment-tensor inversion method, which uses waveforms filtered through a relatively low frequency passband that is typically of 0.05-0.1 Hz (*Dreger and Helmberger, 1990; Ford et al., 2009*). There are other versions of moment-tensor inversion methods that are routinely used for sparse regional data such as those employed by the Saint Louis University Earthquake Center (SLUC) and by the National Earthquake Information Center (NEIC) of the United States Geological Survey (USGS). Both of these regional waveform inversion methods process the seismic waveforms with a low-pass filter which only passes the fundamental-mode surface waves, excluding the body waves from being included in the inversion. The surface waves utilized in all of these inversion methods have good signal-to-noise ratio (SNR)

usually only for events with magnitude about M4.0 and higher, and it is for this reason that these moment-tensor inversion methods are able to obtain accurate focal mechanisms for earthquakes of magnitude above about M_w 4.0 (*Guilhem et al., 2014*). The focal mechanisms from these methods become progressively more inaccurate as the sizes of the events analyzed decrease below M_w 4.0, although in some cases these inversion methods can extract accurate source parameters of earthquakes smaller than M_w 4.0. For example, the catalog of regional moment-tensor inversion results for North America put together by the SLUC has 103 events with $M_w \geq 4.0$, 86 events with $4.0 > M_w \geq 3.5$ and 9 events with $M_w < 3.5$ of the total number of 198 events that were analyzed for the year 2018. (*http://www.eas.slu.edu/eqc/eqc_mt/MECH.NA/2014.html*). This shows how the number of events that can be analyzed using moment-tensor inversion method decreases for $M_w < 4.0$ using the method employed by the SLUC.

In addition to the limitations provide by SNR, imprecise velocity models available for local and regional earthquakes, the trade-off between the source depth and the earthquake origin time inherent in earthquake locations computed using P and S arrival times, and the sparse distribution of the regional and local seismic stations of many regional seismic networks present additional problems towards computing accurate focal mechanisms of earthquakes below M_w 4.0 (*Tan and Helmberger, 2007; Wéber, 2006*). An imprecise velocity model and uncertainties in earthquake focal depth due to the trade-off between the origin time and focal depth of an earthquake when the hypocenter is computed from a sparse regional seismic network introduce uncertainties in the calculation of the Green's functions. The

sparse seismic network data lack the dense distance and azimuthal coverage required to compute well-constrained focal mechanisms of the events recorded by these network stations using P-wave first motion data.

This chapter presents a new method to determine the focal mechanisms of earthquakes using regional broadband seismic data that come from a sparse regional seismic network. By calculating sets of envelopes of synthetic seismograms for all possible focal mechanisms for a known value of focal depth and a known value of scalar moment and comparing those synthetic seismogram envelopes with the envelopes of observed seismograms, a best match is sought, from which an estimate of the event focal mechanism is made from the moment-tensor that was used to compute for the best matching synthetics. It is demonstrated that the method of this dissertation obtains reliable focal mechanisms for all events with M_w 3.04 and above and some events down to M_w 2.60 using the data recorded at least in 3 seismic stations with epicentral distances of 60-350 km when compared to the focal mechanisms found previously for the same events using other methods. This chapter describes the method of this dissertation in detail and then shows its effectiveness by applying it to some aftershocks of the M_w 5.7 2011 Mineral Virginia earthquake and to some aftershocks of the M_w 4.5 2013 Ladysmith, Quebec earthquake.

5.2 WAVEFORM FITTING METHODOLOGY

The method of this dissertation as applied to calculate the focal mechanisms of the 23 events listed in Table 5.1 is given in Figure 5.1. Both the observed seismograms as well as

the Green's functions were filtered forward and backward through a Butterworth bandpass filter with 2 poles and a passband of 1.5-2.5 Hz. A minimum of 3 stations and a maximum of 6 stations per event each with SNR above 10 were used during the analyses. The epicentral distances of the stations used in the analyses ranged from 61-350 km. Some sample fits of the synthetic envelopes to the observed envelopes are shown in Figure 5.2.

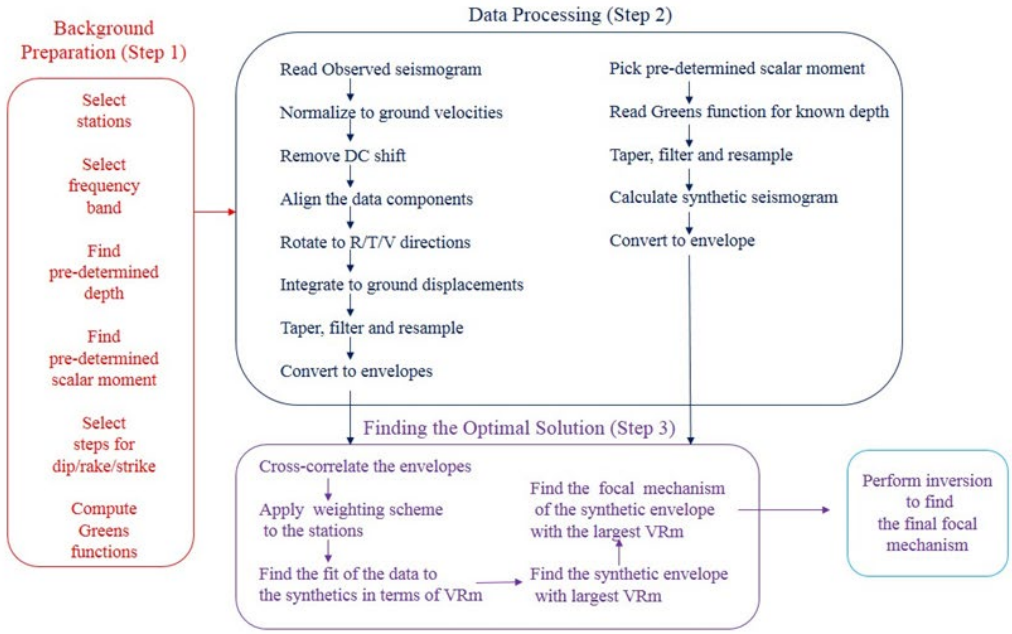

Figure 5.1. Flow chart showing the steps taken to determine the focal mechanism using the method described in this paper. R/T/V refers to Radial/Tangential/Vertical and VRm refers to the modified Variance Reduction of *Dahal and Ebel (2019)*.

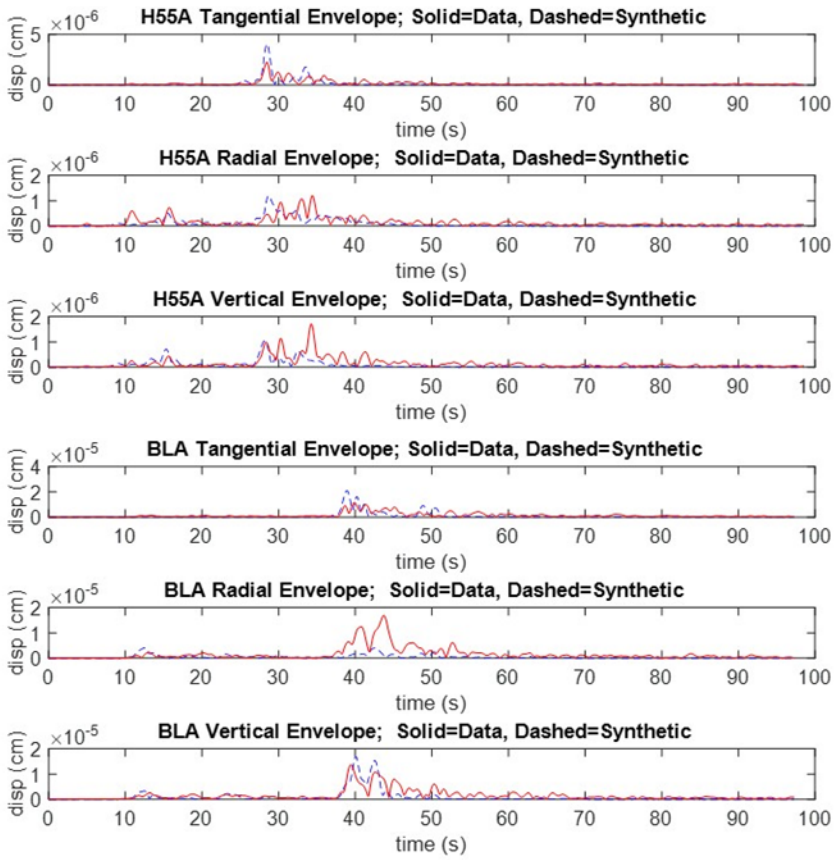

Figure 5.2. Fit of the synthetic envelopes to the data envelopes for a Ladysmith aftershock, Event 23 in Table 5.1 (upper graph, VRm=69.17%) and for a Mineral aftershock, Event 3 in Table 1 (lower graph, VR=61.35%). Synthetic envelopes are generated for the optimal solution of dip= 60º, rake=30º, strike=300º, scalar moment=$1*10^{20}$ dyn-cm and depth=13 km for the Ladysmith aftershock and the optimal solution of dip=60º, rake=60º, strike=180º, scalar moment= $1.1*10^{21}$ dyn-cm and depth=4 km for the Mineral aftershock.

5.3 DATA

Some of the aftershocks of the M_w 5.7 Mineral, Virginia earthquake and some of the M_w 4.5 Ladysmith, Quebec earthquake are analyzed in this chapter for their focal mechanisms. More information about these earthquakes is given in Section 4.2 and Table 4.1 of Chapter 4. The details of these aftershocks as needed in this Chapter are listed in Table 5.1.

Table 5.1: List of Mineral, Virginia aftershocks and Ladysmith, Quebec aftershocks analyzed.

Aftershock Region	Event Number From Table 4.1	Focal Depth (km)	Moment Magnitude (M_w)
Mineral, Virginia	1	4	3.62
	2	4	3.70
	3	4	3.30
	4	3	3.10
	5	4	3.50
	6	4	2.95
	7	4	3.27
	8	4	3.04
	9	4	3.10
	10	5	2.83
	11	4	3.04
	12	4	2.63
	13	4	2.95
	14	3	2.63
	15	7	2.95
	16	3	2.63
	17	3	2.60
	18	4	2.83
Ladysmith, Quebec	19	10	3.62
	20	10	3.04
	21	12	2.83
	22	10	2.83
	23	13	2.63

The 2011 Mineral mainshock along with its 18 aftershocks, the 2013 Ladysmith earthquake along with its 5 aftershocks, and the stations used to obtain the data for the focal mechanisms calculation for each of these events are shown in Figure 4.1.

5.4 RESULTS

By using envelopes to simplify the waveforms, the method of this dissertation provides with an inherent limitation to determine the source mechanism. Going from a seismogram to its envelope, the phase information of the waveform is lost, because a waveform and its 180° flip around the time axis will have the same envelope. In terms of the seismogram, changing the direction of slip by 180° flips the seismogram by 180° around the time axis. This creates ambiguity in the direction of slip on the fault. The method of this dissertation typically yields two possible focal mechanisms for an event, with each focal mechanism different in rake by 180°. Hence, one is not able to distinguish between a thrust and a normal fault using the envelopes of seismograms to constrain the focal mechanism, meaning that the method as applied here inherently has an ambiguity about the true focal mechanism of an event. This ambiguity in the method of this dissertation is similar to what others have reported working with amplitude inversions of seismic waves where they observed a 2-fold indeterminacy in rake along with a 2-fold indeterminacy in strike (e.g., Mendiguren, 1977; Romanowicz et. al. 1983; Okal et al., 2003) and the inversion of the waveform envelopes where they observed a 2-fold indeterminacy in rake (e.g., Zahradník et al., 2018). These studies have also shown that the observed symmetry in rake can be broken by observing the direction of the first P-arrival at one or more stations. Applying

this directional constraint to the two focal mechanisms for a single event obtained from the method of this dissertation can tell which of the two optimal mechanisms is the true one. The directions of the first P-arrivals in the observed seismograms as well as in the synthetic seismograms have been observed and compared for all available stations for the events analyzed in this chapter. Clear P-arrivals from at least 3 stations were available for every event that were analyzed.

Focal mechanisms obtained for the events analyzed using the crustal structures in Table 4.2 and Table 4.3 (a) from the method of this dissertation method are presented in Table 5.2. All of the Mineral aftershocks had thrust-faulting mechanisms except Event 2 in Table 5.1 which had a normal-faulting mechanism and all of the Ladysmith aftershocks had thrust faulting mechanisms as obtained by the method of this dissertation. This is consistent with the faulting mechanisms as obtained by the previous studies (*Wu et al., 2015;* *http://www.eas.slu.edu/eqc/eqc_mt/MECH.NA/*; last accessed March 2018; *Ghafoori, 2017*) for these events. Focal mechanisms of all of the Mineral aftershocks from the previous studies (*Wu et al., 2015*) were obtained using P-wave first motions from the portable station data deployed after the mainshock except for one event (Event number 5 in Table 5.1), for which the focal mechanism was obtained from a regional moment-tensor inversion (*http://www.eas.slu.edu/eqc/eqc_mt/MECH.NA/*, last accessed March 2018). The focal mechanisms from the previous studies of the Ladysmith aftershocks (*Ghafoori, 2017*) were obtained based on P-wave first motions as read from the local and regional stations.

The differences in the focal mechanisms obtained using the method of this dissertation and the previous studies (*Wu et al., 2015;* http://www.eas.slu.edu/eqc/eqc_mt/MECH.NA/, last accessed March 2018; *Ghafoori, 2017*) are calculated in terms of Kagan angles. A Kagan angle between two double couple sources is the angle of rotation with which each source can be rotated to obtain the other and can vary from 0° to 120° where 0° represents the same mechanism and 120° represents totally different mechanisms (*Kagan, 2005*). A Kagan angle well below 60° represents good correspondence between the two mechanisms whereas a Kagan angle above 60° represents a mismatch of the mechanisms (*Pondrelli et al., 2006; D'Amico et al., 2011*). The difference in the dip, rake and strike angles obtained using the coarse grid search and the optimized versions of these angles obtained through the iterative non-linear inversion was about 1° degree for each of the angles for all of the events analyzed. As the Kagan angles reported in Table 5.2 are rounded to their nearest integer, no difference is observed in the Kagan angles calculated using focal mechanisms from the grid search and the inversion with respect to the previously reported solutions. The focal mechanisms of the Mineral Virginia aftershocks as obtained by the method of this dissertation showed Kagan angles of 19° to 87° as compared to the previous solutions (*Wu et al., 2015;* http://www.eas.slu.edu/eqc/eqc_mt/MECH.NA/; last accessed March 2018). The focal mechanisms of the Ladysmith aftershocks as obtained by the method of this dissertation showed Kagan angles of 10° to 66° as compared to the previous solutions (*Ghafoori, 2017*). The Kagan angles for the Mineral and Ladysmith aftershocks are always less than 60° for events with magnitude M_w 3.04 and greater. The average Kagan angle for the Mineral and Ladysmith aftershocks with magnitudes M_w 3.04 and greater is 38°. For

events with magnitudes less than M_w 3.04, the Kagan angles are greater than 60° for 6 of the 11 events.

Table 5.2. Focal mechanisms of the Mineral and Ladysmith aftershocks using the method of this dissertation.

Event Number from Table 5.1	Moment Magnitude (M_w)	Focal Mechanism from this study (D° /R°/S°)	Focal Mechanism from previous studies (D° /R°/S°)	Kagan Angle (°)
1	3.62	60/60/180	49/107/37	19
2	3.70	60/330/300	14/-36/284	47
3	3.30	60/60/180	26/46/172	35
4	3.10	30/60/0	43/59/174	43
5	3.50	30/90/60	73/100/47	48
6	2.95	60/60/270	65/56/65	65
7	3.27	30/120/60	74/96/48	48
8	3.04	30/150/0	17/133/23	41
9	3.10	60/60/180	24/75/198	39
10	2.83	60/60/180	15/58/193	47
11	3.04	60/150/60	19/37/179	46
12	2.63	30/90/30	67/96/37	37
13	2.95	60/60/180	24/76/360	33
14	2.63	60/60/270	62/142/320	69
15	2.95	60/150/30	78/90/41	67
16	2.63	60/120/120	18/84/222	65
17	2.60	30/90/0	69/100/16	40
18	2.83	30/60/0	26/176/34	87
19	3.62	60/120/0	50/57/138	10
20	3.04	60/60/330	-	-
21	2.83	60/60/330	-	-
22	2.83	60/30/330	25/90/140	36
23	2.63	60/30/300	13/51/6	66

For the Mineral Virginia aftershocks previous studies refers to *Wu et al. (2015)* and R. Herrmann's website as given in Data and Resources. For the Ladysmith aftershocks

previous studies refers to *Ghafoori, (2017)*. D°/R°/S° refers to dip/rake/strike angles in degrees. '-' refers to the unavailability of the data. Uncertainties in Kagan angles are not reported in Table 5.2 as the algorithm used to calculate Kagan angles (*Kagan, 2005*) do not provide them. No such uncertainty was found reported in earlier literatures.

The focal mechanisms obtained from the method of this dissertation showed a good correspondence for all events with magnitudes M_w 3.04 and greater but showed a mismatch for 6 out of 11 events with magnitudes less than M_w 3.04. There could be two possible explanations for this observation. The first possibility is that focal mechanism calculation using the method of this dissertation becomes less accurate for events with magnitude less than M_w 3.04. The second possibility is that the focal mechanisms from the previous studies (*Wu et al., 2015; http://www.eas.slu.edu/eqc/eqc_mt/MECH.NA/*, last accessed March 2018; *Ghafoori, 2017*) using the first motion data become less accurate for smaller magnitude events. This has been observed and explained by earlier studies where they found that the focal mechanisms obtained using first motion polarities can become unstable with insufficient azimuthal coverage and are very hard to determine for smaller magnitude events (*D'Amico et al., 2011*). Both of these possibilities could have influenced the Kagan angle results simultaneously.

Tests were done for the minimum number of the stations required to determine an accurate focal mechanism of an event using the method of this dissertation. The variation in the focal mechanisms obtained by using different number of seismic stations for Event 22 in

Table 5.1 is given in Table 5.3. For this event, unique focal mechanisms are obtained even when only one station is included in the analysis except for the station with the azimuth of -148°. For this station, three distinct focal mechanisms (all 3 focal mechanisms have the same VRm) are obtained. These 3 focal mechanisms have Kagan angles of 90°, 42° and 76° with respect to each other. The unique focal mechanism of 60°/30°/330° has Kagan angles of 52°, 30°, 75° with the other unique focal mechanisms obtained using different stations for this event. Thus, it is seen that the focal mechanisms obtained using single stations can be very different from one another. Also the multiple focal mechanisms obtained using single station are also found to be different from each other. A similar multiplicity of possible focal mechanism solutions is obtained when only two stations are included in the analysis, but the focal mechanism becomes unique and stable when three or more stations are used in the analysis. Thus, it is concluded that at least 3 seismic stations are required for the method of this dissertation to provide a reliable focal mechanism for an event. The largest azimuthal gap between the 3 required stations among all events that were analyzed is about 260°. It is concluded that the method is able to recover the focal mechanisms of earthquakes with M_w 3.70-2.63 if there are records of an event from at least 3 regional seismic stations each with SNR 10 or greater. This gives the method great applicability in regions even where the regional and local seismic stations are thinly scattered, which is the case in many places around the world.

Table 5.3. Focal mechanism as a function of the stations used in the grid search for Event 22 in Table 5.1.

Number of stations	Azimuths of the stations used (°)	Focal Mechanisms (D° /R°/S°)	Number of stations	Azimuths of the stations used	Focal Mechanisms (D° /R°/S°)
1	-41	60/30/330	1	-41	60/30/330
1	-56	30/90/180	2	-41,-56	60/90/180
1	-148	60/60/330	3	-41,-56,-148	60/60/330
1	-154	60/0/120, 90/30/300, 90/150/120	4	-41,-56,-148,-154	60/60/330
1	-9	30/120/270	5	-41,-56,-148,-154,-9	60/60/330

Tests were performed for the minimum SNR for the observed seismograms that can be used to find an accurate focal mechanism of an event using the method of this dissertation. In Figure 5.3, it is assumed that a minimum SNR of 10 of an earthquake signal is required to constrain the focal mechanism using the method of this dissertation. Figure 5.3 indicates that one can get reliable focal mechanisms using stations with epicentral distances as great as 350 km for an event of magnitude M_w 3.0 and as great as 310 km for an event of magnitude M_w 2.63 using the method of this dissertation.

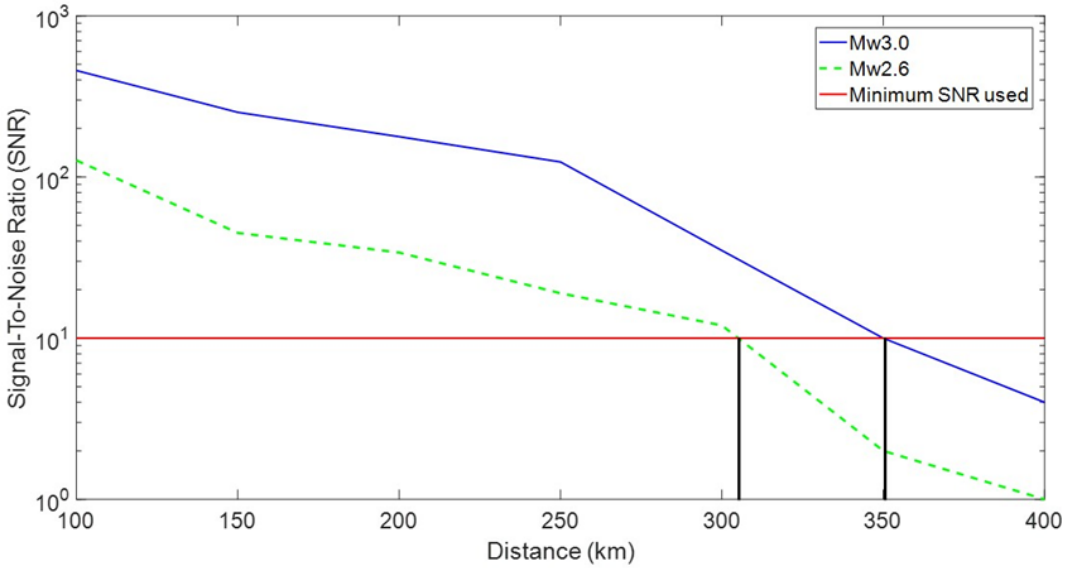

Figure 5.3. Observed decrease of SNR with epicentral distance for the Ladysmith aftershock M_w 3.62 (Event 19 in Table 5.1). The threshold SNR is 10. The threshold epicentral distance for an event of magnitude M_w 3.62 is 350 km whereas the threshold epicentral distance for an event of M_w 2.6 is 310 km.

5.5 SENSITIVITY TO CRUSTAL STRUCTURE

The synthetic envelopes used to determine the focal mechanisms are generated with Green's functions which are functions of the crustal structures used in their computations. For this reason, the velocity structure used to generate Green's functions must affect the focal mechanisms obtained with the method of this dissertation. To investigate how much of an effect variations in the crustal structure might have on the results, three different crustal structures each considered applicable for the region and each with a crustal thickness of 40 km were taken, and Green's functions were generated for the Ladysmith aftershocks using each of those structures. The first crustal structure that was tested is published in the website of R. Herrmann (*http://www.eas.slu.edu/eqc/eqc_mt/MECH.NA/*, last accessed March 2018) and also is listed in Table 4.3 (a). The second crustal structure that was tested is published in Table 8 of *Brune and Dorman (1963)*. This crustal structure as published has a crustal thickness of 35 km, but a modified version of this crustal structure with a crustal thickness of 40 km as published in the Table 5 of *Dahal and Ebel (2019)* was used. The third crustal structure that was tested is published in the last column of Table 1 of *Motazedian et al. (2013)*. The modified version of this model in which the lower velocity layers below 25 km are replaced by higher velocity layers as published in Table 6 of *Dahal and Ebel (2019)* was used.

The results obtained from the tests done on the three different crustal structures as mentioned in the paragraph above are summarized in Table 5.4. The differences in the focal mechanisms obtained among all three crustal structures vary from 0° to 64° in terms of

Kagan angle where 0° was found for the M_w 3.62 event (the largest tested event) and 64° was found for the M_w 2.63 event (the smallest tested event). The average Kagan angle difference between the focal mechanisms obtained using the three crustal structures for Event 19 is 0°, for Event 20 is 44°, for Event 21 is 35°, for Event 22 is 27° and for Event 23 is 43°. The average Kagan angle between the focal mechanisms obtained for the 5 Ladysmith events using Herrmann's crustal structure and Mota's crustal structure is 39°, using Mota's and Brune and Dorman's crustal structures is 29° and using Brune and Dorman's and Herrmann's crustal structures is 21°. The average difference in Kagan angle for the 5 events among all 3 crustal structures is 30°. This sensitivity analysis shows that the focal mechanisms determined by the method of this dissertation show some sensitivity to the crustal details used to generate the Green's functions. The magnitude of the sensitivity varies with the particular event and the crustal structure used in the analysis. The average Kagan angle of 30° observed for the 5 events among all 3 crustal structures is well below 60°, which means that on average the focal mechanisms computed with different crustal structures available for a region using the method of this dissertation well represent each other for events with M_w 3.62 to M_w 2.63.

Table 5.4. Comparison of focal mechanisms obtained for Ladysmith aftershocks using 3 different crustal models.

Event Number From Table 5.1	D°/R°/S° from different crustal models			Kagan Angle Differences (°) between		
	Crustal Model 1 (CM1)	Crustal Model 2 (CM2)	Crustal Model 3 (CM3)	CM1 and CM2	CM2 and CM3	CM3 and CM1
19	60/120/0	60/120/0	60/120/0	0	0	0
20	60/60/330	30/30/150	30/90/180	45	24	64
21	60/60/330	30/90/180	60/30/330	52	52	0
22	60/30/330	60/120/180	60/60/330	24	27	30
23	60/30/300	30/90/180	30/120/180	52	30	47

Crustal Model 1 refers to the crustal structure in Table 4.3 (a). Crustal Model 2 refers to the crustal structure published in Table 6 of *Dahal and Ebel (2019)*, which is the modified form of the crustal structure originally published in *Motazedian et al. (2013)*. Crustal Model 3 refers to the crustal structure published in *Brune and Dorman (1963)*. D°/R°/S° refers to the value of dip/rake/strike angles in degree. Uncertainties in Kagan angles are not reported in Table 5.4 as the algorithm used to calculate Kagan angles (*Kagan, 2005*) does not provide them. No such uncertainty was found reported in the published literatures.

5.6 DISCUSSIONS AND CONCLUSIONS

The focal mechanisms obtained for events with M_w 3.04 and above showed a good correspondence with an average Kagan angle deviation of 38° compared to the mechanisms obtained for these events form earlier studies (*Wu et al., 2015*; http://www.eas.slu.edu/eqc/eqc_mt/MECH.NA/, last accessed March 2018; *Ghafoori, 2017*). Almost half of the events tested below M_w 3.04 showed a mismatch with the previously reported focal mechanisms for these events with Kagan angles ranging from 65°

to 87°. This observation indicates that the focal mechanism determinations using the method of this dissertation becomes less reliable for events below M_w 3.04. The sensitivity test for crustal structure showed that the average Kagan angle between the focal mechanisms obtained using three different crustal structures is 30°, which means that the focal mechanisms obtained from the method of this dissertation are only somewhat sensitive to uncertainties in the crustal model.

In this chapter a new method for determining the focal mechanisms of small earthquakes from magnitude M_w 3.70 down to M_w 2.60 using data from a few local and regional seismic stations at epicentral distances of 60 – 350 km by fitting synthetic waveform envelopes to the envelopes of the observed seismograms is developed and tested. All the Ladysmith aftershocks tested are found to have thrust fault mechanisms. All the Mineral aftershocks tested are found to have thrust fault mechanisms except for Event 2 in Table 5.1 which had normal fault mechanism. These focal mechanisms are consistent with the focal mechanisms reported previously for these events. The focal mechanisms of the Mineral aftershocks had Kagan angles of 19° to 87° compared to the previous solutions (*Wu et al., 2015;* http://www.eas.slu.edu/eqc/eqc_mt/MECH.NA/, last accessed March 2018) whereas the focal mechanisms of the Ladysmith aftershocks had Kagan angles of 10° to 66° compared to the previous solutions (*Ghafoori, 2017*).

When the method of this dissertation is compared with previously published methods to find focal mechanisms using waveform analysis, the method of this dissertation works for the much larger epicentral distance range than that of *Guilhem et al. (2014)*. If one has data

from a sparse regional seismic network with distances from 60-350 km, the method of this dissertation is useful. In contrast, for the data recorded at stations immediately around and over a seismic source, the method of *Guilhem et al. (2014)* is useful. For the regional waveform data within 200 km, the method of *Tan and Helmberger (2007)* can be used for events with $M_w < 3.5$ down to M_w 2.0, provided that there is a nearby M_w 4.0 or greater event. On the other hand, the method of this dissertation can be used for all events with M_w 3.70-2.60 which have the regional data recorded at stations with epicentral distance from 60-350 km without the restriction of having a larger nearby event. The Cut-And-Paste method is useful for events with M_w 4.6 to M_w 2.8 recorded by at least in 4 stations with epicentral distances out to 200 km. The method of this dissertation is useful for events recorded at least in 3 stations with epicentral distances of 50-350 km. Thus, the method of this dissertation is applicable over a greater epicentral distance range for smaller earthquakes than the previously published methods to find focal mechanisms using waveform inversion.

Chapter 6

DETERMINATION OF FOCAL MECHANISMS, FOCAL DEPTHS AND MOMENT MAGNITUDES OF SOME SELECTED AFTERSHOCKS OF THE 2015 GORKHA, NEPAL EARTHQUAKE

6.1 INTRODUCTION

In this chapter, the method developed in this dissertation is applied to some aftershocks of the 2015 Gorkha, Nepal earthquake to obtain the focal depths, focal mechanisms and the moment magnitudes of those aftershocks. The focal depths found in this study improve knowledge of the spatial distribution of the source parameters of the Gorkha aftershocks by providing more constraint on the fault zone structure of the 2015 Gorkha earthquake. Understanding the structures of the faults on which the large earthquakes and the following aftershocks occur can contribute toward an improved understanding of the present day faulting of the Himalayan region. Having knowledge of the structural deformation associated with these earthquakes is crucial to understand the seismic hazard and the potential for future earthquakes in this area. The source properties and the rupture processes of some of the past larger earthquakes provide a broad understanding of the seismotectonics in this region. The source properties of the moderate and smaller magnitude earthquakes still remain poorly known, which prevents understanding of the details of the fault structures (*Bai et al., 2016; Zhang et al., 2016*). The study carried out in this chapter is intended to show how an application of the methods developed earlier in this dissertation can help improve the understanding of the distribution of stress release in the Himalaya in the 2015 earthquake and therefore help provide information about the nearby areas that

may be prone to future earthquakes. Improving the knowledge of the seismotectonics of this part of South Asia would be a great help in encouraging activities to minimize the risk posed by future strong earthquakes to the people who dwell on and near these faults.

6.2 STUDY AREA

The Himalaya has a long history of subduction of the Indian plate under the Eurasian plate along Main Himalayan Thrust (MHT), which is formed by four major faults: the Main Frontal Thrust (MFT), the Main Boundary Thrust (MBT), the Main Central Thrust (MCT) and the South Tibet Detachment (STD) (*Ni and Barazangi, 1984; Zhao et al., 1993; Náb˘elek et al., 2009; Bai et al., 2016*). These four major faults divide the region into four tectonic sub-regions: Sub-Himalaya, Lesser Himalaya, Higher Himalaya and Tethyan Himalaya from south to north (*Yin, 2006; Bai et al., 2016*) as shown in Figure 6.1.

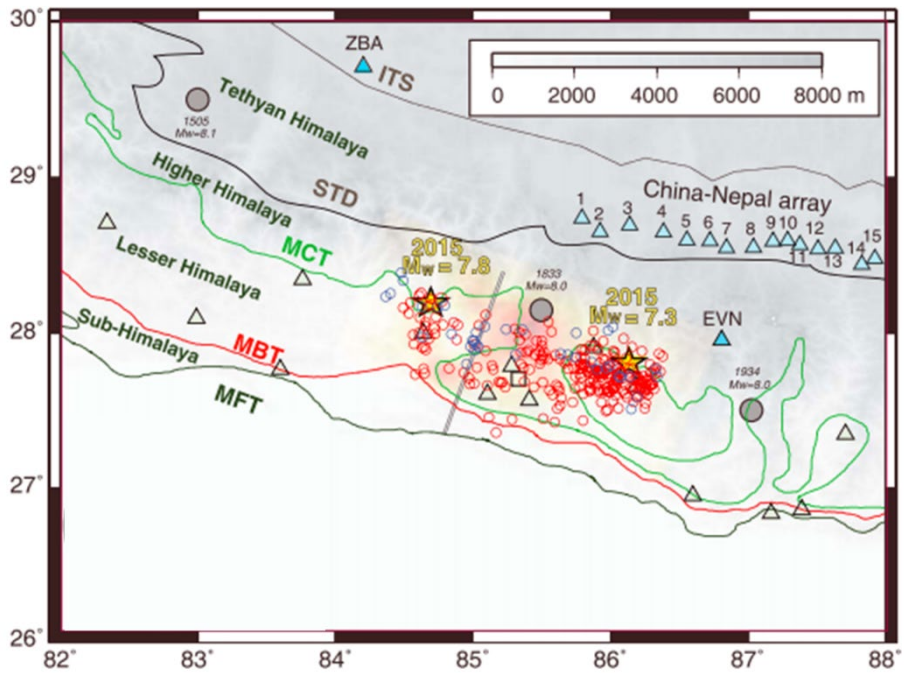

Figure 6.1 The study region showing the locations of Gorkha mainshock and its largest aftershock (yellow stars), aftershocks of these earthquakes (red circles) and earthquakes that occurred before Gorkha earthquake since 1980 (blue circles). Triangles represent the location of the seismic stations. [Figure: *Bai et al., 2016*]

Nepal has been the site of several large earthquakes in its history, some of which are shown in Figure 6.2. The earliest known earthquake, which is considered to be the largest to now, was a magnitude 8.2 event in 1505 that occurred in the western part of Nepal. There were also earthquakes of magnitude 7.7 in 1833 and magnitude 8.1 in 1934 both in the eastern part of Nepal. In 2015, Nepal had an M_w 7.8 earthquake in the western part the country. In Figure 6.2, the dashed lines are the estimated fault ruptures for the previous earthquakes, and the solid rectangle is the fault rupture for the 2015 Gorkha earthquake.

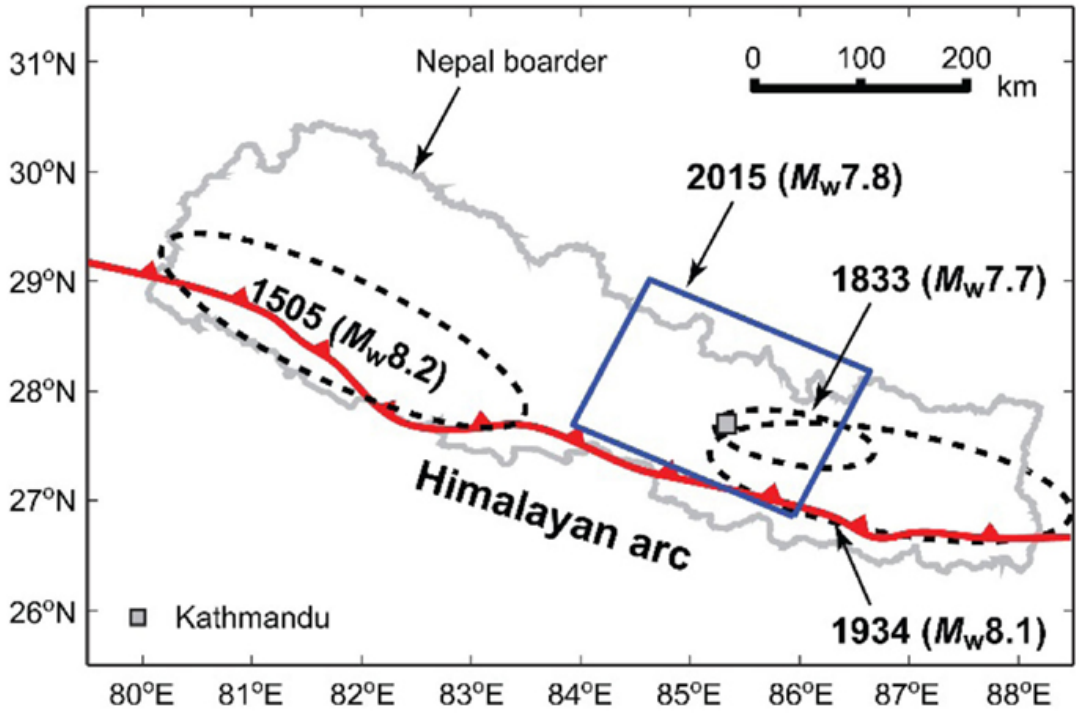

Figure 6.2 Major historical earthquakes in Nepal along the Himalayan arc. The locations of three historical earthquakes (1505, 1833 and 1934) are approximate. For the M_w 7.8 mainshock, the fault plane solution by the USGS is shown. [Figure: *Goda et al., 2015*]

6.3 DATA

The aftershocks of the 2015 Gorkha earthquake are the first well recorded aftershock sequence that occurred on the shallow portion of the Main Frontal Thrust (MHT) (*Bai et al., 2015*). The rapid deployment of portable stations from the Namaste Network after the mainshock allowed seismologists to obtain well-recorded seismograph records for large number of aftershocks. For each event and each station included in the analyses of this chapter, the event magnitude, event origin time and the event location were obtained from the IRIS wilber3 system (*http://ds.iris.edu/wilber3/find_stations/10002986*, last accessed February 2019). The station locations, station network codes and station names are obtained from the IRIS MetaData Agreegator page (*https://ds.iris.edu/mda/XQ/?starttime=2015-01-01T00:00:00&endtime=2016-12-31T23:59:59*, last accessed May 2019). The epicentral distance and the azimuth of each station relative to an event are calculated using the distance-azimuth web service available at IRIS (*http://services.iris.edu/irisws/distaz/1/*, last accessed May 2019). The details of the Gorkha aftershocks analyzed in this chapter are given in Table 6.1. Data from 3 stations with epicentral distances ranging from 63-171 km are used in analyzing each of the events in Table 6.1. The largest azimuthal gap between the 3 stations used in the analysis is about 345°.

Table 6.1: List of Gorkha aftershocks analyzed

Event Number	Date (yyyy/mm/dd)	Time UTC (hh:mm:ss)	Magnitude (mb)	Latitude (°)	Longitude (°)
1	2015/08/11	04:57:44	3.7	27.7475	85.2864
2	2015/10/06	12:02:40	4.0	27.7479	86.1479
3	2015/06/22	07:34:31	4.3	27.6479	86.2800

6.4 METHODOLOGY

The method of this dissertation as applied to the three events listed in Table 6.1 to calculate the focal depths and moment magnitudes is described in Section 4.3 of Chapter 4 and to calculate focal mechanisms is described in Section 5.2 of Chapter 5. The crustal model used to generate Green's function is taken from Table 1 of *Pandey and Tandukar (1995)* and is listed in Table 6.2. Data from stations with epicentral distances 63-171 km were used in the analyses. Some sample fits of the synthetic envelopes to the observed envelopes are shown in Figure 6.3.

Table 6.2: Crustal model used to generate the Green's functions for the Gorkha aftershocks.

Thickness (km)	Vp (km/s)	Vs (km/s)	Rho (g/cc)	1/Qp	1/Qs
23	5.6	3.2	2.3	500	250
32	6.5	3.7	2.7	4000	2000
-	8.1	4.6	3.4	2000	1000

Errors in the parameters in Table 6.2 are not reported as they were not available in the source from where the crustal model is taken.

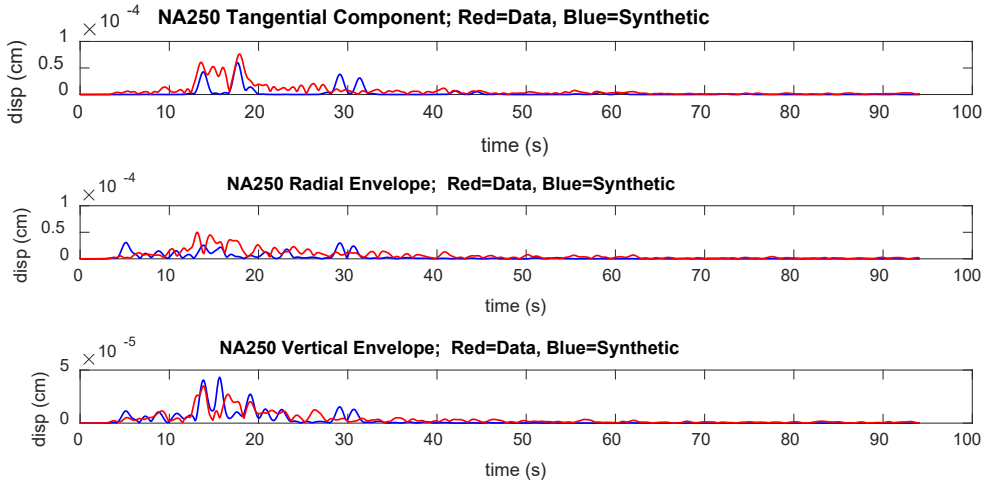

Figure 6.3. Fit of the synthetic envelopes to the data envelopes for a Gorkha aftershock, Event 1 in Table 6.1. Synthetic envelopes are generated for the optimal solution of dip= 30°, rake=150°, strike=120°, scalar moment=30*10^{20} dyn-cm and depth=4 km with VRm = 59.84%.

6.5 RESULTS

Focal depths, moment magnitudes and focal mechanisms obtained for the events analyzed in this chapter are listed in Table 6.2.

Table 6.3. Depths, moment magnitudes and focal mechanisms of the Gorkha aftershocks using the method developed in this dissertation applied to data from all available stations.

Event number from Table 6.1	Scalar Moment from this study (10^{13} N-m)	Magnitude from this study (M_w)	Magnitude from previous study (m_b)	Depth from this study (km)	Depth from previous study (km)	Dip (°)/ Rake (°)/ Strike (°) from this study
1	30	3.62±0.06	4.3	4±0.5	35	30/150/120
2	90	3.94±0.09	4.0	5±4.5	10	60/120/300
3	20	3.50±0.13	4.3	9±1.7	10	30/30/150

Previous study refers to the information published in the USGS's event information page (*https://earthquake.usgs.gov/earthquakes/eventpage*, last visited August 2019). The error in depths and moment magnitudes in Table 6.3 are estimated from the single station analysis presented in Table 6.4. The error in depths and magnitudes from previous studies are not indicated as they were not reported in those studies.

Focal depths, moment magnitudes and focal mechanisms obtained from this study for each of the event listed in Table 6.1 were obtained by analyzing data from 3 stations. The focal depths of the events analyzed ranged from 4-9 km as obtained by the method of this dissertation. The focal depths of these events as obtained by USGS (*https://earthquake.usgs.gov/earthquakes/eventpage*, last visited August 2019) ranged from 10-35 km. The distribution of the depths within 4-9 km as obtained in Table 6.3 is

supported by *Bai et al. (2019)*, who relocated 266 aftershocks of Gorkha earthquake where the depths of these aftershocks ranged from 0.2-23 km with most of the aftershocks concentrated between 4 and 14 km. The fact that the events listed in Table 6.1 are not included in the list of the events analyzed by *Bai et al. (2019)* prevented a direct comparison of the focal depths obtained by the method of this dissertation and those obtained by *Bai et al. (2019)*. The two aftershock sets did not overlap probably because all of the events analyzed by *Bai et al. (2019)* were greater than M_w 4.0 and all of the events analyzed in this study are less than M_w 4.0.

The moment magnitudes of the Gorkha aftershocks as analyzed by the method of this dissertation ranged from M_w 3.62-3.94. Moment magnitudes of the events analyzed in this chapter are reported for the first time. The body-wave magnitudes of these events as reported by the USGS ranged from m_b 3.7 to 4.3. The focal mechanisms obtained for the aftershocks analyzed are listed in Table 6.2. All three focal mechanisms obtained show oblique thrust faulting which is commonly observed for focal mechanisms for this area where the seismotectonics is dominated by a subduction interface. The oblique thrust mechanisms obtained for all three events analyzed using the method of this dissertation is also supported by *Bai et al (2019)* who obtained oblique thrust mechanisms for the most of the aftershocks they analyzed. The focal mechanisms obtained for Events 1, 2 and 3 in Table 6.1 have Kagan angles of 72°, 54°, and 75° respectively with the focal mechanism of the Gorkha mainshock with dip = 7°, rake = 101°, strike = 290° (*https://earthquake.usgs.gov/earthquakes/eventpage/us20002926/moment-tensor*, last

visited August 2019). The focal mechanisms of the Gorkha aftershocks as obtained by *Bai et al., (2019)* have Kagan angles ranging from 10º to 75º with the focal mechanism of the mainshock. The Kagan angles for the three events analyzed in this chapter fall within the range of the Kagan angles obtained for the 17 aftershocks analyzed by Bai *et al. (2019)*. This indicates that the method of this dissertation is able to obtain focal mechanisms for the Gorkha aftershocks that are comparable in quality to those obtained by Bai *et al. (2019)*. The accuracy of all of these aftershock focal mechanisms, both those from this study and those of Bai *et al. (2019),* require further investigation.

Table 6.4. Depths and moment magnitudes of the Gorkha aftershocks found using the method of this dissertation applied to data from a single station.

Event number from Table 6.1	Station used	Depth from single station analysis (km)	Mean depth of single station analysis ± standard deviation (km)	Depth using all stations from Table 6.1 (km)	Scalar Moment (10^{13} N-m)	M_w	Mean M_w of single station analysis ± standard deviation	M_w using all stations from Table 6.1
1	NA200	5	4.7±0.5	4	20	3.50	3.58±0.06	3.62
	NA210	4			30	3.62		
	NA250	5			30	3.62		
2	NA010	7	10.7±4.5	5	100	3.97	3.90±0.09	3.94
	NA050	8			50	3.77		
	NA090	17			100	3.97		
3	NA020	10	10.7±1.7	9	30	3.62	3.65±0.13	3.50
	NA040	13			60	3.82		
	NA150	9			20	3.50		

The error involved in the calculation of the focal depths and moment magnitudes of the Gorkha aftershocks analyzed are estimated by obtaining the focal depths and moment magnitudes using data from a single station. The focal depths and moment magnitudes obtained by analyzing data from individual stations for all three events listed in Table 6.1 are presented in Table 6.4. Three individual stations for each of these events were used in the single station analysis as shown in Table 6.4. The depths in Table 6.3 obtained using three stations are within two standard deviations of the mean depths presented in Table 6.4 obtained using each of the three stations. The moment magnitudes in Table 6.3 obtained using three stations are within one standard deviation of the mean moment magnitudes in Table 6.4 obtained by using each of the three stations. Standard deviations of 0.5-4.5 km are found for the focal depths whereas the standard deviations of 0.06-0.13 magnitude units are observed in the M_w values. This shows that the uncertainties involved in the calculation of moment magnitudes are less than the uncertainties involved in the calculation of the scalar moment and hence the moment magnitudes.

6.6 CONCLUSIONS

The new method developed in this dissertation is successfully applied to some aftershocks of the M_w 7.8 2015 Gorkha, Nepal earthquake using data from portable stations with epicentral distances of 63-171 km. The focal depths of the aftershocks analyzed ranged from 4-9 km with standard deviations ranging from 0.5-4.5 km. These focal depths are all shallower than the mainshock focal depth of 23.5 km (*https://earthquake.usgs.gov/earthquakes/eventpage/us20002926/moment-tensor*, last

visited August 2019) which shows that these aftershocks lie in the hanging wall of the maishock rupture above the MHT, which is also observed by *Bai et al, (2019)* for 95% of the aftershocks analyzed by them. The moment magnitudes obtained for the events ranged from M_w 3.50-3.94 with standard deviations ranging from 0.06-0.13 magnitude units. The focal mechanisms obtained for the three Gorkha aftershocks analyzed in this chapter support the thrust faulting mechanisms developed in the Himalayas due to the northward motion of the Indian plate beneath the Eurasian plate. The analysis of this chapter indicates that the method developed earlier in this dissertation using aftershock data from the intraplate region of the northeast North America is also applicable to the aftershocks from the subduction region of South Asia. This suggests that the method developed in this dissertation should be applicable to the earthquakes from different tectonic regimes around the globe.

Chapter 7

SUMMARY AND FUTURE RESEARCH

7.1 OVERVIEW OF DISSERTATION RESULTS

As described in Chapter 1, the motivation behind the research carried out in this dissertation was to develop a new method to accurately constrain the focal depths, moment magnitudes and focal mechanisms of earthquakes with magnitude less than M_w 4.0 recorded by a sparse regional seismic network. To achieve this goal, a new methodology for calculating focal depths, moment magnitudes and focal mechanisms is proposed in Chapter 3. This methodology is tested with earthquakes from two different geographical settings and the results are presented and analyzed in Chapters 4 and 5. After confirming in Chapters 4 and 5 that the method is successfully developed, the method is applied to the aftershocks from the 2015 M_w 7.8 Nepal earthquake in Chapter 6. The conclusions from this dissertation are summarized in the following sections.

7.1.1 DETERMINATION OF FOCAL DEPTHS

It is challenging to determine the focal depths of earthquakes with magnitude below M_w 4.0 recorded by a sparse regional network of seismic stations. As such earthquakes are usually recorded by relatively few seismic stations, determining the focal depths of these small magnitude earthquakes is not an easy task. The methodology developed in this dissertation is able to constrain the focal depths of earthquakes down to magnitude M_w 2.5 by using data from as few as one seismic station. The results show that the method does

not depend very much on the crustal model other than the total thickness of the crust in the model. Focal depths as determined by the new method developed in this dissertation tend to be shallower with a thicker crust and vice-versa. The focal depth of an earthquake can be obtained using the new method of this dissertation if there are broadband waveforms with SNR 5 or greater from at least one station regional seismic network. This condition is satisfied by a station as far as 510 km from an event of M_w 3.6 and a station as far as 150 km from an event of M_w 2.1.

7.1.2 DETERMINATION OF MOMENT MAGNITUDES

Moment magnitude best represents the size of an earthquake among all the available magnitude scales and, it is the preferred earthquake magnitude in most scientific studies. The method developed in this dissertation can be used to calculate the scalar seismic moment, and therefore moment magnitudes, of earthquakes as small as M_w 2.5. The method is shown to constrain the moment magnitudes of earthquakes with M_w 3.7-2.6 even using a single regional seismic station with SNR 5 of greater, as is the case for the focal depth of the earthquake. The determination of moment magnitudes as done using the method developed in this dissertation is independent of the crustal thickness as well as the crustal velocity structure details used to generate Green's functions.

7.1.3 DETERMINATION OF FOCAL MECHANISMS

The method developed in this dissertation is able to determine the focal mechanisms of earthquakes from M_w 3.70 down to M_w 2.60 by using data from just a few local and regional

seismic stations at epicentral distances of 60-350 km. Using data from at least 3 local or regional seismic stations and using at least one P-wave first motion polarity constraint, the method is able to find the focal mechanisms of small magnitude earthquakes. The average Kagan angle difference between the focal mechanisms of an event obtained using three different crustal structures available for the region is found to be 30° which suggests that focal mechanisms obtained using three different crustal structures well represent each other. The focal mechanism of an M_w 3.7-2.6 earthquake can be obtained using the new method if we have data with SNR 10 or greater from at least three seismic stations. This condition is satisfied by a station as far as 350 km from an event of M_w 3.6 and a station as far as 310 km from an event of M_w 3.0.

7.2 DIRECTIONS FOR FUTURE RESEARCH

7.2.1 EXTENDING THE METHOD TO LOWER MAGNITUDE EARTHQUAKES

The method as developed in this dissertation is able to constrain the focal depths, moment magnitudes and the focal mechanisms of earthquakes with magnitudes between M_w 3.6-2.6. In Chapter 4, it is estimated that the method should be able to constrain the focal depths and moment magnitudes of earthquakes as small as M_w 2.1. It would be a good study to find a data set where the earthquakes with magnitude smaller than M_w 2.6 are well recorded by regional and local seismic stations and test the method for the focal depths, moment magnitudes and focal mechanisms of those earthquakes. Rigorous testing may be required to find the optimal frequency band for filtering the data used during the analysis to extend

the method to lower magnitudes. Instead of including the full waveforms in the analysis, tests can be performed with the sections of the waveforms, similar to the cut-and-paste method of *D'Amico et al. (2011)*. Some sections of the event waveforms may be more sensitive to the source parameters than the other sections, and isolating these sections for analysis may improve the ability of the method to obtain robust results. This can be determined by carrying out tests on multiple sections of the waveforms.

7.2.2 CONSTRAINING THE POTENTIAL SEISMIC SOURCE ZONES FOR FUTURE POSSIBLE EARTHQUAKES

The method developed in this dissertation can be used to constrain the possible seismic source zones for the future possible earthquakes in different parts of the world. As an example, the method developed in this dissertation is applied successfully to some aftershocks of the 2015 Gorkha earthquake in Chapter 6. Here are examples of some additional earthquakes from other parts of the world with aftershock sequences that may be the potential candidates for studies similar to that carried out in this dissertation. One set of earthquakes is the aftershocks of the 2010 M_w 7.0, Haiti earthquake and another set of the earthquakes is the aftershocks of the 2017 M_w 7.1, Puebla, Mexico earthquake. Data for hundreds of aftershocks of magnitude M_w 3.5-2.5 from aftershock sequences like these are available at the IRIS DMC. These aftershocks are in the two different tectonic settings. The earthquakes in Mexico are caused by the subduction of an oceanic plate under a continental plate whereas the earthquakes in Haiti are caused by a transform fault that lies

between the North American plate and the Caribbean plate. Constraining the source parameters of the earthquakes in these two different tectonic settings will help to map faults by providing more precise spatial distributions of the earthquakes in these regions. Having knowledge of the structural deformation that took place in the earth when these earthquakes occurred will help to provide a better understanding of the seismic hazard and the potential for future earthquakes in these areas.

7.2.3. EXTENDING THE METHOD TO INCLUDE NEAR DISTANCE DATA

The method as developed in this dissertation is applied to the data from the local and regional seismic network stations which are at epicentral distance greater than 68 km. The method is then applied to the aftershocks of the Gorkha earthquakes using the data from the portable stations where the epicentral distance of the stations are 63-171 km. More analysis is required to extend the method to include near distance data.

Chapter 8

REFERENCES

Arfken, G. (1985). Mathematical Methods for Physicists, 3rd ed., *Academic Press Inc.*, Orlando, Florida, USA, 985 pp.

Bath, M. (1954). The elastic waves Lg and Rg, along Euroastic paths, *Arkiv Geofys.*, **2**, 295-324.

Bai, L., H. Liu, J. Ritsema, J. Mori, T. Zhang, Y. Ishikawa, and G. Li (2016). Faulting structure above the Main Himalayan Thrust as shown by relocated aftershocks of the 2015 Mw 7.8 Gorkha, Nepal, earthquake, *Geophys. Res. Lett.*, **43**, 637–642, doi:10.1002/2015GL066473.

Bai, L., L. Klemperer, J. Mori, M.S. Karplus, L. Ding, H. Liu, G. Li, B. Song and S. Dhakal (2019). Lateral variation of the Main Himalayan Thrust Controls the Rupture Length of the 2015 Gorkha Earthquake in Nepal, *Sci. Adv.*, **5**, 637–642, doi: 10.1126/sciadv.aav0723.

Bent, A.L., M. Lamontagne, V. peci, S.Halchuk, G.R. Brooks, D. Motazedian, J.A. Hunter, J. Adams, C. Woodgold, J. Drysdale, S. Hayek and W.N. Edwards (2015). The 17 May 2013 M 4.6 Ladysmith, Quebec, Earthquake, *Seism. Res. Lett.*, **86,** 460-476, doi: 10.1785/0220140138.

Billings, S. D., B. L. N. Kennett and M. S. Sambridge (1994). Hypocentre location: genetic algorithms incorporating problem-specific information, *Geophys. J. Int.,* **118,** 693–706.

Bisztricsany, E.A. (1958). A new method for the determination of the magnitudes of earthquakes, *Geofiz Kozl*, **7**, 69-76.

Bock, G. (2010). Depth Phases from Local Earthquakes, *BMR J. of Aus. Geology & Geophys*, **13,** 275-275.

Burridge R. and L. Knopoff (1964). Body Force Equivalents for Seismic Dislocations, *Bull. Seism. Soc. Am.,* **54,** 1875-1888.

Bouchon, M. (1982). The complete synthesis of seismic crustal phases at regional distances, *J. Geophys. Res.*, **87**, 735–1,741.

Brune, J. and J. Dorman (1963). Seismic Waves and Earth Structure in the Canadian Shield, *Bull. Seism. Soc. Am.,* **53**, 167-210.

Cronin, V. (2010). A Draft Primer on Focal Mechanism Solutions for Geologists (https://www.ocean.washington.edu/courses/oc410/reading/Focal_mechanism_primer.pdf).

Dahal, N., and J.E. Ebel (2016). Nonlinear Moment Tensor Inversion of the Envelopes and Cumulative Energy of Regional Seismic Waveforms, *Seism. Res. Lett.,* **88,** pp.247, January/February 2017. (Abstract)

.

D'Amico, S., B. Orecchio, D. Presti, A. Gervasi, L. Zhu., I. Guerra, G. Neri, and R.B. Herrmann (2011). Testing the stability of moment tensor solutions for small earthquakes in the Calabo-Peloritan Arc region (southern Italy), *Boll. Geo. Teor. Appl.*, **52**, 283-298, doi: 14.4430/bgta0009.

D'Amico, S. (2014). Source Parameters Related to a Small Earthquake Swarm Off-shore of Malta (Central Mediterranean), *Development in Earth Science*, **2**, 8-13.

Dreger, D. S., and D. V. Helmberger (1990). Broadband modeling of local earthquakes, *Bull. Seism. Soc. Am.*, **80,** 1162– 1179.

Dreger, D. S., and D. V. Helmberger (1993). Determination of Source Parameters at Regional Distances with Single Station or Sparse Network Data, *J. Geophys. Res.*, **98**, 8107-8125.

Duputel, Z., L. Rivera, Y. Fukahata and H. Kanamori (2012). Uncertainty Estimations for seismic source inversions, *Geophys. J. Int.,* **190,** 1243–1256, doi: 10.1111/j.1365-246X.2012.05554.x.

Ebel, J.E. (1982). M_L measurements for northeastern United States earthquakes, *Bull. Seism. Soc. Am.,* **72,** 1367–1378.

Ford, S.R., D. S. Dreger and W. R. Walter (2009). Identifying isotropic events using a regional moment tensor inversion, *J. Geophys. Res.*, **144,** B01306, doi:10.1029/2008JB005743.

Ghafoori, S. (2017). Analyses of Earthquakes in the Western Quebec Seismic Zone from the United States Transportable Array, M. Sc. Thesis, *Carleton University*, Ottawa, Canada.

Gilbert, F. (1973). Derivation of source parameters from low-frequency spectra, *Phil. Trans. R Soc.*, **274**, 369-371.

Goda, K, T. Kiyota, R.M. Pokhrel, G. Chiaro, T. Katagiri, K. Sharma and S. Wilkinson (2015). The 2015 Gorkha Nepal earthquake: insights from earthquake damage survey, *Front. Built Environ.* **1:8**. doi: 10.3389/fbuil.2015.00008.

Gomberg, J.S., K.M. Shedlock and S.W. Roecker (1990). The effect of *S*-wave arrival times on the accuracy of hypocenter estimation, *Bull. Seism. Soc. Am.,* **80,** 1605–1628.

Guilhem, A., L. Hutchings, D.S. Dreger, and L.R. Johnson (2014). Moment tensor inversions of M ~ 3 earthquakes in the Geysers geothermal fields, California, *J. Geophys. Res. Solid Earth*, **119**, 2121-2137, doi: 10.1002/2013JB010271.

Gutenberg, B., and C.F. Richter (1942). Earthquake Magnitude, Intensity, Energy and Acceleration, *Bull. Seism. Soc. Am*., **32**, 163-191.

Gutenberg, B. (January 1945). Amplitudes of Surface Waves and Magnitudes of Shallow Earthquakes, *Bull. Seism. Soc. Am.,* **35,** 3–12.

Gutenberg, B., and C. F. Richter (1956). Magnitude and energy of earthquakes, *Inn. Geofis*., **9**, 1-15.

Hanks, T.C. and H. Kanamori (1979). A Moment Magnitude Scale, *J. Geophys. Res,* **84**, 2348-2350.

Horton, J.W., Jr., M.C. Chapman, and R.A. Green (2015a). The 2011 Mineral, Virginia, Earthquake, and Its Significance for Seismic Hazards in Eastern North America-Overview and Synthesis, in Horton, J.W., Jr., Chapman M.C., and Green R.A.,eds., The 2011 Mineral, Virginia, Earthquake, and Its Significance for Seismic Hazards in Eastern North America, *Geological Society of America Special Paper*, **509**, 1-25, doi:10.1130/2015.2509(01).

Horton, J.W., Jr., A.K. Shah, D.E. McNamara, S.L. Snyder and A.M. Cartner (2015b). Aftershocks illuminate of the 2011 Mineral, Virginia, earthquake causative fault zone and nearby active faults, in Horton, J.W., Jr., Chapman M.C., and Green R.A., eds., The 2011 Mineral, Virginia, Earthquake, and Its Significance for Seismic Hazards in Eastern North America, *Geological Society of America Special Paper*, **509,** 253-271, doi:10.1130/2015.2509(14).

Howell, B.F, Jr. (1981). On the saturation of Earthquake Magnitudes, *Bull. Seism. Soc. Am.,* **71,** 1401-1422.

Ichiyanagi, M., N. Takai, N. Shigefuji, S. Bijukchhen, T. Sasatani, S. Rajaure, M.R. Dhital and H. Takahashi (2016). Aftershock activity of the 2015 Gorkha, Nepal, earthquake determined using the Kathmandu strong motion seismographic array, *Earth Planet and Space*, **68**, 1-6, doi: 10.1186/s40623-016-0402-8.

Jost, M.L., and R.B. Herrmann (1989). A Student's Guide to and Review of Moment Tensors, *Seism. Res. Lett.*, **60**, 37-57.

Kafka, A.L., (1990). Rg As A Depth Discriminator For Earthquakes And Explosions: A Case Study In New England, *Bull. Seism. Soc. Am.,* **8,** 373-394.

Kagan, Y.Y. (2005). Double-couple earthquake focal mechanism: random rotation and display, *Geophys. J. Int.*, **163**, 1065–1072, doi: 10.1111/j.1365-246X.2005.02781.x.

Knopoff, L., F. Schwab, and E. Kausel (1973). Interpretation of Lg, *Geophys. J. R. Astron. Soc.*, **33**, 389–404

Langston, C. A. (1981). Source transmission of seismic waveforms: the Koyna, India earthquakes of September 13, 1967, *Bull. Seism. Soc. Am.,* **71,** 1-24.

Langston, C.A. (1987). Depth of Faulting during the 1986 Meckering, Australia, earthquake sequence determined from waveform analysis of local seismograms. *Geophys. J. Res.* **92,** 11561–11574.

Ma, S. (2010). Focal Depth Determination for Moderate and Small Earthquakes by Modeling Regional Depth Phases sPg, sPmP, and sPn, *Bull. Seism. Soc. Am.,* **100,** 1-16, doi: 10.1785/0120090103.

Ma, S., and D. W. Eaton (2011). Combining double-difference relocation with regional depth-phase modelling to improve hypocentre accuracy, *Geophys. J. Int.* **185,** 871–889, doi: 10.1111/j.1365-246X.2011.04972.x.

Motazedian, D., S. Ma and S. Crane (2013). Crustal Shear-Wave Velocity Models Retrieved from Rayleigh-Wave Dispersion Data in Northeastern North America, *Bull. Seism. Soc. Am., **103,*** 2266-2276.

Mendiguren, J.A. (1977). Inversion of surface Wave Data in Source Mechanism Studies, *J. Geophys. Res.*, **82**, 889-894.

Náb˘ elek, J., G. Hetenyi, J. Vergne, S. Sapkota, B. Kafle, M. Jiang, H. Su, J. Chen, B. Huang, and H.-C. Team (2009). Underplating in the Himalaya-Tibet collision zone revealed by the Hi-CLIMB experiment, *Science*, **325**, 1371–1374.

Necioglu, A., and O. W. Nuttli (1971). Surface wave attenuation in the United States east of the Rocky Mountains, *Eos Trans. AGU*, **52**, 285. (abstract)

Ni, J., and M. Barazangi (1984). Seismotectonics of the Himalayan collision zone: Geometry of the underthrusting Indian plate beneath the Himalaya, *J. Geophy. Res.*, **89**, 1147–1163.

Nuttli, O.W. (1973). Seismic Wave Attenuation and Magnitude Relations for Eastern North America, *J. Geophys. Res.,* **5,** 876–885.

Okal, E.A. and D. Reymond (2003). The mechanism of great Banda Sea earthquake of 1 February 1938: applying the method of preliminary determination of focal mechanism to a historical event, *Earth Planet. Sci. Lett*, **216,** 1-15. doi: 10.1016/S0012-821X(03)00475-8.

Pandey, M.R. and R.P. Tandukar (1995). Interseismic Strain Accumulation on the Himalayan Crustal Ramp (Nepal), *J. Geophys. Res.,* **22**, 751-754.

Pavlis, G.L. (1986). Appraising earthquake hypocenter location errors: a complete, practical approach for single-event locations, *Bull. Seism. Soc. Am., 76,* 1699-1717.

Pondrelli S., S. Salimbeni, G. Ekström, A. Morelli, P. Gasperiniand and G. Vannucci (2006). The Italian CMT dataset from 1977 to the present, *Phys. Earth Planet. Int.*, **159**, 286-303, doi: 10.1016/j.pepi.2006.07.008.

Okal, E.A., Dominique Reymond (2003). The mechanism of great Banda Sea earthquake of 1 February 1938: applying the method of preliminary determination of focal mechanism to a historical event, *Earth Planet. Sci. Lett*, **216,** 1-15. doi: 10.1016/S0012-821X(03)00475-8.

Richter, C.F. (1935). An Instrumental Earthquake Magnitude Scale, *Bull. Seism. Soc. Am.,* **25**, 1-35.

Romanowicz, B., and G. Suarez (1983). On An Improved Method To Obtain The Moment Tensor And Depth Of Earthquakes From The Amplitude Spectrum Of Rayleigh Waves, *Bull. Seism. Soc. Am.,* **73**, 1513-1526.

Saikia, C.K. (1994). Modified frequency-wavenumber algorithm for regional seismograms using Filon's quadrature: modelling of L_g waves in eastern North America, *Geophys. J. Int.,* **118,** 142–158.

Stein S. and M. Wysession (2003). An Introduction to seismology, Earthquakes and Earth Structures, *Blackwell Publishing*, Malden, Massachusetts, USA.

Tan, Y., and D. Helmberger (2007). A New Method for Determining Small Earthquake Source Parameters Using Short-Period P Waves, *Bull. Seism. Soc. Am.*, **97**, 1176-1195, doi: 10.1785/0120060251.

Tan Y., L. Zhu, D. Helmberger and C. Saikia (2006). Locating and modeling regional earthquakes with two stations, *J. Geophys. Res.*, **111**, B01306, 1-15.

Wéber, Z. (2006). Probabilistic local waveform inversion for moment tensor and hypocentral location, *Geophys. J. Int.,* **165**, 607 – 621, doi: 10.1111/j.1365-246X.2006.02934.x.

Wu, Q., M.C. Chapman and J.N. Beale (2015). The Aftershock Sequence of the 2011 Mineral, Virginia, Earthquake Temporal and Spatial Distribution, Focal Mechanisms, Regional Stress, and the Role of Coulomb Stress Transfer, *Bull. Seism. Soc. Am.,* **105,** 2521–2537, doi: 10.1785/0120150032

Yin, A. (2006). Cenozoic tectonic evolution of the Himalayan orogen as constrained by along-strike variation of structural geometry, exhumation history, and foreland sedimentation, *Earth Sci. Rev.*, **76**, 1–131.

Zang, M., D. Tian, and L. Wen (2014). A new method for earthquake depth determination: stacking multiple-station autocorrelograms, *Geophys. J. Int.* **197,** 1107–1116, doi: 10.1093/gji/ggu044.

Zahradník, J., and E. Sokos (2018). Fitting Waveform Envelopes to Derive Focal mechanisms of Moderate Earthquakes, *Seism. Res. Lett.*, **89,** 1137-1145, doi: 10.1785/0220170161.

Zhang, H., S. van der Lee, and Z. Ge (2016). Multiarray rupture imaging of the devastating 2015 Gorkha, Nepal, earthquake sequence, *Geophys. Res. Lett.*, **43**, 584–591, doi:10.1002/2015GL066657.

Zhao, L.S., and D.V. Helmberger (1994). Source estimation from broadband regional seismograms, *Bull. Seism. Soc. Am.*, **84**, 91-104.

Zhao, W., K. D. Nelson, and Project INDEPTH Team (1993). Deep seismic reflection evidence for continental underthrusting beneath southern Tibet, *Nature*, **366**, 557–559.

Zhu, L., and D.V. Helmberger (1996). Advancement in source estimation techniques using broadband regional seismograms, *Bull. Seism. Soc. Am.*, **86**, 1634-1641.

Zahradník, J., and E. Sokos (2018). Fitting Waveform Envelopes to Derive Focal mechanisms of Moderate Earthquakes. *Seism. Res. Lett.*, **89,** 1137-1145, doi: 10.1785/0220170161.

APPENDIX

APPENDIX I

Abbreviations

CEUS: Central and Eastern United States

DDRM: Double Difference Relocation Method

DMC: Data Management Centre

IRIS: Incorporated Research Institutions for Seismology

OT: Origin Time

RDPM: Regional Depth Phase Modelling

SMAC: Stacking Multiple-Station Autocorrelograms

SNR: Signal-to-Noise Ratio

TU: Tribhuvan University

UTC: Coordinated Universal Time

VRm: Modified Variance Reduction

1-D: 1-Dimensional

APPENDIX II

Publications and Manuscripts

1. **Dahal N.R.** and J.E. Ebel (2019). Method for Determination of Focal Mechanisms of Magnitude 2.5 to 4.0 Earthquakes Recorded by a Sparse Regional Seismic Network, submitted to *Bull. Seism. Soc. Am.*, manuscript number: BSSA-D-19-00170.
2. **Dahal N.R.** and J.E. Ebel (2019). Method for Determination of Depths and Moment Magnitudes of Small-Magnitude Local and Regional Earthquakes Recorded by a Sparse Seismic Network, *Bull. Seism. Soc. Am.*, **109**, 124–137, doi: 10.1785/0120180151.
3. Bent, A.L., S. Halchuk, V. Peci, K.E. Butler, K.B.S. Burke, J. Adams, **N. Dahal**, and S. Hayek (2017). The McAdam, New Brunswick, Earthquake Swarm of 2012 and 2015-2016: Extremely Shallow Natural Events, *Seism. Res. Lett.,* **88**, 1586-1600, doi: 10.1785/0220170071.
4. Ebel, J.E., **N.R. Dahal**, O. Fadugba, A.S. Moulis (2017). Establishing an Operational Earthquake Forecasting System at Weston Observatory of Boston College: ftp://eclogite.geo.umass.edu/pub/stategeologist/MEMA_1994_10_UMSISA/MEMAOEFSFinalReport6_19.pdf (Report).

APPENDIX III

VITA

I, Nawa R. Dahal, was born in Banepa Municipality-03 (formerly Ugrachanndi VDC-07), Kavrepalanchowk, Nepal. I graduated with SLC (School Leaving Certificate) from Bal Batika vidya Mandir in Banepa and joined Kantipur Valley Higher Secondary School, Lalitpur, Nepal where I earned my higher secondary degree. I then joined Tri-Chandra Multiple Campus, Kathmandu, Nepal in Physical Sciences after which I received Master's degree in Physics at Central Department of Physics, TU, Kathmandu, Nepal. Then, I taught Physics to higher secondary students in HSEB (Higher Secondary Education Board) affiliated colleges. Lastly, I joined Boston College and completed Ph.D. degree in Geophysics/Physics in September 2019.